Exclusive J/Ψ Vector-Meson Production in High-Energy Nuclear Collisions

A cross-section determination in the Colour Glass Condensate effective field theory and a feasibility study using the STARlight Monte Carlo event generator

Andrecia Ramnath

Supervisor: Associate Professor Heribert Weigert

Co-supervisor: Doctor Andrew Hamilton

A dissertation presented for the degree of Master of Science
in the Department of Physics at the University of Cape Town, South Africa

Submitted for Examination: 17 February 2014

Revised: 16 May 2014

Abstract

The cross-section calculation for exclusive J/Ψ vector-meson production in ultra-peripheral heavy ion collisions is approached in two ways. First, the setup for a theoretical calculation is done in the context of the Colour Glass Condensate effective field theory. Rapidity-averaged n-point correlators are used to describe the strong interaction part of this process. The JIMWLK equation can be used to predict the energy evolution of a correlator. In order to facilitate practical calculations, an approximation scheme must be employed. The Gaussian Truncation is one such method, which approximates correlators in terms of new 2-point functions. This work takes the first step beyond this truncation scheme by considering higher-order n-point functions in the approximation. An expression for the cross-section is written, which takes parametrised 2- and 4-point correlators as input. This expression can be used as the basis for a full cross-section calculation. The second part of the thesis is a feasibility study using Monte Carlo simulations done by the STARlight event generator. A prediction is made for how many exclusive J/Ψ vector-mesons are expected to be detected by ATLAS in a data set corresponding to 160 μb^{-1} total integrated luminosity. It is found that the muon reconstruction efficiencies for low p_T muons is too poor in ATLAS to do this analysis effectively. On the order of 150 candidate events are expected from all the Pb-Pb collision data collected in 2011. The feasibility study acts as a preliminary investigation for a full cross-section measurement using ATLAS collision data. Once this is completed, it can be compared with the theoretical prediction for the cross-section.

Plagiarism Declaration

I know the meaning of plagiarism and declare that all of the work in this dissertation, save for that which is properly acknowledged, is my own. In particular, Chapter 2 is based on [1] and Chapter 3 is based on [2]. This dissertation has not been submitted, either in the same or different form, to this or any other university for a degree.

Signed: Andrecia Ramnath

Contents

Introduction

The goal of particle physics is to describe all known matter at the most fundamental level. That is, at length and energy scales at which the constituents of matter cannot be fragmented into more elementary components. The overarching theory that encapsulates the present state of the field is the Standard Model of particle physics - a theory that attempts to describe all known fundamental particles and their interactions with each other. It is a culmination of experimental discoveries and theoretical advancements; a historical quilt of both realms of physics working hand-in-hand in the pursuit of a complete description of nature.

The scales at which the elementary particles are probed are well beyond those of everyday human experience and require cutting-edge technology and engineering to be explored. The current experimental approach to accessing the required energies is through particle colliders, in which atomic nuclei are accelerated to relativistic speeds and then crashed into each other. The most powerful collider ever built is the Large Hadron Collider (LHC) at CERN in Geneva, Switzerland. It is capable of colliding protons and heavy ions with an unprecedented design centre-of-mass energy of 14 TeV.

Since the collided nuclei are so small and travel close to the speed of light, a theoretical description of the underlying physics requires the use of both quantum mechanics and special relativity. Enter, quantum field theory (QFT): a mathematical construct that attempts to explain particle interactions by treating the particles as excitations of quantum fields that permeate all of space-time. As can be expected, QFT requires advanced mathematical and physics concepts to describe a system that is both quantum and relativistic. The calculational and numerical techniques required to accomplish this feat are still being developed and improved by ongoing research.

In order for these theoretical calculations to be verified by experimental results, they must work towards predicting something that is physically observable. One such measurable is the *cross-section* of a particle process. The cross-section is an effective cross-sectional area that quantifies the likelihood of the interaction occurring. The goal of this body of work is to determine all the components required to do a cross-section calculation and measurement for a particular process, which will be described below.

The *Colour Glass Condensate* (CGC) [3–12] is an effective field theory that attempts to explain effects seen in nuclear collisions by describing the initial conditions. The starting point is to depict the highly Lorentz-boosted nuclei before the collision as dense media of *partons* that are dominated by gluons. How the two nuclei interact depends on how much they overlap. The situation of interest here is an *ultra-peripheral* heavy ion collision, in which there is no nuclear interaction between the two nuclei because the collision impact parameter is more than twice the sum of their radii.

Due to the strong electromagnetic fields generated by the heavy ions, the ultra-peripheral interaction is dominated by *photonuclear processes*[*]. The photon flux is proportional to the square of the nuclear charge, so photonuclear processes are particularly important in heavy ion collisions versus proton-proton collisions. In the case that the only particles in the final state are remnants of the photon and the second nucleus (considered the target), the interaction is called *exclusive*. If there are more particles in the final state then it is termed *inclusive*. Interactions are further classified as *coherent* or *incoherent*, depending on whether the photon interacts with the whole target or just one nucleon in a target that has broken up, respectively.

In the case that the photon interacts with a single nucleon in the second nucleus (considered the target), the interaction is called *coherent*. The target nucleus remains intact in such an interaction. Alternatively, the photon may interact with the target nucleus as a whole, in which case the interaction is called *incoherent*.

In either case, the interaction is energetic enough to facilitate particle production. An array of final-state particles may be considered but in this thesis, the focus will be on the J/Ψ vector-meson. This particle is a bound state, consisting of a charm quark and an anti-charm quark. It has zero charge, spin

[*]It is also possible for the two nuclei to interact purely electromagnetically. In such a case, both nuclei emit a photon which then interact with each other. Processes of this kind are called *photon-photon* interactions.

1 (hence, vector-meson) and a mass of 3.096 GeV/c^2. The J/Ψ is an unstable particle with a lifetime of approximately 7×10^{-21} seconds [13]. Its decay products are dictated by its intrinsic properties, with the products of the two principal decays being an electron-positron pair and a muon-antimuon pair. The various decay channels are not given equal weighting. In fact, the J/Ψ only decays in the muon channel 5.93% of the time; this fraction is called the branching ratio.

J/Ψ vector-mesons are an ideal candidate to study as a link between theoretical calculations in the CGC context and experimental analyses using nuclear collision data. This work illustrates the first steps in a cross-section calculation for exclusive J/Ψ production in heavy ion collisions from both viewpoints, theory and experiment. As such, the thesis is divided into two parts. Part `I` begins with a chapter dedicated to the CGC. It also introduces the main mathematical tool at the heart of the theory, the *JIMWLK* (Jalilian-Marian−Iancu−McLerran−Weigert−Leonidov−Kovner) evolution equation [14–21,27,28,60–64]. For reasons that will be motivated in Chapter 2, an approximation to the equation must be considered - the *Gaussian Truncation* (GT). The GT has already been established in the literature [2] and is discussed in Chapter 3. It is used in this thesis, as the starting point for further investigations, which follow in Chapter 4. Finally, Part `I` is concluded with a chapter describing the explicit cross-section expression required to be calculated within the CGC framework.

This is followed by Part `II`, the experimental feasibility study that attempts to describe how one would go about measuring the cross-section for exclusive J/Ψ production in the ATLAS detector [31] at the LHC [32]. It begins with a description of the LHC and ATLAS in Chapter 7. Then in Chapter 8, a Monte Carlo event generator is used to simulate a heavy ion collision. The simulation provides a sample of exclusively-produced J/Ψ's that can be used to determine the ATLAS detector's response to events of interest. Before one can get to that, however, and even before the theory done in Part `I`, a brief preliminary chapter will be provided to describe the introductory material needed in the bulk of the thesis.

Chapter 1

Preliminaries

This opening chapter provides the preliminary concepts required to tackle both a theoretical calculation and an experimental measurement of a cross-section. The chapter begins with a section on the Standard Model, with priority given to quantum chromodynamics (QCD) - the QFT describing the strong force. Then Section 1.2 introduces the cross-section from the viewpoints of the experimentalist and the theorist. Finally, Section 1.3 concludes the chapter with a general description of collider experiments. Priority is given to the detector relevant in this thesis, the ATLAS detector at the LHC. Natural units have been assumed throughout ($c = \hbar = 1$), which means that time has units of length and momentum and mass have units of energy.

1.1 The Standard Model

The Standard Model is a theory that describes all known elementary particles and their interactions with each other. These elementary particles are point-like objects that live in four-dimensional space-time but occupy no volume. It is assumed that all ordinary matter in the universe is made of these particles, which interact in the same way wherever they are. They are characterised by their intrinsic properties such as mass, spin and electric charge. On the first level, the particles are categorised

according to spin: fermions have half-integer spin and bosons have integer spin. Each category and the particles belonging to it, is shown in Figures 1.1 and 1.2*.

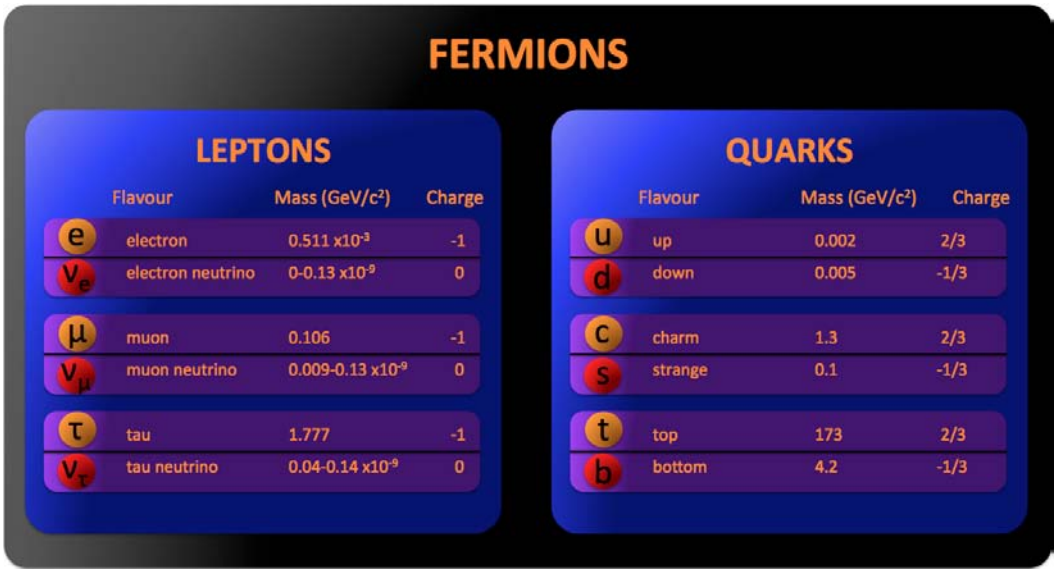

Figure 1.1: The spin-$\frac{1}{2}$ particles of the Standard Model and their mass and electric charge.

Figure 1.2: The integer-spin particles of the Standard Model and their mass, spin and electric charge. Also shown are the forces that they mediate.

*The experimental measurement of the mass of the Higgs boson is given in [33] and [34]. It is quoted as 125.3 ± 0.4 (stat) ± 0.5 (sys) GeV and 126.0 ± 0.4 (stat) ± 0.4 (sys) GeV, respectively.

The fermions are further separated into leptons (with integer charge) and quarks (with fractional charge). Quarks are unique to leptons in that, in addition to electric charge, they possess another characteristic called *colour charge*. All the fermions also have antiparticle equivalents, not shown in Figure 1.1. Particle-antiparticle partners have the same mass but the opposite sign for all other properties.

The fermions interact via three of the four fundamental forces of nature: the electromagnetic, weak and strong forces. The fourth force, gravity, is not included in the Standard Model since it is very weak at the small distances at which the theory is probed. While it is generally agreed that there must be some quantum mechanical theory of gravity, there is not yet (despite many years of effort), a theory called "Quantum Gravity". Each type of force in the Standard Model is mediated by a particular boson, as denoted in the last column of Figure 1.2.

The last boson in Figure 1.2, the Higgs boson, is a distinctive particle that has caused a lot of excitement around the world in the past few years. It is a prediction of the Standard Model that accounts for the mass of all fundamental particles, as explained by the *Higgs mechanism* (first proposed in 1964 in two independent papers [35], [36]). Since the theory makes no prediction for the boson's mass, the experimental search has been extremely challenging. In 2012, two experiments at the LHC, ATLAS and CMS, announced that they had observed a "Higgs-like" particle in proton-proton collisions [33], [34]. Further investigation was required to check the fundamental properties of this new particle and in 2013, its spin and parity were discovered to be consistent with that of the Standard Model Higgs boson [37].

The theory of the electromagnetic force is described by a QFT called quantum electrodynamics (QED). It is mediated by the photon and applies to all fermions with electric charge. The electromagnetic force is fairly well understood and has also been unified with the weak force. The combined description is called electroweak theory (EWK). Finally, strong interactions are accounted for by a QFT called quantum chromodynamics (QCD). There are several intricacies that make QCD a rich and complicated theory. These details will be discussed in Section 1.1.2 and the consequences of their complexities will make an appearance throughout Part `I` of this thesis. The interested reader is directed to [38–40] for pedagogic discussions on QFT. Here, a foray into the mathematics of QCD.

1.1.1 Group-theoretical prerequisites for QCD

The mathematical description of the Standard Model begins with a Lagrangian density, $\mathcal{L}(\varphi_i, \partial_\mu \varphi_i)$, that gives the action when integrated over all space-time: $S = \int d^4x\, \mathcal{L}(\varphi_i, \partial_\mu \varphi_i)$. It depends on fields, $\varphi_i(x)$, and their four-gradients, $\partial_\mu \varphi_i(x) = \frac{\partial \varphi_i(x)}{\partial^\mu x}$, where $i = 1, 2, ..., n$ for n fields. These in turn depend on a four-vector, $x^\mu = (t, x, y, z)$, denoting space-time. There are three types of fields in the Standard Model: scalars (like the Higgs field), vectors (like the gluon field) and spinors (like the fermion fields). Analogously to classical mechanics, the equations of motion describing the kinematics of the particles are obtained by applying the variational principle to the action S.

It is important to understand the underlying symmetries of the theory, since these lead to crucial conserved quantities fundamental to the system. A symmetry arises when a transformation applied to $\mathcal{L}$ renders it invariant. Such transformations may either be local (x-dependent) or global (x-independent). If $\mathcal{L}$ is invariant under a continuous group of *local* transformations, then the theory is called a *gauge theory**. The invariance of $\mathcal{L}$ under a continuous group of *global* transformations leads to one of the most profound theorems in field theory: Noether's theorem. This states that each continuous global symmetry has an associated conservation law, for example: energy conservation from time-translational symmetry or linear momentum conservation from space-translational symmetry.

These global symmetries can be categorised according to the subgroups of the General Linear group

$$\mathrm{GL}(n, \mathbb{K}) := \{A \in \mathbb{K}^{n\times n} | \det \neq 0\} \tag{1.1}$$

(where $\mathbb{K} = \mathbb{C}, \mathbb{R}$). $\mathrm{GL}(n, \mathbb{K})$ and its proper subgroups are continuous groups called matrix *Lie groups*. The subgroups relevant to the Standard Model are the n-degree Unitary and Orthogonal groups

$$\mathrm{U}(n) := \{A \in \mathrm{GL}(n, \mathbb{C}) | A^\dagger A = 1\} \tag{1.2}$$

$$\mathrm{O}(n) := \{A \in \mathrm{GL}(n, \mathbb{R}) | A^t A = 1\}. \tag{1.3}$$

and the Special Unitary and Special Orthogonal groups

$$\mathrm{SU}(n) := \{A \in \mathrm{GL}(n, \mathbb{C}) | A^\dagger A = 1, \det(A) = 1\} \tag{1.4}$$

$$\mathrm{SO}(n) := \{A \in \mathrm{GL}(n, \mathbb{R}) | A^t A = 1, \det(A) = 1\} \tag{1.5}$$

*The term *gauge* refers to the redundant degrees of freedom in $\mathcal{L}$, which are typically eliminated by *gauge fixing* in practical calculations.

(made "special" by imposing the additional requirement $\det(A) = 1$ on $\mathrm{U}(n)$ and $\mathrm{O}(n)$). One can also define a Lie algebra for each group G by

$$\mathfrak{g} := \{X \in \mathbb{K}^{n\times n} | e^{sX} \in G \; \forall s \in \mathbb{R}\}. \tag{1.6}$$

The algebra is a vector space spanned by a basis constructed of the *generators* t^a $(a = 1, 2, ..., \dim(\mathfrak{g}))$ of the group.

Since the context of this thesis entails knowledge of special relativity, a group-theoretical discussion on this level would be incomplete without brief mention of Lorentz transformations. One begins with all transformations of the kind

$$x^\mu \to \Lambda^\mu_\nu x^\nu \tag{1.7}$$

that constitute the *homogeneous Lorentz group*. These transformations leave the metric $g^{\mu\nu}$ invariant, i.e.

$$g^{\mu\nu} = \Lambda^\mu_\alpha \Lambda^\nu_\beta g^{\alpha\beta}. \tag{1.8}$$

In addition, affine transformations of the kind

$$x^\mu \to \Lambda^\mu_\nu x^\nu + a^\mu, \tag{1.9}$$

constitute the *Poincaré group*. These transformations leave relativistic distances $(x-y)^\mu g_{\mu\nu}(x-y)^\nu$ between two space-time points, x and y, invariant.

Groups in general may be represented in one of several ways. The representation dictates how the group acts on a vector space. Two representations are of interest in this thesis:

- The *fundamental* representation of a group G is the inclusion map of G into $\mathrm{GL}(n)$ and is used to define the group by the standard way in which it acts on a vector space. Similarly, $\mathfrak{g}$ is included into $\mathrm{gl}(n, \mathbb{K})$, the algebra of $\mathrm{GL}(n, \mathbb{K})$.
- The *adjoint* representation, $\mathtt{Ad}$, of a group G, maps G to $\mathrm{GL}(\mathfrak{g})$ via $\mathtt{Ad}A(X) = AXA^{-1}$. Similarly, $\mathtt{ad}$ maps $\mathfrak{g}$ to $\mathrm{gl}(\mathfrak{g})$ via $\mathtt{ad}X(Y) = [X, Y] \in \mathfrak{g}$ (if the commutator $[X, Y] = XY - YX$ is zero then the group is called *Abelian*, otherwise it is called *non-Abelian*) The adjoint matrix can be written as $\tilde{A}^{ab} = 2\mathrm{tr}(t^a A t^b A^{-1})$ where t^a are the generators*.

*To see this, express $X \in \mathfrak{g}$ in terms of generators t^a as $X^a t^a$ and use $X^a = 2\mathrm{tr}(t^a X)$ to write $AXA^{-1} = AX^b t^b A^{-1} = t^a(2\mathrm{tr}(t^a A t^b A^{-1})X^b) = t^a \tilde{A}^{ab} X^b$.

The Standard Model Lagrangian density, $\mathcal{L}_{\mathrm{SM}}$, is a monstrously long expression, since it must account for all fundamental particles and their interactions. It is best understood in parts, in terms of the three fundamental forces it describes. QED is an Abelian U(1) gauge theory. Unified electroweak theory and QCD are both Yang-Mills theories, meaning that they are non-Abelian gauge theories based on the SU(N) group. In particular, EWK is a U(1)×SU(2) theory and QCD is an SU(3) theory.

1.1.2 QCD in a nutshell

All particles with colour charge, namely quarks and gluons, experience the strong force. QCD is more complicated than QED because unlike electromagnetic charge, colour has three degrees of freedom (called red, green and blue)*. Quarks carry one colour and antiquarks one anticolour; they transform in the fundamental representation. Gluons on the other hand, are bicoloured, carrying superpositions of colour-anticolour states. The i^{th} state can be obtained by calculating the product

$$|i\rangle = (r, g, b)\, t^a \begin{pmatrix} r \\ g \\ b \end{pmatrix} \tag{1.10}$$

where r, g, b are the three possible colours. This means that gluons transform in the adjoint representation. Recall from the previous section that the dimension of the algebra dictates the number of generators. In the case that there are three colours, $\dim(\mathrm{su}(3)) = 3^2 - 1 = 8$ so there are eight gluons in total. Since gluons are the mediators of the strong force and themselves carry colour, they have the unique ability to self-couple (unlike photons). This characteristic makes QCD far richer than QED.

Another distinguishing feature of QCD is that isolated quarks have not been observed. Instead, they occur in colourless bound states called *hadrons*: *mesons* are quark-antiquark states and *baryons* are 3-quark states. Mesons are further split into *pseudo-scalar-mesons* (spin-0) and *vector-mesons* (spin 1). Essentially all of matter is made up of only two of these hadrons: the proton (*uud* quarks) and the neutron (*udd* quarks). They are the most stable hadrons, proton decay being theorised to take longer than the age of the universe and the neutron lifetime measured to be 885.7 seconds. Other hadrons

*QCD is an SU group of dimension $3^2 - 1$ because of the $N = 3$ colour degrees of freedom (N is the degree of the fundamental representation. In some instances, it may be profitable to consider calculations in the more generic context of an SU(N) group, where N can represent any number of colours.

typically have a lifetime around $10^{-24} - 10^{-8}$ seconds, after which they decay to particles with smaller mass.

QCD is encapsulated in the QCD Lagrangian, which requires the gauge-covariant gluon field strength tensor,

$$G^a_{\mu\nu} = \partial_\mu \mathcal{A}^a_\nu - \partial_\nu \mathcal{A}^a_\mu + g f^{abc} \mathcal{A}^b_\mu \mathcal{A}^c_\nu, \tag{1.11}$$

analogous to the electromagnetic field strength tensor, $F_{\mu\nu}$, in QED. Here, $\mathcal{A}^a_\mu(x)$ are gluon fields in the adjoint representation of SU(3) with colour index a, g is the coupling strength and f^{abc} are the completely antisymmetric structure constants of SU(3) such that $[t^a, t^b] = i f^{abc} t^c$. They can be determined using the expression $f^{abc} = 2i \,\mathrm{tr}(t^a, [t^b, t^c])$.

Now for the QCD Lagrangian:

$$\mathcal{L}_{\mathrm{QCD}} = i\bar{\psi}_i \Big[(\gamma^\mu D_\mu[A])_{ij} - m\delta_{ij} \Big] \psi_j - \frac{1}{4} G^a_{\mu\nu} G^{\mu\nu}_a, \tag{1.12}$$

which is gauge invariant under local transformations of the kind

$$\psi(x) \to U_x \psi(x) \qquad \text{and} \qquad A_\mu \to U_x \Big(A_\mu + \frac{i}{g} \partial_\mu \Big) U_x^\dagger \implies D_\mu[A] \to U_x D_\mu[A] U_x^\dagger. \tag{1.13}$$

(In the Abelian case, A_μ would transform as $A_\mu \to A_\mu - \frac{1}{g}\partial_\mu \alpha(x)$).

Here, $\psi_i(x)$ is the quark field in the fundamental representation of SU(3) with quark flavour indices i, j and $\overline{\psi} := \psi^\dagger \gamma^0$ where the dagger denotes the transpose complex conjugate (or hermitian conjugate) and γ^0 is a Dirac matrix given below. $D_\mu = \partial_\mu - ig A^a_\mu t^a$ is the gauge covariant derivative and m represents the quark masses. γ^μ are the Dirac matrices that, in the Weyl representation, are given by

$$\gamma^0 := \begin{pmatrix} 1 & 0 \\ 0 & -1 \end{pmatrix}, \qquad \gamma^i := \begin{pmatrix} 0 & \sigma_i \\ -\sigma_i & 0 \end{pmatrix}, \qquad \gamma^5 := i\gamma^0\gamma^1\gamma^2\gamma^3 = \begin{pmatrix} 0 & 1 \\ 1 & 0 \end{pmatrix} \tag{1.14}$$

where σ_i are the Pauli matrices from SU(2),

$$\sigma_1 := \begin{pmatrix} 0 & 1 \\ 1 & 0 \end{pmatrix}, \qquad \sigma_2 := \begin{pmatrix} 0 & -i \\ i & 0 \end{pmatrix}, \qquad \sigma_3 := \begin{pmatrix} 1 & 0 \\ 0 & -1 \end{pmatrix}. \tag{1.15}$$

One of the key elements of QCD hidden in $\mathcal{L}_{\mathrm{QCD}}$ is the coupling strength, $g = \sqrt{4\pi\alpha_s}$. In QED, α is small enough to facilitate expansion methods like perturbation theory, with typical values around

1/137 for interactions in the GeV energy range. The QCD situation is not so convenient, what with α_s having the energy-dependent behaviour

$$\alpha_s(|q^2|) = \frac{\alpha_s(\mu^2)}{1 + \frac{\alpha_s(\mu^2)}{12\pi}\Big(11n - 2f\Big)\ln\left(\frac{|q^2|}{\mu^2}\right)}, \qquad |q^2| \gg \mu^2. \tag{1.16}$$

Here, q and μ are energies, q defined by the probe and μ a renormalisation scale used to define a cutoff

$$\ln \Lambda_{\mathrm{QCD}}(\mu^2) = \ln \mu^2 - \frac{12\pi}{\Big(11n - 2f\Big)\alpha_s(\mu^2)}. \tag{1.17}$$

Perturbation theory breaks down beyond Λ_{QCD}. n and f are the numbers of colours and quark flavours in the theory, respectively. In the Standard Model, $n = 3$ and $f = 6$. Figure 1.3 shows various experimental measurements of α_s as well as the QCD prediction. At low energies (corresponding to large distance scales), the largeness of the coupling means that quarks in a bound state are tightly confined to each other, a phenomenon known as *confinement*. At large energies (corresponding to small distance scales), the coupling becomes very small and perturbative techniques can be used to do calculations using α_s as the expansion parameter. This is a region known as *asymptotic freedom*.

In the non-perturbative regions of QCD, one must utilise more innovative calculational techniques to obtain results. There are several methods on the market that have been established to deal with large α_s calculations. One such method is lattice QCD, in which space-time points are discretised and numerical methods are used to perform calculations on powerful computers. In fact, this works for all values of α_s. Alternative methods and effective theories exist, like QCD sum rules and $1/N$ expansions. The Colour Glass Condensate (CGC), which is the context of this thesis, is an effective theory that attempts to explain the physics of heavy ion collisions by understanding initial-state effects. It is valid for small values of the coupling but in regions of phase space where factors of α_s appear with other large factors, rendering perturbation theory ineffective.

1.2 Observables: the Cross-section

With the theoretical basis of particle physics established in the previous section, the goal of calculations in this context must now be presented. In order for theory to make connections to experiment, it needs to predict something that can be physically measured. One such observable is an interaction cross-section - an effective cross-sectional area measured in units of barns (1 b $= 10^{-28}$ m^2) that depends

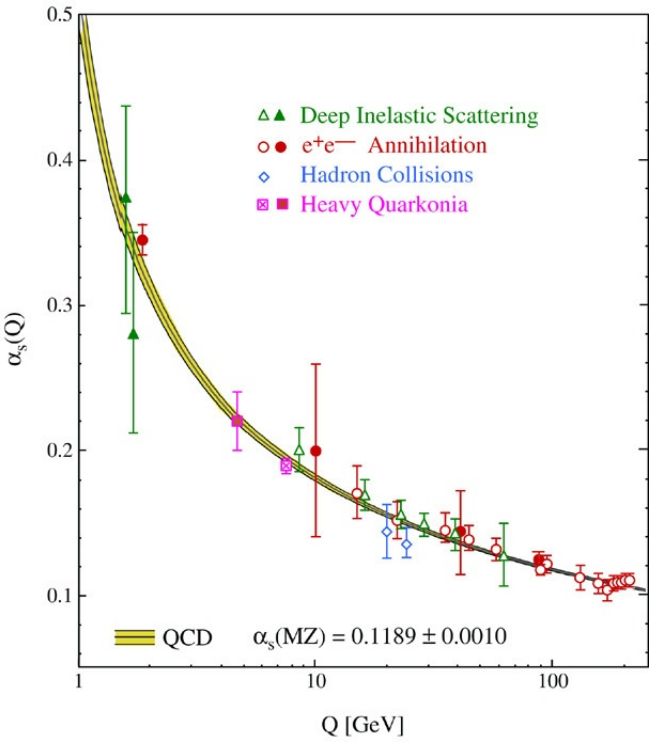

Figure 1.3: The running of the coupling α_s as a function of energy, as measured by various experiments [41].

on both the incoming and outgoing particles in the interaction. Given the many different elementary particles and the array of bound states that they can form, a plethora of fundamental interactions can occur when particles are collided at relativistic speeds. The cross-section of a process quantifies the probability of a particular interaction (as opposed to the many others) occurring. Naturally, this observable is extremely difficult to determine since it depends on the inherent characteristics of the interacting particles as well as their kinematics, which are determined by the experimental setup. A generic cross-section calculation will be demonstrated in this section, first from the perspective of the experimentalist and then the theorist.

1.2.1 Experimental cross-section measurement

The total cross-section, σ, quantifies how particles can interact in all ways and requires a summation over all possible processes i:

$$\sigma = \sum_{i=1}^{n} \sigma_i \tag{1.18}$$

where σ_i refers to one process in particular. If one considers a hard scattering experiment in which incident particles are aimed at a target, then the differential cross-section may be more useful: $\frac{d\sigma}{d\Omega}$. This is a measure of the number of interactions per target particle that scatters within a solid angle segment $d\Omega$ at an angle θ from the collision axis, per number of incident particles per unit area. The total cross-section can be obtained from the differential cross-section by integrating over all values of the solid angle: $\sigma = \int d\Omega \frac{d\sigma}{d\Omega}$.

In particle colliders, the more routine scenario involves an incoming beam of particles, where the beam's *instantaneous luminosity*, $\mathcal{L}$, is a measure of the particle flux (the number of particles per unit area per unit time) in units of $\mathrm{cm}^{-2}\mathrm{s}^{-2}$. The number of scattered particles can be obtained from the luminosity via

$$N_{\mathrm{scat}} = \sigma \int dt\mathcal{L} \tag{1.19}$$

where $\int dt\mathcal{L}$ is called the *integrated luminosity*, usually measured in units of pb^{-1}. The machine luminosity, $L = \int dt\mathcal{L}$, is dictated purely by beam parameters, such as the number of particles per bunch, the number of bunches per beam, the revolution frequency, the relativistic boost factor and the beam emittance.

To account for detector imperfections, Equation 1.19 needs to be modified to incorporate detector *acceptance* and *efficiency*. Acceptance, A, corrects for candidate events lost due to selection criteria that depend on kinematic factors. It is typically found from Monte Carlo studies by dividing the number of Monte Carlo events that pass these kinematic cuts by the total number of events. Efficiency, ε, corrects for events lost due to selection criteria associated with the trigger, event reconstruction and identification (all of which will be elaborated upon in Part II). The efficiency is very much dependent on the type of analysis being done. Taking these into account, Equation 1.19 becomes

$$\sigma = \frac{N - N_{\mathrm{B}}}{A\varepsilon \int dt\mathcal{L}} \tag{1.20}$$

where N is the total number of events, N_{B} is the number of background events (events that pass the

selection criteria but are likely from other processes) and $N_{\mathrm{S}} = N - N_{\mathrm{B}}$ is the number of signal events (events that are relevant to the process being studied).

While the final cross-section calculation in an experimental analysis seems trivial, determining each of the factors in these expressions requires extensive work. Each step must also take into account all sources of uncertainty and a full uncertainty analysis is required in addition to the final cross-section value that is quoted.

1.2.2 Theoretical cross-section calculation

The underpinning of the cross-section lies in the *scattering matrix* S. To see this, one must begin with the probability P of the process in question. The number of scattering events N when r particles are incident on a single target is

$$N = \int d^2b\, n_{\mathrm{in}}\, P(\boldsymbol{b}) \tag{1.21}$$

where n_{in} is the number of incoming particles per unit area and $P(\boldsymbol{b})$ is the probability that a given incoming particle has impact parameter $\boldsymbol{b}$. The total cross-section is then

$$\sigma = \frac{N}{n_{\mathrm{in}}} = \int d^2b\, P(\boldsymbol{b}). \tag{1.22}$$

A standard scattering experiment involves two incoming particles, a and b, and several outgoing particles, say n. A schematic of this process is shown in Figure 1.4 using a diagram called an *n-point function* (where n is the number of external legs in the diagram). If each of these interacting particles is represented by a wave-packet ϕ then the probability that the scattering will occur is given by

$$P(a\,b \to 1\,2\,...\,n) = \Big|\, \langle \phi_1 \phi_2 \,...\, \phi_n | \phi_a \phi_b \rangle \,\Big|^2. \tag{1.23}$$

The *in-state*, $|\phi_a \phi_b\rangle$, is taken in the remote past and the *out-state*, $\langle \phi_1 \phi_2 \,...\, \phi_n|$, is taken in the remote future.

Each state $|\phi\rangle$ in Equation 1.23 is a Fourier transform,

$$|\phi\rangle = \int \frac{d^3k}{(2\pi)^3} \frac{1}{\sqrt{2E_{\boldsymbol{k}}}} \phi(\boldsymbol{k})\, |\boldsymbol{k}\rangle \tag{1.24}$$

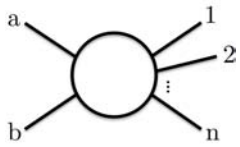

Figure 1.4: A schematic representation of a 2-to-n scattering event ($2+n$-point function) in which the incoming particles are labelled a and b and the outgoing particles are labelled $1, 2, ..., n$.

and each ϕ is an independent wave-packet localised in space. The factor $\frac{1}{\sqrt{2E_{\boldsymbol{k}}}}$ is a consequence of requiring the integration measure to be Lorentz invariant*. In the simplified case in which there are no other quantum numbers (like spin and colour) to account for, Equation 1.23 can just as well be written in terms of a momentum-state *transition amplitude*,

$$_{\text{out}}\left\langle \boldsymbol{p}_1\boldsymbol{p}_2 ... \boldsymbol{p}_n|\boldsymbol{k}_a\boldsymbol{k}_b\right\rangle_{\text{in}} \tag{1.25}$$

where $\boldsymbol{k}$'s refer to incoming particles and $\boldsymbol{p}$'s refer to outgoing particles.

Now all that is left to do to get to the S-matrix is to recognise that out-states are in-states that have been time-evolved according to the (unitary) evolution operator e^{-iHt} where H is the relevant Hamiltonian of the theory. Since the in- and out-states are in the remote past and future respectively, one has

$$\begin{aligned} _{\text{out}}\left\langle \boldsymbol{p}_1\boldsymbol{p}_2 ... \boldsymbol{p}_n|\boldsymbol{k}_a\boldsymbol{k}_b\right\rangle_{\text{in}} &= \lim_{T\to\infty} {}_T\left\langle \boldsymbol{p}_1\boldsymbol{p}_2 ... \boldsymbol{p}_n|\boldsymbol{k}_a\boldsymbol{k}_b\right\rangle_{-T} &(1.26)\\ &= \lim_{T\to\infty} \left\langle \boldsymbol{p}_1\boldsymbol{p}_2 ... \boldsymbol{p}_n\right| e^{-iH(2T)} \left|\boldsymbol{k}_a\boldsymbol{k}_b\right\rangle &(1.27)\\ &=: \lim_{T\to\infty} \left\langle \boldsymbol{p}_1\boldsymbol{p}_2 ... \boldsymbol{p}_n\right| S \left|\boldsymbol{k}_a\boldsymbol{k}_b\right\rangle . &(1.28)\end{aligned}$$

The S-matrix is therefore a sequence of limiting unitary operators that contains knowledge of the scattering interaction. If no interaction occurs, then $S = \mathbb{1}$. This trivial piece can be separated out of the S-matrix by defining the T-matrix according to

$$S =: \mathbb{1} + iT. \tag{1.29}$$

S and T should preserve four-momentum conservation and therefore always contain a factor

*For an invariant test function $f(k)$,

$$\int \frac{d^4k}{(2\pi)^4} 2\pi\delta^{(4)}(k^2 - m^2) f(k) = \int \frac{d^3k}{(2\pi)^3} \frac{1}{2E_{\boldsymbol{k}}} f(E_{\boldsymbol{k}}, \boldsymbol{k})$$

is still consistent with Lorentz transformations. $2E_{\boldsymbol{k}}\delta^{(3)}(\boldsymbol{k}' - \boldsymbol{k})$ is an invariant so define $|\boldsymbol{k}\rangle := \sqrt{2E_{\boldsymbol{k}}} a^\dagger_{\boldsymbol{k}} |0\rangle$ as the normalised state in a free theory, where $a^\dagger_{\boldsymbol{k}}$ is a creation operator.

$\delta^{(4)}\Big(k_a + k_b - \sum_{i=1}^{n} p_i\Big)$. It is conventional to write this factor explicitly, the remaining part of the S- or T-matrix being defined as a new object, $\mathcal{M}$:

$$\langle \boldsymbol{p}_1 \boldsymbol{p}_2 \ldots \boldsymbol{p}_n |\, iT \,| \boldsymbol{k}_a \boldsymbol{k}_b \rangle =: \left[(2\pi)^4 \delta^{(4)}\Big(k_a + k_b - \sum_{i=1}^{n} p_i\Big) \right] i\mathcal{M}\Big(k_a, k_b \to p_1, p_2, ..., n\Big). \tag{1.30}$$

After some lengthy algebra that will not be done here (see [40]), the differential cross-section can be written in terms of $\mathcal{M}$ as

$$d\sigma = \frac{1}{2E_a\, 2E_b\, |v_a - v_b|} \Big(\prod_f \int \frac{d^3 p_f}{(2\pi)^3} \frac{1}{2E_f} \Big) \Big| \mathcal{M}\Big(p_a, p_b \to \{p_f\}\Big) \Big|^2 \left[(2\pi)^4 \delta^{(4)}\Big(p_a + p_b - \sum_f p_f\Big) \right]. \tag{1.31}$$

where f denotes the final-state and $|v_a - v_b|$ is the relative velocity of the two beams in the laboratory reference frame.

$\mathcal{M}$ is an invariant matrix element called the *scattering amplitude* and remains the only thing that needs to be calculated in order to determine the cross-section of a particular process. This calculation is done using Feynman rules, a procedure that begins with drawing every possible Feynman diagram for an interaction and using standard prescriptions to write down the corresponding mathematical expressions. Each diagram constitutes a contribution to the scattering amplitude. The Feynman rules for calculating typical Feynman diagrams can be found in graduate textbooks such as [40]. These will not be discussed here since the CGC theory requires somewhat different diagrams, as will be revealed in Part `I`.

Obtaining the cross-section from $\mathcal{M}$ relies on the *optical theorem*: the imaginary part of the scattering amplitude is proportional to the cross-section. This comes from using the definition of the S-matrix and its unitarity property to write

$$-i(T^\dagger - T) = T^\dagger T. \tag{1.32}$$

For the case of 2-to-2 scattering, one can use Equation 1.30 to write this expression in terms of $\mathcal{M}$:

$$\begin{aligned} -i\Big[\mathcal{M}\Big(k_1 k_2 \to p_1 p_2\Big) - \mathcal{M}^*\Big(p_1 p_2 \to k_1 k_2\Big) \Big] = \sum_n \left[\prod_{i=1}^{n} \int \frac{d^3 q_i}{(2\pi)^3} \frac{1}{2E_i} \right] \\ \times \mathcal{M}^*\Big(p_1 p_2 \to \{q_i\}\Big) \mathcal{M}\Big(k_1 k_2 \to \{q_i\}\Big) \left[(2\pi)^4 \delta^{(4)}\Big(k_1 k_2 - \sum_i q_i\Big) \right] \end{aligned} \tag{1.33}$$

where q_i refer to momenta of final-state particles. This expression is shown pictorially in Figure 1.5. Working through the algebra of kinematic factors, one obtains

$$\mathrm{Im}\, \mathcal{M}\Big(k_1, k_2 \to k_1, k_2\Big) = 2E_{\mathrm{cm}}\, p_{\mathrm{cm}}\, \sigma(k_1, k_2 \to \text{anything}), \tag{1.34}$$

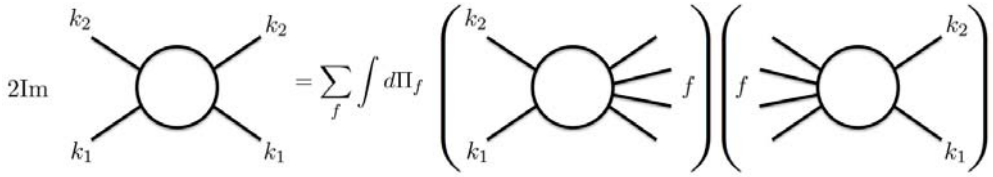

Figure 1.5: A 2-to-2 scattering (4-point function) where the righthand side requires a sum over all possible final states.

which is the standard form of the optical theorem. This can be used to calculate the cross-section after the scattering amplitude has been determined in a particular scenario.

1.3 Collider Experiments

It has already been noted that today's scattering experiments, like RHIC [42] and the LHC, employ fairly high energies. In order for the relevant degrees of freedom in a particle collision to be the elementary particles of the Standard Model, centre-of-mass energies around GeV and even TeV are required (compared to everyday scales, like the mass of a proton, which is approximately 1 MeV). The experimentalist's approach to accessing these energies is to use oscillating electromagnetic fields to accelerate charged particles to relativistic speeds and then collide them. The electric fields are used to accelerate the particles through a series of radio frequency cavities; the magnetic fields are used to bend and control the beams. The best beam candidates for such experiments are electrons and protons due to their stability. There are, however, a variety of physics motivations for using other particles, particularly heavier nuclei like gold and lead.

The two main classes of accelerators are categorised according to their topology. Linear accelerators, or *linacs*, consist of straight particle beams. These are typically used for low-energy physics experiments and medical applications. The best example of a linac is the Stanford Linear Collider at SLAC (Stanford Linear Accelerator Centre) in California. It is the longest linear collider in the world, measuring in at a length of 3 km.

The second class of accelerators has a circular geometry and relies heavily on magnetic fields supplied

by superconducting magnets to bend the beams. The most modern circular accelerator design is the *synchrotron*, an accelerator concept that has enabled particle physicists to build large-scale colliders like the Tevatron [43] at Fermilab, Chicago, and HERA (Hadron-Electron Ring Accelerator) [44] at DESY, Hamburg. The most powerful collider of all time, however, is housed at CERN (European Organisation for Nuclear Research) in Geneva - the LHC.

There are several advantages to linacs and synchrotrons, depending on the type of physics processes being studied. Linacs are capable of achieving much higher energies with heavy ion beams, which are otherwise limited in synchrotrons by the magnetic field strength required to control them. Since electrons travelling in an arc lose much of their energy through radiation, electron beams are better suited to linacs. Also, if a continuous stream of particles is required, then linacs are the best bet (synchrotrons provide periodic bursts of particles, called bunches). In practice, linacs are not able to achieve as high energies as circular machines; the main advantage of linacs is the higher luminosity.

Circular accelerators on the other hand, have their own redeeming features. For one, continuous acceleration is possible since particles can travel indefinitely in the ring. Synchrotrons in particular, have an innovative design that allows their mandatory components to be separated into several parts. For example, instead of having one massive magnet covering the entire particle orbit, magnetic fields can be provided by several smaller magnets dispersed around the ring. One of the major advantages of a circular accelerator is its size - an extremely long linac is required to match the power of what could be a much smaller circular accelerator. Linacs also need bigger power supplies and a lot of expensive, specialist material to deal with the high energies of beams. The most powerful circular collider, the LHC, will now be discussed in more detail.

1.3.1 The Large Hadron Collider

CERN (initially *Conseil Européen pour la Recherche Nucléaire*) is an international scientific research facility on the French-Swiss border, founded in 1952 by 12 European countries. As of the beginning of 2014, the organisation consists of 21 Member States and 92 other affiliated countries, making it one of the most collaborative international initiatives in history. CERN's primary objective is to probe the fundamental constituents of matter through a series of high-energy experiments. This goal comes in two parts: i) studying the Standard Model and ii) testing theories beyond the Standard Model. In particular, the experiments at CERN wish to understand how matter obtains mass, the nature of dark matter and dark energy, the matter-antimatter asymmetry in the universe and the evolution of matter from the Big Bang to present day. Thus far, the work done at this institution has resulted in several Nobel prizes, most notably the 2013 Nobel Prize in physics which was awarded to Peter Higgs and Francois Englert for their work on the Higgs mechanism (verified after a Higgs-like particle was observed in the LHC in 2012).

The LHC is CERN's crowning glory. It is the world's newest and largest particle collider, capable of colliding protons and heavy ions at unprecedented centre-of-mass energies. It is located in a 26.7 km long circular tunnel, 45 - 170 m underground. A photo taken inside the LHC tunnel is shown in Figure 1.6. Running at design capabilities, the LHC will be able to collide protons (p) at 14 TeV with a luminosity of 10^{34} cm^{-2}s^{-1} and heavy ions (HI), specifically lead ($^{208}Pb^{82+}$), at 2.76 TeV per nucleon with a peak luminosity of 10^{27} cm^{-2}s^{-1} [32].

Unlike particle-antiparticle colliders, which only have one ring for two the beams, the LHC has two separate rings with counter-rotating beams that cross at four points along the tunnel. These are the locations of the four major detectors: ATLAS, CMS, ALICE and LHCb:

- ATLAS (A Toroidal LHC ApparatuS) is a general-purpose detector, capable of detecting both proton and heavy ion collisions.
- CMS (Compact Muon Solenoid) [45] is another general-purpose detector.
- ALICE (A Large Ion Collider Experiment) [46] is the only experiment dedicated to heavy ion collisions, with the primary focus of understanding the quark-gluon plasma*.

*This is a medium of quarks and gluons theorised to form in heavy ion collisions. It is widely believed that the

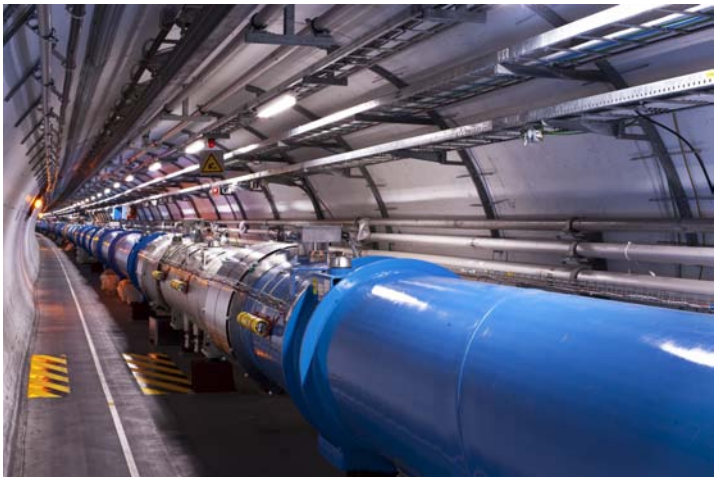

Figure 1.6: A photo taken inside the LHC tunnel [51].

- LHCb (Large Hadron Collider bottom) [47] specialises in b-physics (physics concerning the bottom flavour quark) with the hopes of understanding CP violation. It also conducts analyses concerning bound charm quark states, like the J/Ψ and Υ vector-mesons.

An aerial view photo of Geneva is shown in Figure 1.7 with a drawing of the position of the LHC tunnel as well as the locations of these four detectors. There are also three smaller detectors at the LHC: LHCf [48], TOTEM [49] and MoEDAL [50]. These are more specialised machines, dedicated to forward neutral pion detection, small-angle elastic scattering and highly ionising stable massive particles, respectively.

The experimental work done in this thesis concerns the ATLAS detector. A more detailed exposition on the detector and the computing infrastructure used by the collaboration will be given at the beginning of Part II. For the sake of comparison, results concerning exclusive vector-meson production performed by CMS, ALICE and LHCb will also be included.

universe was a quark-gluon plasma a few seconds after the Big Bang.

Figure 1.7: An aerial view of CERN and the LHC taken in 2008 [52].

Part I:

Theory

Chapter 2

The Colour Glass Condensate

The CGC effective theory has already been mentioned briefly in the Introduction. In this chapter, the most prominent concepts of the theory will be discussed in some detail. Recall that the processes under consideration in this work are photonuclear interactions. The most probable scenario is that one of the nuclei emits a virtual photon with four-momentum q^μ. This photon then splits into a projectile with coloured components, typically a quark-antiquark pair at leading order. The colour-netural *quark dipole* can interact with the second nucleus, with four-momentum p^μ, via the strong force. It is this complicated photonuclear interaction between the projectile and target nucleus that is the subject of this chapter. Figure 2.1 shows a visual representation of this kind of process. In high-energy colliders like the LHC, these interactions are energetic enough to facilitate particle production.

The chapter is divided into three sections. Section 2.1 describes the light-cone coordinate system used throughout Part I. It goes on to explain what the CGC is by depicting the target nucleus as a dense gluonic field and explaining the saturation effects that lead to the novel features of this medium. Then in Section 2.2, the *quark dipole picture* is introduced to describe the strong interaction between the projectile and the target as depicted by the CGC. Finally, in Section 2.3 the energy evolution of this interaction is explained using the JIMWLK equation. The discussion below largely follows that of [1].

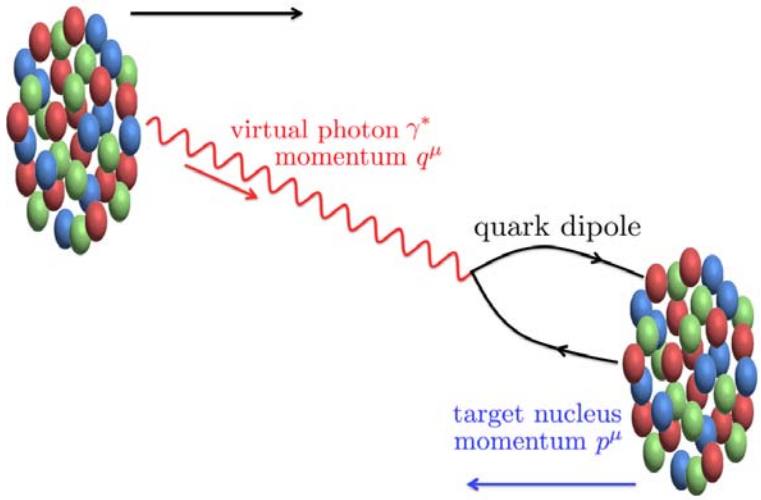

Figure 2.1: A photonuclear interaction in which one nucleus emits a virtual photon, which then interacts with the second nucleus via the strong force.

2.1 Saturation at Low-x_{Bj}

2.1.1 Light-cone coordinates

Before colliding particles in a high-energy scattering experiment, they must be accelerated to close to the speed of light. If a particle with Minkowski coordinate four-vector $x^\mu = (t, x, y, z)^*$ travelling at speed v_x is boosted along the x-direction by a factor $\gamma := \frac{1}{\sqrt{1-\beta^2}}$ (where $\beta := v_x/c$) to a reference frame in which it is travelling at speed $\tilde{v}_x$, then its Lorentz-transformed four-vector is given by

$$\tilde{x}^\mu = \Lambda^\mu{}_\nu \, x^\nu \qquad \text{where} \qquad \Lambda^\mu{}_\nu = \begin{pmatrix} \gamma & -\gamma\beta & 0 & 0 \\ -\gamma\beta & \gamma & 0 & 0 \\ 0 & 0 & 1 & 0 \\ 0 & 0 & 0 & 1 \end{pmatrix}. \tag{2.1}$$

*The metric is defined as

$$g^{\mu\nu} := \begin{pmatrix} 1 & 0 & 0 & 0 \\ 0 & -1 & 0 & 0 \\ 0 & 0 & -1 & 0 \\ 0 & 0 & 0 & -1 \end{pmatrix}$$

such that $I := g_{\mu\nu} x^\mu x^\nu$ is a Lorentz-invariant.

This implies dilation in the temporal component and contraction in the x-spatial component: $\tilde{t} = \gamma t$ and $\tilde{x} = x/\gamma$. All observable particles are physical and obey the *on-shell condition*, $p^\mu p_\mu = m^2$, where $p^\mu = (E, p_x, p_y, p_z)$ is the four-momentum given in terms of energy E and three-momentum $\boldsymbol{p} = (p_x, p_y, p_z)$ and m is the particle's mass. The photon in Figure 2.1 is virtual in the sense that it is off-shell and cannot be observed in a final state.

Since the underlying physics in a collision is frame-independent, there is freedom in a calculation to choose a convenient system of coordinates that makes the mathematics simpler. Instead of Minkowski coordinates $x^\mu = (x^0, x^1, x^2, x^3)$, define *light-cone coordinates*

$$x^+ := \frac{1}{\sqrt{2}}(x^0 + x^1) \tag{2.2}$$

$$x^- := \frac{1}{\sqrt{2}}(x^0 - x^1) \tag{2.3}$$

$$\boldsymbol{x} := (x^2, x^3)\,. \tag{2.4}$$

This transforms the metric $g^{\mu\nu}$ to

$$\begin{pmatrix} 1 & 0 & 0 & 0 \\ 0 & -1 & 0 & 0 \\ 0 & 0 & -1 & 0 \\ 0 & 0 & 0 & -1 \end{pmatrix} \quad \longrightarrow \quad \begin{pmatrix} 0 & 0 & 0 & 1 \\ 0 & 0 & 0 & 0 \\ 0 & 0 & -1 & 0 \\ 1 & 0 & 0 & -1 \end{pmatrix}. \tag{2.5}$$

Writing the boost factor as rapidity $Y := \ln\gamma$, a Minkowski four-vector boosted in the x^1-direction transforms according to

$$\begin{pmatrix} x^0 \\ x^1 \\ x^2 \\ x^3 \end{pmatrix} \quad \longrightarrow \quad \begin{pmatrix} \cosh Y & \sinh Y & 0 & 0 \\ \sinh Y & \cosh Y & 0 & 0 \\ 0 & 0 & 1 & 0 \\ 0 & 0 & 0 & 1 \end{pmatrix} \begin{pmatrix} x^0 \\ x^1 \\ x^2 \\ x^3 \end{pmatrix}, \tag{2.6}$$

which in light-cone coordinates becomes

$$\begin{pmatrix} x^+ \\ x^- \\ x^2 \\ x^3 \end{pmatrix} \quad \longrightarrow \quad \begin{pmatrix} e^Y & 0 & 0 & 0 \\ 0 & e^{-Y} & 0 & 0 \\ 0 & 0 & 1 & 0 \\ 0 & 0 & 0 & 1 \end{pmatrix} \begin{pmatrix} x^+ \\ x^- \\ x^2 \\ x^3 \end{pmatrix}. \tag{2.7}$$

Notice that the x^+-component gets enhanced by a factor e^Y. It can therefore be interpreted as being time-dilated so the x^+-direction acts like light-cone time. Similarly, the x^--component gets reduced

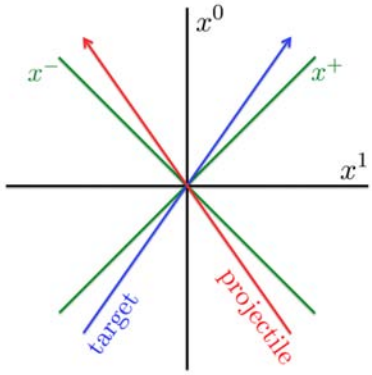

Figure 2.2: Light-cone coordinates x^+ and x^- shown in the x^0-x^1 plane.

by e^{-Y}, which can be thought of as getting length-contracted, implying the x^--direction behaves like a spatial direction. Consider the case in which the target nucleus travels in the x^+-direction and the projectile travels in the x^--direction. During the interaction, the target then resembles a highly Lorentz-contracted object from the viewpoint of the projectile. Figure 2.2 shows the new light-cone coordinates on a Minkowski diagram with the target and projectile directions aligned along their respective axes.

2.1.2 Low-x_{Bj} and the target nucleus

Another useful quantity is *Bjorken-x* (x_{Bj}),

$$\frac{1}{x_{\mathrm{Bj}}} = e^Y = \gamma \qquad \Longrightarrow \qquad Y = -\ln x_{\mathrm{Bj}}. \tag{2.8}$$

It is defined in terms of the photon and target momenta q and p (as shown in Figure 2.1) according to

$$x_{\mathrm{Bj}} := \frac{-q^2}{2p^\mu q_\mu}. \tag{2.9}$$

The photon momentum is a critical parameter, so it is convenient to express it as a positive quantity by defining $Q^2 := -q^2 > 0$. Then x_{Bj} can also be written as $x_{\mathrm{Bj}} = \frac{Q^2}{s}$ where s is the centre-of-mass energy* of the collision. From this expression, it can be seen that high energies correspond to low-x_{Bj}.

Let us now turn the spotlight on the target nucleus, whose internal structure can be probed through *deep inelastic scattering* (DIS). These are experiments in which leptons emit virtual photons that are

*$s = (p+q)^2$ is an invariant quantity and acts as the largest scale in the problem. It becomes $s = 2p^\mu q_\mu$ for large s.

used to probe hadrons at very high energies. High energies correspond to having a probe with good resolution, which is necessary to access the internal configurations of the hadrons. In the case of DIS, this translates to the photon having a large momentum. The results from DIS studies can be extended to nuclear collisions, since nuclei are just collections of protons and neutrons. In that case, x_{Bj} has the interpretation of the fraction of momentum p carried by the parton in the nucleus that the photon hits.

The question is: how does the structure of the hadron change as a function of energy, particularly at low-x_{Bj}? This has been answered using DIS data from HERA and a fitting method that entails solving the *DGLAP equation* (Dokshitzer-Gribov-Altarelli-Parisi equation) [55, 56]. The DGLAP equation is a linear differential equation describing the Q^2 evolution of quark and gluon distribution functions in the hadron. The differential equation may be extracted by standard perturbative methods but the initial conditions require experimental input. As such, measurements over a range of Q^2 are required to extract this non-perturbative information. The results of this procedure are shown in Figure 2.3 for gluon distributions at various, fixed Q^2. DGLAP is only valid at relatively high values of Q^2 and small x_{Bj}.

The main feature eminent in Figure 2.3 is the large growth of the gluon distributions as x_{Bj} becomes small. This behaviour can be explained fairly simply: as energy increases, the gluons already present in the hadron emit more gluons. This self-interaction characteristic of gauge bosons is a unique feature of a non-Abelian theory like QCD. Thus gluons act as further sources of emission, producing more gluons and densely populating the hadron as energy increases. The corresponding quark distributions are not shown here because they show similar behaviour.

2.1.3 Gluon saturation

DGLAP provides a sufficient description for the evolution of the internal structure of the nucleus as a function of energy at large, fixed Q^2. Figure 2.3 also shows that the gluon distributions grow faster the smaller x_{Bj} is. In this region, the dominant large logarithm is $\ln \frac{1}{x_{\mathrm{Bj}}}$ instead of $\ln Q^2$. The first attempt to resum these logarithms is the *BFKL equation* (Balitsky-Fadin-Kuraev-Lipatov equation) [53, 54]. Unlike the DGLAP equation, the BFKL equation met with only limited phenomenological success. The underlying reason for this was addressed for the first time with the advent of the BK and JIMWLK

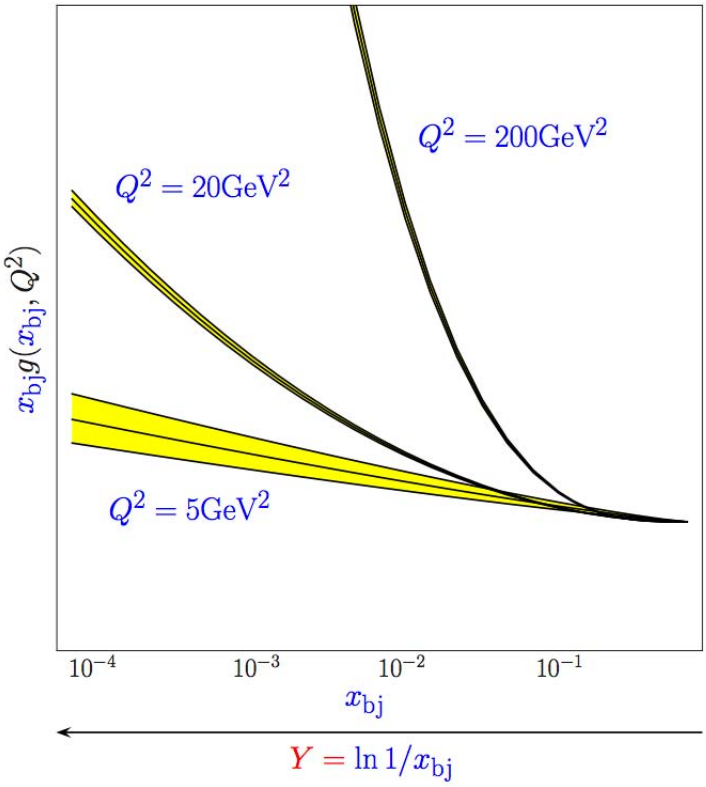

Figure 2.3: Qualitative gluon growth distributions for various Q^2 from typical DGLAP fits of DIS at HERA [1]. Quark distributions follow a similar behaviour.

evolution equations, which generalise the BFKL equation into a domain where gluon distributions become large and nonlinear effects become non-negligible. Even without the mathematical machinery needed to formulate these equations, the generic physical situation is easily described by referencing a $Q^2 - x_{\text{Bj}}$ phase space diagram.

This diagram is shown in Figure 2.4 along with demarcations for DGLAP and BFKL where they are applicable. The nucleus is represented by a collection of partons whose apparent size is given by $\frac{1}{Q^2}$. The quarks and gluons are actually point particles, as discussed in the previous chapter, but their measured size is dependent on the resolution of the experimental probe. Since a larger Q^2 will allow for better resolution, it is inversely proportional to the parton size. At very small values of x_{Bj}, gluons dominate the nucleus. The effect of gluon growth with increasing energy is also shown in this figure - as x_{Bj} decreases, more gluons are observed.

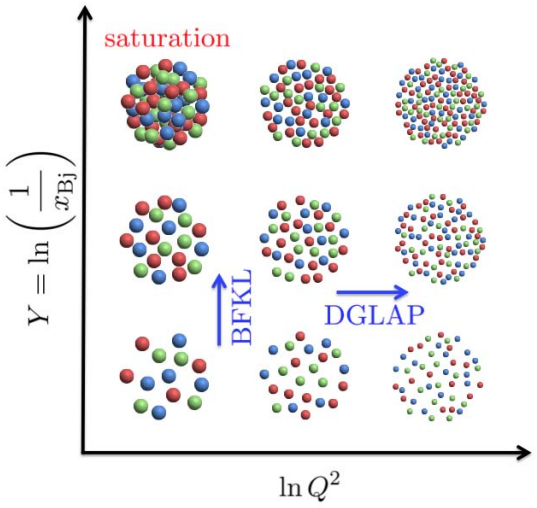

Figure 2.4: $Q^2 - x_{\mathrm{Bj}}$ phase diagram with partons represented as dots.

At the top left corner of the phase diagram, where Q^2 and x_{Bj} are small, the nucleus looks very dense. It is this region where non-linearities are important and a treatment using full JIMWLK evolution becomes necessary. In this region of phase space, there are many partons with large apparent size and so they begin to overlap. The system can no longer be treated as a dilute sea of quarks and gluons that are not correlated (in which case both linear evolution equations BFKL and DGLAP, fall short). Gluons that overlap begin to recombine, thus counteracting the growth observed in the likes of Figure 2.3. At small enough x_{Bj}, this recombination effect leads to gluon saturation and parton numbers stabilise.*

The saturated gluonic medium that forms at small-Q^2 and small-x_{Bj} is the CGC. *Colour* refers to the charge of SU(3), relevant because it is the non-Abelian nature of QCD that allows for gluon recombination. *Glass* refers to the glass-like behaviour the medium exhibits - it acts like a solid on short timescales but like a fluid on long timescales. Finally, *condensate* refers to the saturation effect that characterises the medium. It is important to note that, despite the misleading jargon, there is no phase transition involved in the CGC. Neither DGLAP nor BFKL are able to predict saturation since neither account for recombination. A new mathematical model is therefore required to deal with this corner of the phase diagram: JIMWLK evolution, which will be saved for the end of the chapter.

*Saturation does not show itself at large Q^2 and small x_{Bj}. In this region, partonic size is regulated by the largeness of Q^2 so that high densities do not lead to overlapping.

2.1.4 The target as a background field

At this point, there is a qualitative picture of the target nucleus as a dense medium of gluons, called the CGC. In order to describe the quark dipole interaction with this medium, it is necessary to have a mathematical description for it.

Recall that the target's trajectory has been aligned with the x^+-axis and the projectile's with the x^--axis. By choice of reference frame, there is only one important degree of freedom in the target field, b^μ, which manifests in the +-component. The Lorentz contraction of this b^+ component in the x^--direction can be taken to an extreme if the projectile's momentum is large enough (x_{Bj} must be small enough). In that case, the x^- contribution becomes a delta function, $\delta(x^-)$, and the field can be written as

$$b^\mu = \Big(\beta(\boldsymbol{x})\delta(x^-),\, 0,\, 0,\, 0\Big) \tag{2.10}$$

where $\beta(\boldsymbol{x})$ is a function of transverse coordinates only. It has no x^+-dependence, which means that this direction is left unprobed. The resulting field strength tensor has components

$$G^{i+}(x) = \delta(x^-)\partial^i\beta(\boldsymbol{x}) \tag{2.11}$$

and zero otherwise.

The field represented by Equation 2.10 is, in fact, not the whole story. b^μ only represents the kinematically enhanced contribution to the gluon field. In addition to this, there may be kinematically suppressed factors, δA^μ, so that the actual gauge field is

$$A^\mu = b^\mu + \delta A^\mu. \tag{2.12}$$

δA^μ represents quantum corrections to the leading contribution, b^μ, that correspond to further gluon emission over and above this background. These corrections may be dealt with perturbatively, which is why it is useful to separate them from b^μ.

2.2 The Dipole Picture

2.2.1 The eikonal approximation and Wilson lines

In order for the virtual photon to interact with the target field, it will need to manifest in a colour-apparent way. The simplest colour configuration that it can assume is a quark-antiquark pair, as depicted in Figure 2.1. Since the photon is colourless, this quark dipole is too, but the individual quark and antiquark at least have a chance to interact strongly with the target. This section explains the nature of that interaction.

Since the background field is localised in the x^--direction, any projectile travelling along the x^--axis will propagate freely except exactly at $x^- = 0$, where it encounters the target. Due to the large momentum carried by the dipole, this localised interaction is insufficient for the target to deflect it in transverse directions and so it manages to punch straight through the target field. It does, however, undergo a phase rotation. The interaction between the dipole and target is said to *eikonalise*.

Wilson lines in the fundamental representation of SU(3) are used to account for this. These are path-ordered exponentials that depend on the transverse coordinate at which the projectiles punch through the field.* The Wilson line for a quark that interacts with the target at position $\boldsymbol{z}$ is

$$U_{\boldsymbol{z}} := \mathrm{P}\exp\left\{-ig\int_{-\infty}^{\infty} dx^- b^+(0,x^-,\boldsymbol{x})\right\} \tag{2.14}$$

where liberty has been taken to write only the +-component of the target field, since the other three components are zero. For an antiquark, the Hermitian conjugate of $U_{\boldsymbol{z}}$ applies:

$$U_{\boldsymbol{z}}^\dagger = \mathrm{P}\exp\left\{ig\int_{\infty}^{-\infty} dx^- b^+(0,x^-,\boldsymbol{x})\right\}. \tag{2.15}$$

*The starting point is a propagator for a massless scalar field in a background gauge field,

$$\frac{-i}{D^2[b]}(y,z) = \int_0^\infty ds \int_z^y [dx]\exp\Big\{-\int_0^s d\kappa\,\frac{\big(\dot{x}(\kappa)\big)^2}{4}\Big\}\,\mathrm{P}\exp\Big\{-ig\int_z^y dx^\mu\, b_\mu(x)\Big\} \tag{2.13}$$

where the path-integral is over trajectories x (parametrized by κ) that connect y ($\kappa = 0$) to z ($\kappa = s$). Substituting in Equation 2.10, the path-ordered exponential in this expression reduces to

$$\mathrm{P}\exp\Big\{-ig\int_z^y dx^\mu\, b_\mu(x)\Big\} = \mathrm{P}\exp\Big\{-ig\int_z^y dx^- b^+(0,x^-,\boldsymbol{x})\Big\}.$$

See [57] for a full exposition.

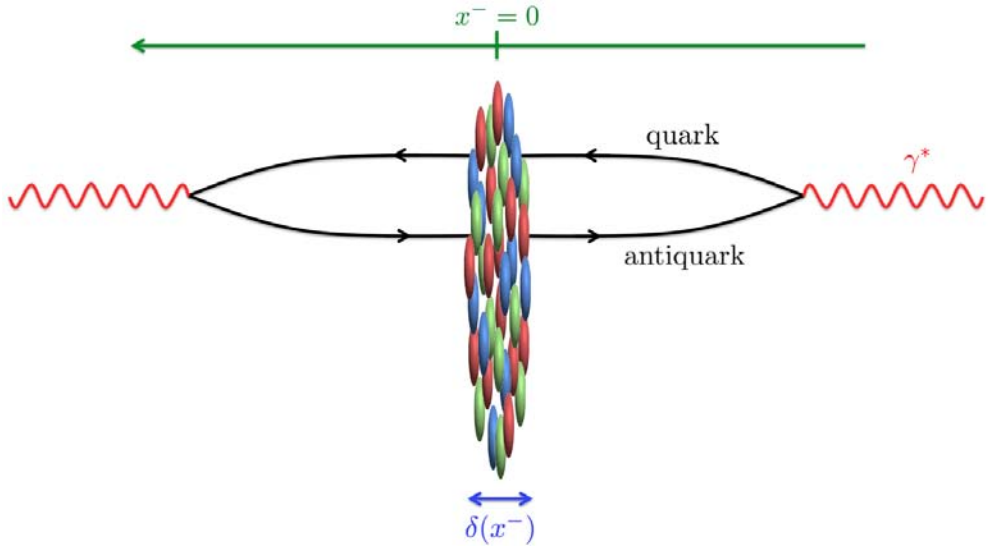

Figure 2.5: Interaction of a quark dipole with a fully Lorentz-contracted target field. Light-cone time runs from right to left.

The integral over x^- runs backwards in this case because the antiquark is thought of as a quark propagating "backwards in time".

The limits of the integrals in Equations 2.14 and 2.15 are infinite because the quark and antiquark are considered to propagate from very early time to very late time. In reality, they would form from the photon projectile at some finite time before $x^- = 0$ and recombine into a photon at some finite time after $x^- = 0$. It is also possible to replace the local degrees of freedom in the target field with these non-local Wilson lines according to

$$b^+_{\boldsymbol{z}} = i(\partial^+ U_{\boldsymbol{z}})U^\dagger_{\boldsymbol{z}} \tag{2.16}$$

where $b_{\boldsymbol{z}} = b(0, z^-, \boldsymbol{z})$ is in the group algebra.

Figure 2.5 shows the full propagation of the projectile. The part of interest, the interaction with the target, is best represented by a Feynman diagram as shown in Figure 2.6a. The bottom grey object is the target, the target field is represented by the blue vertical line and the two black horizontal lines are the quark and antiquark. They pick up Wilson lines $U_{\boldsymbol{u}}$ and $U^\dagger_{\boldsymbol{v}}$ (shown by the pink forward and reverse arrowheads, respectively) as they interact with the background field. The virtual photons will not be shown. These kinds of diagrams will be used throughout Part I and will prove very useful when

Figure 2.6: a) A dipole-target interaction. b) A dipole-target interaction in which the dipole emits a gluon, that passes through the target field and then gets reabsorbed by the dipole.

more complicated projectiles are considered.

In the next chapter, it will also be necessary to consider what happens when a projectile gluon interacts with the target. Instead of a Wilson line of the kind above, a path-ordered exponential in the adjoint representation of SU(3) is used:

$$\tilde{U}_{\boldsymbol{z}}^{ab} = 2\mathrm{tr}(t^a U_{\boldsymbol{z}} t^b U_{\boldsymbol{z}}^{\dagger}). \tag{2.17}$$

Note that

$$\left[\tilde{U_{\boldsymbol{z}}}^{\dagger}\right]^{ab} = \left[\tilde{U_{\boldsymbol{z}}}\right]_{ba} = \left[\tilde{U_{\boldsymbol{z}}}^{-1}\right]_{ab}. \tag{2.18}$$

A typical diagram with a gluon Wilson line is shown in Figure 2.6b. It is actually a sum of four diagrams, since gluon emission and absorption can occur with either the quark or the antiquark. All four combinations are accounted for by the vertices represented by the black arrowheads on the quark lines. At each quark-gluon vertex, a group generator is allocated. Their colour indices must correspond to those in the adjoint Wilson line where the gluon interacts with the field. The non-Abelian nature of the theory manifests in the path-ordering of the Wilson line, since the order of interactions along the path of integration must be preserved to ensure that these non-commuting generators are kept ordered.

There is one final constraint that must be made to Wilson lines as shown in Figure 2.6. Because the initial-state and final-state photons are colourless, the net colour interaction between the dipole and the target must be colourless. This means that Figure 2.6a is actually a trace of the form $\mathrm{tr}(U_{\boldsymbol{u}} U_{\boldsymbol{v}}^{\dagger})$. Similarly, Figure 2.6b is $\tilde{U}_{\boldsymbol{z}}^{ab}\,\mathrm{tr}(t^a U_{\boldsymbol{u}} t^b U_{\boldsymbol{v}}^{\dagger})$. The easiest way to read these expressions off the diagrams is by traversing the entire loop and writing down all contributions obtained along the way. Using the diagrammatic ingredients introduced in these two diagrams, it is possible to draw more complicated interactions, such as those between an arbitrary number of dipoles and the target field.

2.2.2 DIS cross-section and the dipole correlator

The ultimate goal of this thesis is to write down an expression for the cross-section of a particular process. It may, therefore, be useful to provide a brief outline for a prototype calculation using the dipole picture - the total cross-section for DIS. A full discussion is provided in [1].

By the optical theorem discussed in Section 1.2.2, one must calculate the imaginary part of the scattering amplitude in order to calculate a cross-section. This amplitude has two parts: a trivial piece, denoting no interaction with the background field and a non-trivial piece, containing all the interaction information. The cross-section is then the difference between these two contributions. Using the appropriate expressions for propagators in both scenarios (propagators of the kind in Equation 2.13) and the optical theorem, it can be shown after an involved calculation that the cross-section is given by

$$\sigma_{\mathrm{DIS}}(x_{\mathrm{Bj}},Q^2)=\int d^2\boldsymbol{r}\int_0^1 d\alpha\Big|\psi(\alpha,\boldsymbol{r}^2,Q^2)\Big|^2\int d^2\boldsymbol{b}\left\langle\frac{\mathrm{tr}(1-U_{\boldsymbol{x}}U_{\boldsymbol{y}}^\dagger)}{N_c}+\frac{\mathrm{tr}(1-U_{\boldsymbol{y}}U_{\boldsymbol{x}}^\dagger)}{N_c}\right\rangle \tag{2.19}$$

where $\boldsymbol{r}=\boldsymbol{x}-\boldsymbol{y}$ is the transverse size of the dipole and $\boldsymbol{b}=\frac{1}{2}(\boldsymbol{x}+\boldsymbol{y})$ is the impact parameter. ψ is the photon wave-function, α is the longitudinal momentum fraction of the the quark or antiquark and N_c is the number of colour degrees of freedom in the theory. This can be simplified to

$$\sigma_{\mathrm{DIS}}(x_{\mathrm{Bj}},Q^2)=2\int d^2\boldsymbol{r}\int_0^1 d\alpha\Big|\psi(\alpha,\boldsymbol{r}^2,Q^2)\Big|^2\int d^2\boldsymbol{b}\left\langle\frac{\mathrm{tr}(1-U_{\boldsymbol{x}}U_{\boldsymbol{y}}^\dagger)}{N_c}\right\rangle, \tag{2.20}$$

provided that the individual terms are real.

Equation 2.20 can be examined in two independent parts. The first part, $\int d^2r\int_0^1 d\alpha\big|\psi(\alpha,\boldsymbol{r}^2,Q^2)\big|^2$, contains the information relevant for the photon-quark vertex at which the photon splits into a quark-antiquark pair. It represents the probability that the photon (whose momentum dictates Q^2) splits into a quark dipole of size r. This integral is fairly well understood in terms of QED.

The second part of Equation 2.20 is the dipole cross-section

$$\sigma_{\mathrm{dipole}}(Y,r^2):=2\int d^2\,\boldsymbol{b}\hat{N}_{Y,\boldsymbol{xy}} \tag{2.21}$$

where

$$\hat{N}_{Y,\boldsymbol{xy}}:=\left\langle\frac{\mathrm{tr}(1-U_{\boldsymbol{x}}U_{\boldsymbol{y}}^\dagger)}{N_c}\right\rangle_Y \tag{2.22}$$

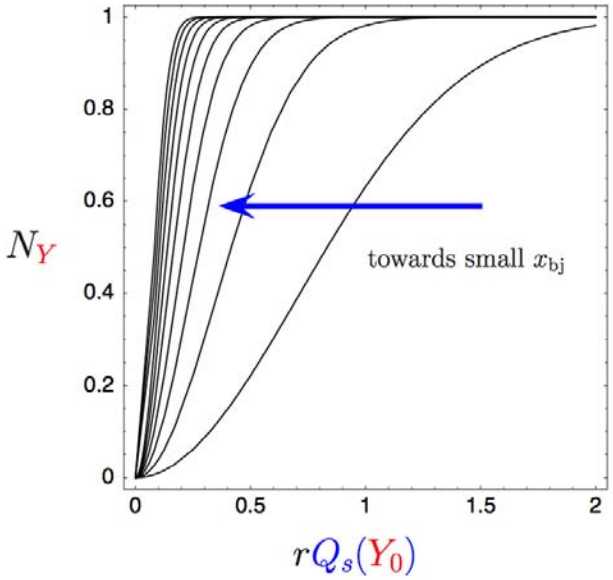

Figure 2.7: Evolution of $\hat{N}_{Y,\boldsymbol{xy}}$ as a function for various Y [1]. Each curve is a function of the saturation scale, Q_s, which characterises the transition between colour-transparency and saturation in the target.

is the expectation value of the *dipole correlator*. The integral over b ensures that σ_{dipole} scales with the transverse size of the target and vanishes completely outside of it. σ_{dipole} contains all information about the dipole interaction with the target field. Notice that there is no information in it about the intrinsic properties of the quark and antiquark. This means that their quantum numbers are preserved throughout the interaction.

Figure 2.7 shows the behaviour of $\hat{N}_{Y,\boldsymbol{xy}}$ from a phenomenological study. Since the product $U_{\boldsymbol{x}}U^{\dagger}_{\boldsymbol{y}}$ takes on values between zero and one, so too does $\hat{N}_{Y,\boldsymbol{xy}}$. In the absence of a target, $U_{\boldsymbol{x}} = U^{\dagger}_{\boldsymbol{y}} = \mathbb{1}$. $\hat{N}_{Y,\boldsymbol{xy}}$ then becomes zero as it should because there is no interaction occurring. The rightmost curve corresponds to an initial rapidity Y_0; increasing Y results in the curves moving left and approaching a step function. This means that saturation sets in sooner as energy is increased.

It will be the task of the remainder of Part `I` to try to apply this procedure for calculating a cross-section to nuclear collisions. Both the QED and QCD integrals in Equation 2.20 will need to be determined, since our interest is in a final-state vector-meson, not a virtual photon.

2.3 JIMWLK Evolution

Evolution equations like DGLAP and BFKL discussed in the previous section are good for describing the dipole-target interaction before saturation. After saturation, the particle correlations leading to recombination effects need to be accounted for to correctly describe the physics. This is the power of JIMWLK evolution.

2.3.1 The JIMWLK equation

The JIMWLK equation is a nonlinear, functional differential equation derived by requiring that the total cross-section is independent of rapidity Y. The first step in deriving the evolution equation is to note that the averaging procedure over Y of a correlator (as in Equation 2.22) describes all the information about the background field. The dipole correlator above is written in terms of Wilson lines, which have an implicit Y-dependence. To make this dependence more explicit, one may write the averaging of any correlator $F[U]$ in terms of weights $\hat{Z}_Y[U]$:

$$\Big\langle F[U]\Big\rangle_Y = \int \hat{D}[U]\Big(F[U]\hat{Z}_Y[U]\Big) \tag{2.23}$$

where

$$\hat{D}[U] := D[U]\,\delta\big(UU^\dagger - \mathbb{1}\big)\,\delta\big(\det U - 1\big) \tag{2.24}$$

is the functional Haar measure*. In the case of the dipole, $F[U] = \mathrm{tr}(1 - U_{\boldsymbol{x}}U^\dagger_{\boldsymbol{y}})/N_c$.

In order to investigate the Y-dependence of $\hat{Z}_Y[U]$, Equation 2.23 can be differentiated:

$$\frac{d}{dY}\Big\langle F[U]\Big\rangle_Y = \frac{d}{dY}\int \hat{D}[U]\Big(F[U]\hat{Z}_Y[U]\Big) \tag{2.25}$$

$$= \int \hat{D}[U]\left(F[U]\frac{d}{dY}\hat{Z}_Y[U]\right). \tag{2.26}$$

On the other hand, $\frac{d}{dY}\langle F[U]\rangle_Y$ is just an energy evolution of an arbitrary correlator, $\langle F[U]\rangle_Y$, which can be written in terms of the governing Hamiltonian in the theory. In this case the JIMWLK Hamiltonian, $H_{\mathrm{JIMWLK}}[U]$, applies to the arbitrary $F[U]$:

$$\frac{d}{dY}\Big\langle F[U]\Big\rangle_Y = \Big\langle -H_{\mathrm{JIMWLK}}[U]F[U]\Big\rangle_Y. \tag{2.27}$$

*The Haar measure is an invariant used to define an integral for functions on a locally compact group by assigning an "invariant volume" to subsets of the group.

By using Equation 2.23, this can be written as

$$\frac{d}{dY}\Big\langle F\big[U\big]\Big\rangle_Y = \int \hat{D}\big[U\big]\bigg(\Big(-H_{\text{JIMWLK}}\big[U\big]F\big[U\big]\Big)\hat{Z}_Y\big[U\big]\bigg) \tag{2.28}$$

and after partial integration yields

$$\frac{d}{dY}\Big\langle F\big[U\big]\Big\rangle_Y = \int \hat{D}\big[U\big]F\big[U\big]\Big(-H_{\text{JIMWLK}}\big[U\big]\hat{Z}_Y\big[U\big]\Big). \tag{2.29}$$

Finally, combining Equations 2.26 and 2.29 gives

$$\int \hat{D}\big[U\big]\bigg(F\big[U\big]\frac{d}{dY}\hat{Z}_Y\big[U\big]\bigg) = \int \hat{D}\big[U\big]F\big[U\big]\Big(-H_{\text{JIMWLK}}\big[U\big]\hat{Z}_Y\big[U\big]\Big) \tag{2.30}$$

from which the JIMWLK equation can be extracted:

$$\frac{d}{dY}\hat{Z}_Y\big[U\big] = H_{\text{JIMWLK}}\big[U\big]\hat{Z}_Y\big[U\big]. \tag{2.31}$$

Equation 2.31 can be extracted from Equation 2.30 because $F\big[U\big]$ can be any U-object and therefore acts as a test function.

The Hamiltonian is an expression containing Wilson lines and differential operators

$$i\nabla^a_{\boldsymbol{u}} := -\big[U_{\boldsymbol{u}}t^a\big]_{ij}\,\frac{\delta}{\delta\big[U_{\boldsymbol{u}}\big]_{ij}} \qquad \text{and} \qquad i\bar{\nabla}^a_{\boldsymbol{u}} := \big[t^aU_{\boldsymbol{u}}\big]_{ij}\,\frac{\delta}{\delta\big[U_{\boldsymbol{u}}\big]_{ij}} \tag{2.32}$$

where

$$[i\nabla^a_{\boldsymbol{u}}, i\nabla^b_{\boldsymbol{v}}] = \delta^{(2)}_{\boldsymbol{uv}}f^{abc}i\nabla^c_{\boldsymbol{v}}, \qquad [i\bar{\nabla}^a_{\boldsymbol{u}}, i\bar{\nabla}^b_{\boldsymbol{v}}] = \delta^{(2)}_{\boldsymbol{uv}}f^{abc}i\bar{\nabla}^c_{\boldsymbol{v}} \qquad \text{and} \qquad [i\bar{\nabla}^a_{\boldsymbol{u}}, i\nabla^b_{\boldsymbol{v}}] = 0. \tag{2.33}$$

$i\nabla^a_{\boldsymbol{u}}$ and $i\bar{\nabla}^a_{\boldsymbol{u}}$ are related to each other by

$$i\nabla^a_{\boldsymbol{u}} = -\big[U^\dagger_{\boldsymbol{u}}\big]^{ab}i\bar{\nabla}^b_{\boldsymbol{u}} \qquad \text{and} \qquad i\bar{\nabla}^a_{\boldsymbol{u}} = -\big[U^\dagger_{\boldsymbol{u}}\big]^{ab}i\nabla^b_{\boldsymbol{u}}. \tag{2.34}$$

It is defined according to

$$H_{\text{JIMWLK}} := \frac{1}{2}\,i\nabla^a_{\boldsymbol{u}}\,\chi^{ab}_{\boldsymbol{uv}}\,i\nabla^b_{\boldsymbol{v}} \tag{2.35}$$

where

$$\chi^{ab}_{\boldsymbol{uv}} := \frac{\alpha_s}{\pi^2}\int d^2z\,\mathcal{K}_{\boldsymbol{uzv}}\Big[\big(1-U^\dagger_{\boldsymbol{u}}U_{\boldsymbol{z}}\big)\big(1-U^\dagger_{\boldsymbol{z}}U_{\boldsymbol{v}}\big)\Big]^{ab} \tag{2.36}$$

$\mathcal{K}_{\boldsymbol{uzv}}$ is a transverse coordinate-dependent kernel,

$$\mathcal{K}_{\boldsymbol{uzv}} = \frac{(\boldsymbol{u}-\boldsymbol{z})\cdot(\boldsymbol{z}-\boldsymbol{v})}{(\boldsymbol{u}-\boldsymbol{z})^2\,(\boldsymbol{z}-\boldsymbol{v})^2}. \tag{2.37}$$

H_{JIMWLK} can be written in a way that makes the interpretation of its terms more intuitive:

$$H_{\text{JIMWLK}} = \frac{\alpha_s}{2\pi^2}\int d^2z\,\mathcal{K}_{\boldsymbol{uzv}}\Big[i\nabla^a_{\boldsymbol{u}}i\nabla^a_{\boldsymbol{v}} + i\bar\nabla^a_{\boldsymbol{u}}i\bar\nabla^a_{\boldsymbol{v}} + \tilde U^{ab}_{\boldsymbol{z}}\big(i\nabla^a_{\boldsymbol{u}}i\bar\nabla^b_{\boldsymbol{v}} + i\bar\nabla^b_{\boldsymbol{u}}i\nabla^b_{\boldsymbol{v}}\big)\Big]. \tag{2.38}$$

This can be seen by re-expressing the factor

$$i\nabla^a_{\boldsymbol{u}}\Big[\big(1-U^\dagger_{\boldsymbol{u}}U_{\boldsymbol{z}}\big)\big(1-U^\dagger_{\boldsymbol{z}}U_{\boldsymbol{v}}\big)\Big]^{ab}i\nabla^b_{\boldsymbol{v}} \tag{2.39}$$

from the original definition of the Hamiltonian as

$$\begin{aligned}
&i\nabla^a_{\boldsymbol{u}}\Big[1+U^\dagger_{\boldsymbol{u}}U_{\boldsymbol{z}}U^\dagger_{\boldsymbol{z}}U_{\boldsymbol{v}} - U^\dagger_{\boldsymbol{u}}U_{\boldsymbol{z}} - U^\dagger_{\boldsymbol{z}}U_{\boldsymbol{v}}\Big]^{ab}i\nabla^b_{\boldsymbol{v}}\\
&= i\nabla^a_{\boldsymbol{u}}\delta^{ab}i\nabla^b_{\boldsymbol{v}} + i\bar\nabla^a_{\boldsymbol{u}}\delta^{ab}i\bar\nabla^b_{\boldsymbol{v}} - i\nabla^a_{\boldsymbol{x}}\Big[U^\dagger_{\boldsymbol{u}}U_{\boldsymbol{z}}\Big]^{ab}i\nabla^b_{\boldsymbol{v}} - i\nabla^a_{\boldsymbol{u}}\Big[U^\dagger_{\boldsymbol{z}}U_{\boldsymbol{v}}\Big]^{ab}i\nabla^b_{\boldsymbol{v}}\\
&= i\nabla^a_{\boldsymbol{u}}i\nabla^a_{\boldsymbol{v}} + i\bar\nabla^a_{\boldsymbol{u}}i\bar\nabla^a_{\boldsymbol{v}} - i\bar\nabla^a_{\boldsymbol{u}}\big[U_{\boldsymbol{z}}\big]^{ab}i\nabla^b_{\boldsymbol{v}} - i\nabla^a_{\boldsymbol{u}}\big[U^\dagger_{\boldsymbol{z}}\big]^{ab}i\bar\nabla^b_{\boldsymbol{v}}\\
&= i\nabla^a_{\boldsymbol{u}}i\nabla^a_{\boldsymbol{v}} + i\bar\nabla^a_{\boldsymbol{u}}i\bar\nabla^a_{\boldsymbol{v}} + \tilde U^{ab}_{\boldsymbol{z}}\big(i\nabla^a_{\boldsymbol{u}}i\bar\nabla^b_{\boldsymbol{v}} + i\bar\nabla^a_{\boldsymbol{u}}i\nabla^b_{\boldsymbol{v}}\big).
\end{aligned}$$

2.3.2 Action of the JIMWLK Hamiltonian

The interpretation of what H_{JIMWLK} does, relies on the definitions of the differential operators as given in Equation 2.32. Since functional derivatives of Wilson lines are

$$\frac{\delta}{\delta\big[U_{\boldsymbol{u}}\big]_{ij}}\big[U_{\boldsymbol{x}}\big]_{kl} = \delta_{ik}\delta_{jl}\delta^{(2)}(\boldsymbol{u}-\boldsymbol{x}) =: \delta_{ik}\delta_{jl}\delta^{(2)}_{\boldsymbol{ux}}, \tag{2.40}$$

$i\nabla^a_{\boldsymbol{u}}$ and $i\bar\nabla^a_{\boldsymbol{u}}$ act on them according to

$$i\nabla^a_{\boldsymbol{u}}U_{\boldsymbol{x}} = -U_{\boldsymbol{u}}t^a\delta^{(2)}_{\boldsymbol{ux}}, \qquad i\nabla^a_{\boldsymbol{u}}U^\dagger_{\boldsymbol{y}} = t^aU^\dagger_{\boldsymbol{u}}\delta^{(2)}_{\boldsymbol{uy}} \tag{2.41}$$

$$i\bar\nabla^a_{\boldsymbol{u}}U_{\boldsymbol{x}} = t^aU_{\boldsymbol{u}}\delta^{(2)}_{\boldsymbol{ux}}, \qquad i\bar\nabla^a_{\boldsymbol{u}}U^\dagger_{\boldsymbol{y}} = -U^\dagger_{\boldsymbol{u}}t^a\delta^{(2)}_{\boldsymbol{uy}}. \tag{2.42}$$

The appearance of a generator in the above expressions means that a quark-gluon vertex forms whenever a Wilson line is differentiated. This has been shown diagrammatically already, in Figure 2.6b. To be precise, consider the operations of $i\nabla^a_{\boldsymbol{u}}$ and $i\bar\nabla^a_{\boldsymbol{u}}$ on the product

$U_{\boldsymbol{x_1}}...U_{\boldsymbol{x_n}}U^\dagger_{\boldsymbol{y_1}}...U^\dagger_{\boldsymbol{y_n}} =$ 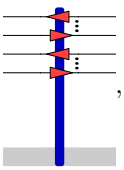 ,

a correlator of n quarks and n antiquarks. The differential operators insert quark-gluon vertices as follows:

The differential operators can act on any U or $U^\dagger$, so the gluon insertion lines

are actually sums over $2n$ terms, where the vertex dots represent interaction with the specific quark or antiquark. The point is that $i\nabla^a_{\boldsymbol{u}}$ inserts a gluon line to the right of the target and $i\bar{\nabla}^a_{\boldsymbol{u}}$ inserts a gluon line to the left of the target. Whether these lines are gluon emission or absorption lines depend on what other differential operators are acting on the correlator.

Instead of an arbitrary number of quarks and antiquarks, consider a single dipole. For the four terms in the JIMWLK Hamiltonian as written in Equation 2.38,

(2.43)

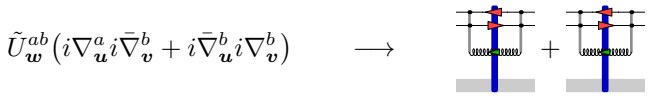

(2.44)

so altogether,

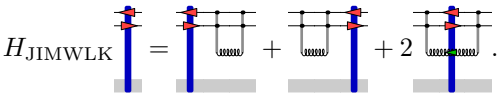

(2.45)

The factor of 2 in the last term is a symmetry factor that arises because the two contributions from expression 2.44 are indistinguishable on a diagrammatic level.

Of course, the reasoning used here to interpret the action of H_{JIMWLK} on a dipole can be used on any correlator. Each time the Hamiltonian acts on a correlator, it adds one gluon to it. This hierarchical procedure is shown schematically in Figure 2.8. Another feature visualised in this figure is the longitudinal growth of the dipole with increasing energy. As the distance between the photon-gluon vertex and the target grows, the phase space that accommodates multiple gluon emission increases. Therefore, it is more likely that gluons will be emitted at higher energies.

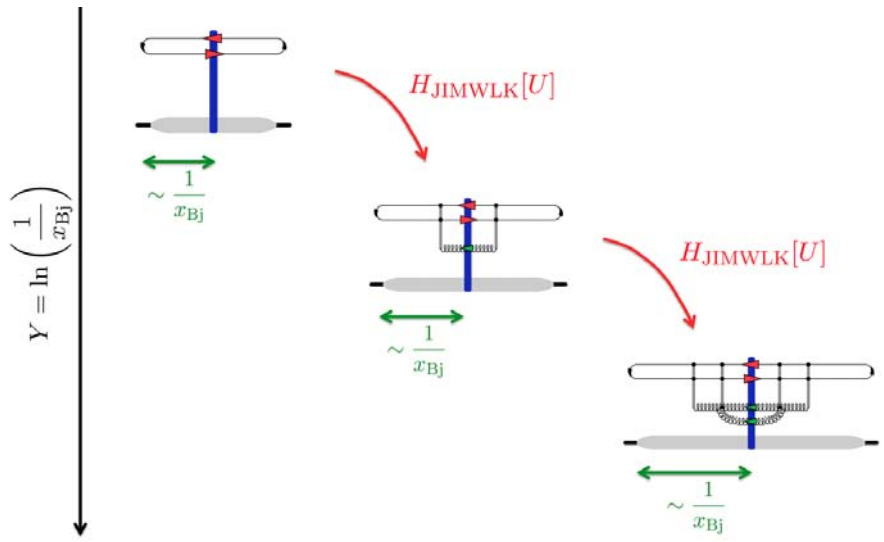

Figure 2.8: Evolution of a dipole correlator with decreasing x_{Bj} at leading order. H_{JIMWLK} adds a gluon each time it acts. The phase space for gluon emissions increases with increasing energy.

2.3.3 Perturbative treatment of the JIMWLK Hamiltonian

The energy dependence of $\hat{Z}_Y$ can be deduced perturbatively up to some accuracy, but for exact calculations at some specified Y_0, non-perturbative input from experimental data is required. The perturbative treatment begins with identifying

$$\hat{Z}_Y\big[U\big] = e^{-H\Delta Y}\hat{Z}_{Y_0}\big[U\big], \qquad \Delta Y = Y - Y_0 \tag{2.46}$$

as a solution to Equation 2.31 (the subscript on the Hamiltonian has been dropped for compactness). Diagrammatically, this solution leads to considering the sequential insertion of gluon lines to a correlator, as shown in Figure 2.8 for the dipole correlator. In this solution, the operator $e^{-H\Delta Y}$ evolves $\hat{Z}$ from Y_0 to Y.

In order for one to investigate this solution systematically, it is mandatory to deal with each order explicitly. The exponential can be expanded in a Taylor series:

$$e^{-H\Delta Y} = \sum_{j=0}^{\infty} \frac{(-H\Delta Y)^j}{j!} \tag{2.47}$$

$$= 1 - H\Delta Y + \frac{1}{2}(H\Delta Y)^2 + \mathcal{O}(H^3). \tag{2.48}$$

The saturation regime in which JIMWLK evolution applies is valid for values of Q^2 much larger than

Λ^2_{QCD}: since the coupling α_s is inversely proportional to $\ln \frac{Q^2}{\Lambda^2_{\text{QCD}}}$, it is small and can be used as a perturbative parameter for expanding H according to

$$H = \alpha_s H^{(1)} + \alpha_s^2 H^{(2)} + \alpha_s^3 H^{(3)} + ... \tag{2.49}$$

This is a standard perturbative expansion in which terms increase with a factor of α_s. Substituting this expanded form of H into Equation 2.48 gives

$$e^{-H\Delta Y} = 1 - \Big(\alpha_s H^{(1)} + \alpha_s^2 H^{(2)}\Big)\Delta Y + \frac{1}{2}\Big(\alpha_s H^{(1)}\Delta Y + \alpha_s^2 H^{(2)}\Delta Y\Big)^2 + \mathcal{O}(\alpha_s^3) \tag{2.50}$$

$$= 1 - \big(\alpha_s \Delta Y\big)H^{(1)} + \frac{1}{2}\big(\alpha_s\Delta Y\big)^2\big(H^{(1)}\big)^2 - \alpha_s\big(\alpha_s\Delta Y\big)H^{(2)} + \mathcal{O}(\alpha_s^3) \tag{2.51}$$

and so the α_s counting has been thrown off. Notice, however, that the general form of a term in this expansion has a coefficient $\alpha_s^m(\alpha_s\Delta Y)^n$, where $m, n \in \mathbb{Z}^+$. Terms of this kind are interpreted as quantum correction factors. Factors of $(\alpha_s\Delta Y)^n$ are of order 1 because the smallness of α_s is compensated for by a large ΔY. In order to count factors of α_s, as in standard perturbation theory, additional factors of α_s must be counted over-and-above $(\alpha_s\Delta Y)^n$. It is therefore useful to order terms by m because this is the parameter that counts the number of additional α_s factors in the term.

Explicitly, the first few terms at leading order ($m = 0$) are

$$n = 0: \qquad 1 \tag{2.52}$$

$$n = 1: \qquad -\big(\alpha_s\Delta Y\big)H^{(1)} \tag{2.53}$$

$$n = 2: \qquad +\frac{1}{2}\big(\alpha_s\Delta Y\big)^2\big(H^{(1)}\big)^2 \tag{2.54}$$

and consist of all diagrams with iterated one-gluon emission (as in diagrams of the type shown in Equation 2.45). An example of a leading order contribution is the second diagram in Figure 2.8. The first few next-to-leading order ($m = 1$) terms are

$$n = 1: \qquad -\alpha_s\big(\alpha_s\Delta Y\big)H^{(2)} \tag{2.55}$$

$$n = 2: \qquad +\frac{1}{2}\alpha_s\big(\alpha_s\Delta Y\big)^2\Big\{H^{(1)}, H^{(2)}\Big\} \tag{2.56}$$

where $\{A, B\} := AB + BA$ is the anti-commutator. These correspond to diagrams with two gluons, as can be seen in the last diagram of Figure 2.8. The leading order Hamiltonian, $H^{(1)}$, has already been provided in Equation 2.38. The forms of $H^{(2)}$, $H^{(3)}$, etc. on the other hand, are unknown. One might be concerned that higher order contributions are non-negligible. The expansion only serves the purpose of making individual terms in the exponential solution $e^{-H\Delta Y}$ explicit. Once these terms

have been evaluated order-by-order, all contributions must be resummed by re-exponentiation so that higher-order terms are not neglected. Explicit expressions for leading order JIMWLK exist in the literature, along with running coupling corrections [58]. The next-to-leading order is far more involved but some work has been attempted in [59] and similar papers.

Chapter 3

The Gaussian Truncation

The JIMWLK equation is an open equation in the sense that n^{th}-order calculations need input from the $n+1^{\text{st}}$ order. The equation can, however, be written in an equivalent form, called the *Balitsky hierarchy* [60,61] - a hierarchy of coupled equations for n-point correlators. The equation for the 2-point correlator is

$$\frac{d}{dY}\left\langle \frac{\mathrm{tr}(U_{\boldsymbol{x}}U_{\boldsymbol{y}}^\dagger)}{N_c}\right\rangle_Y = \frac{\alpha_s}{\pi^2}\int d^2z\,\tilde{\mathcal{K}}_{\boldsymbol{xzy}}\left(\left\langle \frac{\tilde{U}_{\boldsymbol{z}}^{ab}\,\mathrm{tr}(t^aU_{\boldsymbol{x}}t^bU_{\boldsymbol{y}}^\dagger)}{N_c}\right\rangle_Y - C_f\left\langle \frac{\mathrm{tr}(U_{\boldsymbol{x}}U_{\boldsymbol{y}}^\dagger)}{N_c}\right\rangle_Y\right) \tag{3.1}$$

where $C_f = \frac{N_c^2-1}{2N_c}$ (f denotes the fundamental representation)*. This can be derived easily from the JIMWLK equation, as will be shown in Section 3.1. Notice that this equation requires the 3-point correlator, $\left\langle \tilde{U}_{\boldsymbol{z}}^{ab}\,\mathrm{tr}(t^aU_{\boldsymbol{x}}t^bU_{\boldsymbol{y}}^\dagger)\right\rangle_Y$, as input. In fact, at every order n in the hierarchy, knowledge of the $n+1^{\text{st}}$ is required. In order to do practical calculations then, some kind of approximation or truncation is needed.

One such technique is to use the mean-field approximation to write a closed, non-linear equation for the 2-point correlator, called the *BK equation* (Balitsky-Kovchegov equation) [62–64]. This can be

*For any representation $\mathcal{R}$, one can write $\mathrm{tr}(t^a_{\mathcal{R}}t^b_{\mathcal{R}})_{\mathcal{R}} = \alpha_{\mathcal{R}}\delta^{ab}$. On the other hand, the Casimir of a representation is defined as $C_{\mathcal{R}}d_{\mathcal{R}} := \mathrm{tr}(t^a_{\mathcal{R}}t^a_{\mathcal{R}})_{\mathcal{R}}$. Together, the two expressions imply $\alpha_{\mathcal{R}}d_A = C_{\mathcal{R}}d_{\mathcal{R}}$. By convention $\alpha_f = \frac{1}{2}$ and $\alpha_A = N_c$. Then C_f and C_A can be deduced easily.

obtained from Equation 3.1 by using the *Fierz identity*

$$2\tilde{U}^{ab}_{\boldsymbol{z}}\mathrm{tr}(t^a U_{\boldsymbol{x}} t^b U^\dagger_{\boldsymbol{y}}) = \mathrm{tr}(U_{\boldsymbol{x}}U^\dagger_{\boldsymbol{z}})\mathrm{tr}(U_{\boldsymbol{z}}U^\dagger_{\boldsymbol{y}}) - \frac{1}{N_c}\mathrm{tr}(U_{\boldsymbol{x}}U^\dagger_{\boldsymbol{y}}) \tag{3.2}$$

to factorise the 3-point correlator in Equation 3.1. Doing so, one obtains

$$\begin{aligned}\frac{d}{dY}\left\langle \frac{\mathrm{tr}(U_{\boldsymbol{x}}U^\dagger_{\boldsymbol{y}})}{N_c}\right\rangle_Y &= \frac{\alpha_s}{\pi^2}\int d^2z\,\tilde{\mathcal{K}}_{\boldsymbol{xzy}}\left(\left\langle \frac{\mathrm{tr}(U_{\boldsymbol{x}}U^\dagger_{\boldsymbol{z}})\mathrm{tr}(U_{\boldsymbol{z}}U^\dagger_{\boldsymbol{y}})}{2N_c} - \frac{\mathrm{tr}(U_{\boldsymbol{x}}U^\dagger_{\boldsymbol{y}})}{2N_c^2}\right\rangle_Y - C_f\left\langle \frac{\mathrm{tr}(U_{\boldsymbol{x}}U^\dagger_{\boldsymbol{y}})}{N_c}\right\rangle_Y\right)\\ &= \frac{\alpha_s N_c}{2\pi^2}\int d^2z\,\tilde{\mathcal{K}}_{\boldsymbol{xzy}}\left(\left\langle \frac{\mathrm{tr}(U_{\boldsymbol{x}}U^\dagger_{\boldsymbol{z}})}{N_c}\frac{\mathrm{tr}(U_{\boldsymbol{z}}U^\dagger_{\boldsymbol{y}})}{N_c}\right\rangle_Y - \left\langle \frac{\mathrm{tr}(U_{\boldsymbol{x}}U^\dagger_{\boldsymbol{y}})}{N_c}\right\rangle_Y\right).\end{aligned} \tag{3.3}$$

The last line is the BK equation.

The BK equation and the JIMWLK equation make similar predictions for the dipole correlator. However, the object that is actually of interest is the 4-point correlator

$$\left\langle \frac{\mathrm{tr}(U_{\boldsymbol{y}'}U^\dagger_{\boldsymbol{x}'})}{N_c}\,\frac{\mathrm{tr}(U_{\boldsymbol{x}}U^\dagger_{\boldsymbol{y}})}{N_c}\right\rangle_Y, \tag{3.4}$$

since this is what appears in experimental observables like the cross-section for exclusive vector-meson production. Investigations concerning this correlator lead to better understanding of unexplored features of JIMWLK, which have yet been probed by global observables like the total cross-section in which they do not appear.

Despite its usefulness, the BK approximation is not the correct tool in this context because it is impartial to this object (this kind of 4-point correlator does not show up in Equation 3.3). A more appropriate approximation scheme is therefore required to be able to make practical calculations using JIMWLK evolution but simultaneously stay sensitive to expression 3.4. This is called the *Gaussian Truncation** (GT) - a powerful approximation that can be used to study features beyond the scope of the BK equation. One crucial advantage of the GT is that it automatically satisfies group-theoretical constraints in the local limits of transverse coordinates in the correlators.† This will be shown explicitly in Section 3.1.4.

*The name comes from the fact that this prescription is equivalent to using a non-local Gaussian approximation for JIMWLK weights,

$$W_Y\big[\rho\big] = \exp\Big\{-\int^Y dY'\int d^2u\,d^2v\,\frac{\rho_c(Y',\boldsymbol{u})\rho_c(Y',\boldsymbol{v})}{2\mu^2(Y',\boldsymbol{u},\boldsymbol{v})}\Big\},$$

where ρ_c is a colour source with variance μ^2 and $W_Y\big[\rho\big]$ is a weight equivalent to $\hat{Z}_Y\big[U\big]$ [2].

†Generically, when one truncates an infinite hierarchy, there must be certain constraints imposed to ensure that the approximation used is legitimate. For the Schwinger-Dyson equations, for example, the Ward identities must be satisfied when the hierarchy is truncated at the n^{th} order. The group-theoretical constraints in the coincidence limits are the appropriate analogue to the Ward identities in this context.

The crux of the GT begins with a parametrisation of $F[U]$ (any Wilson line correlator average as in Equation 2.23):

$$\Big\langle F[U]\Big\rangle_Y = \exp\Big\{-\frac{1}{2}\int^Y dY' \int d^2u\, d^2v\, G_{Y',\boldsymbol{uv}}\, i\bar{\nabla}^a_{\boldsymbol{u}} i\bar{\nabla}^a_{\boldsymbol{v}}\Big\} F[U]. \tag{3.5}$$

where $G_{Y',\boldsymbol{uv}}$ is a two-point function that the correlators in Equation 3.5 can be written in terms of. The new expressions for the correlators are obtained via *parametrisation equations*. These parametrised correlators are then inserted into Equation 3.1 to obtain the Y-dependence of G. For the sake of calculating these correlators, it is convenient to note that the Y-derivative of Equation 3.5 is

$$\frac{d}{dY}\Big\langle F[U]\Big\rangle_Y = -\frac{1}{2}\Big\langle \int d^2u\, d^2v\, G_{Y,\boldsymbol{uv}}\, i\bar{\nabla}^a_{\boldsymbol{u}} i\bar{\nabla}^a_{\boldsymbol{v}}\, F[U]\Big\rangle \tag{3.6}$$

or diagrammatically for the dipole correlator,

$\frac{d}{dY}$  $=$ 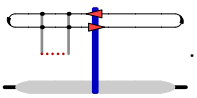 . (3.7)

It is easy to confuse this diagram on the righthand side with a gluon diagram but these are NOT the same:

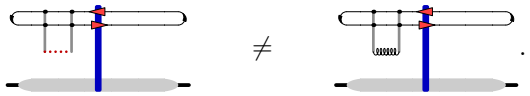

The diagram on the lefthand side is simply a visual tool that can be used to deal with calculations in the approximation scheme, defined according to Equation 3.5.

In the limit $N_c \to \infty$ (*large N_c limit*), the GT becomes the BK equation. Later on, it will become evident that correlators consisting of two dipoles are necessary to determine cross-sections of vector-meson production. These calculations grow complicated quickly so the GT will be introduced with a single-dipole correlator to begin with. Section 3.1 begins with a derivation of the Balitsky equation from the JIMWLK equation and then a detailed calculation of the relevant correlators in the GT. Every calculational detail has been included so that liberty may be taken to skip these when more complicated correlators are discussed in Section 3.2 and the next chapter. The results and explanations contained in Section 3.2 come from [2].

3.1 The Balitsky Equation for the 2-point Correlator

The basis for determining evolution equations for the degrees of freedom in the GT, namely G, is the Balitsky equation. The G content enters this equation via parametrisation equations obtained from applying the GT to the 2-point and 3-point correlators that enter Equation 3.1. These G-parametrised expressions for the correlators will be calculated within the GT once the connection between the JIMWLK and Balitsky equations has been shown.

3.1.1 Relating the JIMWLK and Balitsky equations

Given the JIMWLK equation as presented in the form of Equation 2.38, Equation 3.1 can be deduced fairly painlessly. JIMWLK evolution of the dipole correlator, in particular, is

$$\frac{d}{dY}\left\langle \frac{\mathrm{tr}(U_{\boldsymbol{x}}U_{\boldsymbol{y}}^\dagger)}{N_c}\right\rangle_Y = \frac{\alpha_s}{2\pi^2}\left\langle \int d^2z\,\mathcal{K}_{\boldsymbol{uzv}}\Big[i\nabla^a_{\boldsymbol{u}}i\nabla^a_{\boldsymbol{v}} + i\bar\nabla^a_{\boldsymbol{u}}i\bar\nabla^a_{\boldsymbol{v}} + \tilde U^{ab}_{\boldsymbol{z}}(i\nabla^a_{\boldsymbol{u}}i\bar\nabla^b_{\boldsymbol{v}} + i\bar\nabla^a_{\boldsymbol{u}}i\nabla^b_{\boldsymbol{v}})\Big]\frac{\mathrm{tr}(U_{\boldsymbol{x}}U_{\boldsymbol{y}}^\dagger)}{N_c}\right\rangle_Y, \tag{3.8}$$

which can be evaluated term-by-term using Equations 2.41 and 2.42. The first term becomes

$$\begin{aligned}
&\int d^2z\,\mathcal{K}_{\boldsymbol{uzv}}i\nabla^a_{\boldsymbol{u}}i\nabla^a_{\boldsymbol{v}}\frac{\mathrm{tr}(U_{\boldsymbol{x}}U_{\boldsymbol{y}}^\dagger)}{N_c}\\
&= \int d^2z\,\mathcal{K}_{\boldsymbol{uzv}}i\nabla^a_{\boldsymbol{u}}\Big[-\frac{\mathrm{tr}(U_{\boldsymbol{x}}t^aU_{\boldsymbol{y}}^\dagger)}{N_c}\delta_{\boldsymbol{vx}} + \frac{\mathrm{tr}(U_{\boldsymbol{x}}t^aU_{\boldsymbol{y}}^\dagger)}{N_c}\delta_{\boldsymbol{vy}}\Big]\\
&= \int d^2z\,\mathcal{K}_{\boldsymbol{uzv}}\Big[\frac{\mathrm{tr}(U_{\boldsymbol{x}}t^at^aU_{\boldsymbol{y}}^\dagger)}{N_c}\delta_{\boldsymbol{vx}}\delta_{\boldsymbol{ux}} - \frac{\mathrm{tr}(U_{\boldsymbol{x}}t^at^aU_{\boldsymbol{y}}^\dagger)}{N_c}\delta_{\boldsymbol{vx}}\delta_{\boldsymbol{uy}} - \frac{\mathrm{tr}(U_{\boldsymbol{x}}t^at^aU_{\boldsymbol{y}}^\dagger)}{N_c}\delta_{\boldsymbol{vy}}\delta_{\boldsymbol{ux}} + \frac{\mathrm{tr}(U_{\boldsymbol{x}}t^at^aU_{\boldsymbol{y}}^\dagger)}{N_c}\delta_{\boldsymbol{vy}}\delta_{\boldsymbol{uy}}\Big]\\
&= \int d^2z\,\mathcal{K}_{\boldsymbol{uzv}}\frac{\mathrm{tr}(U_{\boldsymbol{x}}t^at^aU_{\boldsymbol{y}}^\dagger)}{N_c}\Big[\delta_{\boldsymbol{vx}}\delta_{\boldsymbol{ux}} - \delta_{\boldsymbol{vx}}\delta_{\boldsymbol{uy}} - \delta_{\boldsymbol{vy}}\delta_{\boldsymbol{ux}} + \delta_{\boldsymbol{vy}}\delta_{\boldsymbol{uy}}\Big]\\
&= C_f\int d^2z\,\mathcal{K}_{\boldsymbol{uzv}}\frac{\mathrm{tr}(U_{\boldsymbol{x}}U_{\boldsymbol{y}}^\dagger)}{N_c}\Big[\delta_{\boldsymbol{vx}}\delta_{\boldsymbol{ux}} - \delta_{\boldsymbol{vx}}\delta_{\boldsymbol{uy}} - \delta_{\boldsymbol{vy}}\delta_{\boldsymbol{ux}} + \delta_{\boldsymbol{vy}}\delta_{\boldsymbol{uy}}\Big]\\
&= C_f\int d^2z\,\Big[\mathcal{K}_{\boldsymbol{xzx}} - \mathcal{K}_{\boldsymbol{yzx}} - \mathcal{K}_{\boldsymbol{xzy}} + \mathcal{K}_{\boldsymbol{yzy}}\Big]\frac{\mathrm{tr}(U_{\boldsymbol{x}}U_{\boldsymbol{y}}^\dagger)}{N_c}\\
&= -C_f\int d^2z\,\Big[-\mathcal{K}_{\boldsymbol{xzx}} + 2\mathcal{K}_{\boldsymbol{xzy}} - \mathcal{K}_{\boldsymbol{yzy}}\Big]\frac{\mathrm{tr}(U_{\boldsymbol{x}}U_{\boldsymbol{y}}^\dagger)}{N_c}\\
&= -C_f\int d^2z\,\tilde{\mathcal{K}}_{\boldsymbol{xzy}}\frac{\mathrm{tr}(U_{\boldsymbol{x}}U_{\boldsymbol{y}}^\dagger)}{N_c}
\end{aligned} \tag{3.9}$$

where, in the last line, the linear combination

$$\tilde{\mathcal{K}}_{\boldsymbol{xzy}} := -\mathcal{K}_{\boldsymbol{xzx}} + 2\mathcal{K}_{\boldsymbol{xzy}} - \mathcal{K}_{\boldsymbol{yzy}} \tag{3.10}$$

has been renamed. Similarly, the second term of Equation 3.8 becomes

$$\int d^2z\, \mathcal{K}_{\boldsymbol{uzv}} i\bar{\nabla}^a_{\boldsymbol{u}} i\bar{\nabla}^a_{\boldsymbol{v}} \frac{\mathrm{tr}(U_{\boldsymbol{x}}U^\dagger_{\boldsymbol{y}})}{N_c} = -C_f \int d^2z\, \tilde{\mathcal{K}}_{\boldsymbol{xzy}} \frac{\mathrm{tr}(U_{\boldsymbol{x}}U^\dagger_{\boldsymbol{y}})}{N_c}. \tag{3.11}$$

The last terms of Equation 3.8 are

$$\begin{aligned}
&\mathcal{K}_{\boldsymbol{uzv}} \tilde{U}^{ab}_{\boldsymbol{z}} i\nabla^a_{\boldsymbol{u}} i\bar{\nabla}^b_{\boldsymbol{v}} \frac{\mathrm{tr}(U_{\boldsymbol{x}}U^\dagger_{\boldsymbol{y}})}{N_c} \\
&= \int d^2z\, \mathcal{K}_{\boldsymbol{uzv}} \tilde{U}^{ab}_{\boldsymbol{z}} i\bar{\nabla}^b_{\boldsymbol{v}} \Big[\frac{\mathrm{tr}(t^a U_{\boldsymbol{x}}U^\dagger_{\boldsymbol{y}})}{N_c} \delta_{\boldsymbol{ux}} - \frac{\mathrm{tr}(U_{\boldsymbol{x}}U^\dagger_{\boldsymbol{y}}t^a)}{N_c} \delta_{\boldsymbol{uy}} \Big] \\
&= \int d^2z\, \mathcal{K}_{\boldsymbol{uzv}} \tilde{U}^{ab}_{\boldsymbol{z}} \Big[- \frac{\mathrm{tr}(t^a U_{\boldsymbol{x}}t^b U^\dagger_{\boldsymbol{y}})}{N_c} \delta_{\boldsymbol{ux}}\delta_{\boldsymbol{vx}} + \frac{\mathrm{tr}(t^a U_{\boldsymbol{x}}t^b U^\dagger_{\boldsymbol{y}})}{N_c} \delta_{\boldsymbol{ux}}\delta_{\boldsymbol{vy}} + \frac{\mathrm{tr}(U_{\boldsymbol{x}}t^b U^\dagger_{\boldsymbol{y}}t^a)}{N_c} \delta_{\boldsymbol{uy}}\delta_{\boldsymbol{vx}} - \frac{\mathrm{tr}(U_{\boldsymbol{x}}t^b U^\dagger_{\boldsymbol{y}}t^a)}{N_c} \delta_{\boldsymbol{uy}}\delta_{\boldsymbol{vy}} \Big] \\
&= \int d^2z\, \mathcal{K}_{\boldsymbol{uzv}} \tilde{U}^{ab}_{\boldsymbol{z}} \frac{\mathrm{tr}(t^a U_{\boldsymbol{x}}t^b U^\dagger_{\boldsymbol{y}})}{N_c} \Big[- \delta_{\boldsymbol{ux}}\delta_{\boldsymbol{vx}} + \delta_{\boldsymbol{ux}}\delta_{\boldsymbol{vy}} + \delta_{\boldsymbol{uy}}\delta_{\boldsymbol{vx}} - \delta_{\boldsymbol{uy}}\delta_{\boldsymbol{vy}} \Big] \\
&= \int d^2z \Big[- \mathcal{K}_{\boldsymbol{xzx}} + \mathcal{K}_{\boldsymbol{xzy}} + \mathcal{K}_{\boldsymbol{yzx}} - \mathcal{K}_{\boldsymbol{yzy}} \Big] \tilde{U}^{ab}_{\boldsymbol{z}} \frac{\mathrm{tr}(t^a U_{\boldsymbol{x}}t^b U^\dagger_{\boldsymbol{y}})}{N_c} \\
&= \int d^2z\, \tilde{\mathcal{K}}_{\boldsymbol{xzy}} \tilde{U}^{ab}_{\boldsymbol{z}} \frac{\mathrm{tr}(t^a U_{\boldsymbol{x}}t^b U^\dagger_{\boldsymbol{y}})}{N_c} \\
&= \int d^2z\, \mathcal{K}_{\boldsymbol{uzv}} \tilde{U}^{ab}_{\boldsymbol{z}} i\bar{\nabla}^a_{\boldsymbol{u}} i\nabla^b_{\boldsymbol{v}} \frac{\mathrm{tr}(U_{\boldsymbol{x}}U^\dagger_{\boldsymbol{y}})}{N_c}.
\end{aligned} \tag{3.12}$$

Plugging these results into Equation 3.8 yields

$$\frac{d}{dY} \Big\langle \frac{\mathrm{tr}(U_{\boldsymbol{x}}U^\dagger_{\boldsymbol{y}})}{N_c} \Big\rangle_Y = \frac{\alpha_s}{\pi^2} \int d^2z\, \tilde{\mathcal{K}}_{\boldsymbol{xzy}} \Big\langle - C_f \frac{\mathrm{tr}(U_{\boldsymbol{x}}U^\dagger_{\boldsymbol{y}})}{N_c} + \frac{\tilde{U}^{ab}_{\boldsymbol{z}} \mathrm{tr}(t^a U_{\boldsymbol{x}}t^b U^\dagger_{\boldsymbol{y}})}{N_c} \Big\rangle_Y, \tag{3.13}$$

which is the same as the Balitsky equation as claimed in the chapter introduction.

3.1.2 Parametrisation equation for the 2-point correlator

Given the Balitsky equation, all that is left to do is to find expressions for the the correlators contained in it. In the case $F[U] = \Big\langle \mathrm{tr}(U_{\boldsymbol{x}}U^\dagger_{\boldsymbol{y}}) \Big\rangle_Y$, one obtains from Equation 3.6:

$$\frac{d}{dY} \Big\langle \mathrm{tr}(U_{\boldsymbol{x}}U^\dagger_{\boldsymbol{y}}) \Big\rangle_Y = -\frac{1}{2} \Big\langle \int d^2u\, d^2v\, G_{Y,\boldsymbol{uv}}\, i\bar{\nabla}^a_{\boldsymbol{u}} i\bar{\nabla}^a_{\boldsymbol{v}}\, \mathrm{tr}(U_{\boldsymbol{x}}U^\dagger_{\boldsymbol{y}}) \Big\rangle \tag{3.14}$$

or diagrammatically,

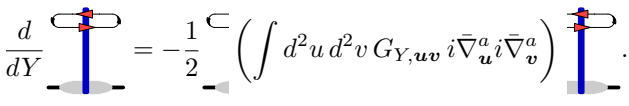

(3.15)

Then using expressions 2.41 and 2.42,

$$\begin{aligned}
&\int d^2u\, d^2v\, G_{Y,\boldsymbol{uv}}\, i\bar{\nabla}^a_{\boldsymbol{u}} i\bar{\nabla}^a_{\boldsymbol{v}} \operatorname{tr}(U_{\boldsymbol{x}}U^\dagger_{\boldsymbol{y}}) \\
&= \int d^2u\, d^2v\, G_{Y,\boldsymbol{uv}}\, i\bar{\nabla}^a_{\boldsymbol{u}} \Big[\operatorname{tr}(t^a U_{\boldsymbol{x}}U^\dagger_{\boldsymbol{y}})\delta_{\boldsymbol{vx}} - \operatorname{tr}(U_{\boldsymbol{x}}U^\dagger_{\boldsymbol{y}}t^a)\delta_{\boldsymbol{vy}}\Big] \\
&= \int d^2u\, d^2v\, G_{Y,\boldsymbol{uv}} \Big[\operatorname{tr}(t^a t^a U_{\boldsymbol{x}}U^\dagger_{\boldsymbol{y}})\delta_{\boldsymbol{vx}}\delta_{\boldsymbol{uv}} - \operatorname{tr}(t^a U_{\boldsymbol{x}}U^\dagger_{\boldsymbol{y}}t^a)\delta_{\boldsymbol{vx}}\delta_{\boldsymbol{uy}} - \operatorname{tr}(t^a U_{\boldsymbol{x}}U^\dagger_{\boldsymbol{y}}t^a)\delta_{\boldsymbol{vy}}\delta_{\boldsymbol{ux}} \\
&\qquad\qquad + \operatorname{tr}(U_{\boldsymbol{x}}U^\dagger_{\boldsymbol{y}}t^a t^a)\delta_{\boldsymbol{vy}}\delta_{\boldsymbol{uv}}\Big] \\
&= G_{Y,\boldsymbol{xx}} \operatorname{tr}(t^a t^a U_{\boldsymbol{x}}U^\dagger_{\boldsymbol{y}}) - G_{Y,\boldsymbol{yx}} \operatorname{tr}(t^a U_{\boldsymbol{x}}U^\dagger_{\boldsymbol{y}}t^a) - G_{Y,\boldsymbol{xy}} \operatorname{tr}(t^a U_{\boldsymbol{x}}U^\dagger_{\boldsymbol{y}}t^a) + G_{Y,\boldsymbol{yy}} \operatorname{tr}(U_{\boldsymbol{x}}U^\dagger_{\boldsymbol{y}}t^a t^a) \\
&= G_{Y,\boldsymbol{xx}} \operatorname{tr}(t^a t^a U_{\boldsymbol{x}}U^\dagger_{\boldsymbol{y}}) - 2G_{Y,\boldsymbol{xy}} \operatorname{tr}(t^a t^a U_{\boldsymbol{x}}U^\dagger_{\boldsymbol{y}}) + G_{Y,\boldsymbol{yy}} \operatorname{tr}(t^a t^a U_{\boldsymbol{x}}U^\dagger_{\boldsymbol{y}})
\end{aligned} \tag{3.16}$$

where in the last line, $G_{Y,\boldsymbol{xy}} = G_{Y,\boldsymbol{yx}}$ and the cyclicity of the trace has been used. Renaming the linear combination

$$\mathcal{G}_{Y,\boldsymbol{xy}} := \int^Y dY' \left(G_{Y',\boldsymbol{xy}} - \frac{1}{2}\Big(G_{Y',\boldsymbol{xx}} + G_{Y',\boldsymbol{yy}}\Big)\right), \tag{3.17}$$

one can rewrite this result in terms of its derivative $\mathcal{G}'_{Y,\boldsymbol{xy}} := \frac{d}{dY}\mathcal{G}_{Y,\boldsymbol{xy}}$ as

$$\int d^2u\, d^2v\, G_{Y,\boldsymbol{uv}}\, i\bar{\nabla}^a_{\boldsymbol{u}} i\bar{\nabla}^a_{\boldsymbol{v}} \operatorname{tr}(U_{\boldsymbol{x}}U^\dagger_{\boldsymbol{y}}) = 2\,\mathcal{G}'_{Y,\boldsymbol{xy}} \operatorname{tr}(t^a t^a U_{\boldsymbol{x}}U^\dagger_{\boldsymbol{y}}). \tag{3.18}$$

Then substitution into Equation 3.14 gives

$$\begin{aligned}
\frac{d}{dY}\Big\langle \operatorname{tr}(U_{\boldsymbol{x}}U^\dagger_{\boldsymbol{y}})\Big\rangle_Y &= -\mathcal{G}'_{Y,\boldsymbol{xy}}\Big\langle \operatorname{tr}(t^a t^a U_{\boldsymbol{x}}U^\dagger_{\boldsymbol{y}})\Big\rangle_Y \\
&= -C_f\mathcal{G}'_{Y,\boldsymbol{xy}}\Big\langle \operatorname{tr}(U_{\boldsymbol{x}}U^\dagger_{\boldsymbol{y}})\Big\rangle_Y.
\end{aligned} \tag{3.19}$$

This differential equation has a simple exponential solution

$$\Big\langle \operatorname{tr}(U_{\boldsymbol{x}}U^\dagger_{\boldsymbol{y}})\Big\rangle_Y = d_f \exp\Big\{ - C_f\mathcal{G}_{Y,\boldsymbol{xy}}\Big\} \tag{3.20}$$

with normalisation factor $d_f = N_c$ (the dimension of the fundamental representation, which comes from normalising the dipole). The calculation can also be applied as is, in the adjoint representation with factor $C_A\delta_{cd} = f^{abc}f^{abd} = N_c$ and dimension $d_A = N_c^2 - 1$.

3.1.3 Parametrisation equation for the 3-point correlator

In the case $F[U] = \left\langle \tilde{U}^{ab}_{\boldsymbol{z}} \operatorname{tr}(t^a U_{\boldsymbol{x}} t^b U^\dagger_{\boldsymbol{y}}) \right\rangle_Y$, a similar procedure can be carried out to obtain an expression in terms of G. Again, using Equation 3.6,

$$\frac{d}{dY}\left\langle \tilde{U}^{ab}_{\boldsymbol{z}} \operatorname{tr}(t^a U_{\boldsymbol{x}} t^b U^\dagger_{\boldsymbol{y}}) \right\rangle_Y = -\frac{1}{2}\left\langle \int d^2u\, d^2v\, G_{Y,\boldsymbol{uv}}\, i\bar{\nabla}^c_{\boldsymbol{u}} i\bar{\nabla}^c_{\boldsymbol{v}} \left(\tilde{U}^{ab}_{\boldsymbol{z}} \operatorname{tr}(t^a U_{\boldsymbol{x}} t^b U^\dagger_{\boldsymbol{y}}) \right) \right\rangle \tag{3.21}$$

or diagrammatically,

$\frac{d}{dY}$ 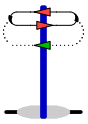 $= -\frac{1}{2}$ 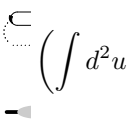 $\left(\int d^2u\, d^2v\, G_{Y,\boldsymbol{uv}}\, i\bar{\nabla}^a_{\boldsymbol{u}} i\bar{\nabla}^a_{\boldsymbol{v}} \right)$  . (3.22)

The differential operator can be executed in parts as follows:

$$\begin{aligned}
&\int d^2u\, d^2v\, G_{Y,\boldsymbol{uv}}\, i\bar{\nabla}^c_{\boldsymbol{u}} i\bar{\nabla}^c_{\boldsymbol{v}} \left(\tilde{U}^{ab}_{\boldsymbol{z}} \operatorname{tr}(t^a U_{\boldsymbol{x}} t^b U^\dagger_{\boldsymbol{y}}) \right) \\
&= \int d^2u\, d^2v\, G_{Y,\boldsymbol{uv}} \Big[\left(i\bar{\nabla}^c_{\boldsymbol{u}} i\bar{\nabla}^c_{\boldsymbol{v}} \tilde{U}^{ab}_{\boldsymbol{z}} \right) \operatorname{tr}(t^a U_{\boldsymbol{x}} t^b U^\dagger_{\boldsymbol{y}}) + \left(i\bar{\nabla}^c_{\boldsymbol{v}} \tilde{U}^{ab}_{\boldsymbol{z}} \right) \left(i\bar{\nabla}^c_{\boldsymbol{u}} \operatorname{tr}(t^a U_{\boldsymbol{x}} t^b U^\dagger_{\boldsymbol{y}}) \right) \\
&\qquad + \left(i\bar{\nabla}^c_{\boldsymbol{u}} \tilde{U}^{ab}_{\boldsymbol{z}} \right) \left(i\bar{\nabla}^c_{\boldsymbol{v}} \operatorname{tr}(t^a U_{\boldsymbol{x}} t^b U^\dagger_{\boldsymbol{y}}) \right) + \tilde{U}^{ab}_{\boldsymbol{z}} \left(i\bar{\nabla}^c_{\boldsymbol{u}} i\bar{\nabla}^c_{\boldsymbol{v}} \operatorname{tr}(t^a U_{\boldsymbol{x}} t^b U^\dagger_{\boldsymbol{y}}) \right) \Big].
\end{aligned} \tag{3.23}$$

The first three terms require the derivative of a Wilson line in the adjoint representation,

$$\begin{aligned}
i\bar{\nabla}^c_{\boldsymbol{v}} \tilde{U}^{ab}_{\boldsymbol{z}} &= i\bar{\nabla}^c_{\boldsymbol{v}} \left(2\operatorname{tr}(t^a U_{\boldsymbol{z}} t^b U^\dagger_{\boldsymbol{z}}) \right) \\
&= 2\left(\operatorname{tr}(t^a t^c U_{\boldsymbol{z}} t^b U^\dagger_{\boldsymbol{z}}) - \operatorname{tr}(t^a U_{\boldsymbol{z}} t^b U^\dagger_{\boldsymbol{z}} t^c) \right) \delta_{\boldsymbol{vz}} \\
&= 2\left(\operatorname{tr}(t^a t^c U_{\boldsymbol{z}} t^b U^\dagger_{\boldsymbol{z}}) - \operatorname{tr}(t^c t^a U_{\boldsymbol{z}} t^b U^\dagger_{\boldsymbol{z}}) \right) \delta_{\boldsymbol{vz}} \\
&= 2\left(\operatorname{tr}([t^a, t^c] U_{\boldsymbol{z}} t^b U^\dagger_{\boldsymbol{z}}) \right) \delta_{\boldsymbol{vz}} \\
&= 2if^{acd} \left(\operatorname{tr}(t^d U_{\boldsymbol{z}} t^b U^\dagger_{\boldsymbol{z}}) \right) \delta_{\boldsymbol{vz}} \\
&= if^{acd} \tilde{U}^{db}_{\boldsymbol{z}} \delta_{\boldsymbol{vz}}
\end{aligned} \tag{3.24}$$

and another derivative gives

$$\begin{aligned}
i\bar{\nabla}^c_{\boldsymbol{u}} i\bar{\nabla}^c_{\boldsymbol{v}} \tilde{U}^{ab}_{\boldsymbol{z}} &= i\bar{\nabla}^c_{\boldsymbol{u}} \Big(if^{acd} \tilde{U}^{db}_{\boldsymbol{z}} \delta_{\boldsymbol{vz}} \Big) && \text{(using Equation 3.24)} \\
&= if^{acd} \Big(i\bar{\nabla}^c_{\boldsymbol{u}} \tilde{U}^{db}_{\boldsymbol{z}} \Big) \delta_{\boldsymbol{vz}} \\
&= if^{acd} \Big(if^{dce} \tilde{U}^{eb}_{\boldsymbol{z}} \delta_{\boldsymbol{uz}} \Big) \delta_{\boldsymbol{vz}} && \text{(using Equation 3.24 again)} \\
&= -f^{acd} f^{dce} \tilde{U}^{eb}_{\boldsymbol{z}} \delta_{\boldsymbol{uz}} \delta_{\boldsymbol{vz}} \\
&= C_A \delta^{ae} \tilde{U}^{eb}_{\boldsymbol{z}} \delta_{\boldsymbol{uz}} \delta_{\boldsymbol{vz}} \\
&= C_A \tilde{U}^{ab}_{\boldsymbol{z}} \delta_{\boldsymbol{uz}} \delta_{\boldsymbol{vz}}. && (3.25)
\end{aligned}$$

Then the first term of Equation 3.23 becomes

$$\begin{aligned}
\int d^2u\, d^2v\, G_{Y,\boldsymbol{uv}} \left(i\bar{\nabla}^c_{\boldsymbol{u}} i\bar{\nabla}^c_{\boldsymbol{v}} \tilde{U}^{ab}_{\boldsymbol{z}} \right) \mathrm{tr}(t^a U_{\boldsymbol{x}} t^b U^\dagger_{\boldsymbol{y}}) &= \int d^2u\, d^2v\, G_{Y,\boldsymbol{uv}}\, C_A \tilde{U}^{ab}_{\boldsymbol{z}} \delta_{\boldsymbol{uz}} \delta_{\boldsymbol{vz}}\, \mathrm{tr}(t^a U_{\boldsymbol{x}} t^b U^\dagger_{\boldsymbol{y}}) \\
&= C_A G_{Y,\boldsymbol{zz}}\, \tilde{U}^{ab}_{\boldsymbol{z}} \mathrm{tr}(t^a U_{\boldsymbol{x}} t^b U^\dagger_{\boldsymbol{y}}). && (3.26)
\end{aligned}$$

The second term becomes

$$\begin{aligned}
&\int d^2u\, d^2v\, G_{Y,\boldsymbol{uv}} \left(i\bar{\nabla}^c_{\boldsymbol{v}} \tilde{U}^{ab}_{\boldsymbol{z}} \right) \Big(i\bar{\nabla}^c_{\boldsymbol{u}} \mathrm{tr}(t^a U_{\boldsymbol{x}} t^b U^\dagger_{\boldsymbol{y}}) \Big) \\
&= \int d^2u\, d^2v\, G_{Y,\boldsymbol{uv}} \left(if^{acd} \tilde{U}^{db}_{\boldsymbol{z}} \delta_{\boldsymbol{vz}} \right) \Big(\mathrm{tr}(t^a t^c U_{\boldsymbol{x}} t^b U^\dagger_{\boldsymbol{y}}) \delta_{\boldsymbol{ux}} - \mathrm{tr}(t^a U_{\boldsymbol{x}} t^b U^\dagger_{\boldsymbol{y}} t^c) \delta_{\boldsymbol{uy}} \Big) \\
&= if^{acd} G_{Y,\boldsymbol{xz}}\, \tilde{U}^{db}_{\boldsymbol{z}}\, \mathrm{tr}(t^a t^c U_{\boldsymbol{x}} t^b U^\dagger_{\boldsymbol{y}}) - if^{acd} G_{Y,\boldsymbol{yz}}\, \tilde{U}^{db}_{\boldsymbol{z}}\, \mathrm{tr}(t^c t^a U_{\boldsymbol{x}} t^b U^\dagger_{\boldsymbol{y}}) && (3.27)
\end{aligned}$$

which can be simplified using the relation

$$[t^a, t^b] = if^{abc} t^c = \frac{1}{2} i (2f^{abc}) t^c = \frac{1}{2} i (f^{abc} - f^{bac}) t^c.$$

Then

$$\begin{aligned}
&\int d^2u\, d^2v\, G_{Y,\boldsymbol{uv}} \left(i\bar{\nabla}^c_{\boldsymbol{v}} \tilde{U}^{ab}_{\boldsymbol{z}} \right) \Big(i\bar{\nabla}^c_{\boldsymbol{u}} \mathrm{tr}(t^a U_{\boldsymbol{x}} t^b U^\dagger_{\boldsymbol{y}}) \Big) \\
&= -\frac{1}{2} C_A \delta_{de} G_{Y,\boldsymbol{xz}}\, \tilde{U}^{db}_{\boldsymbol{z}}\, \mathrm{tr}(t^e U_{\boldsymbol{x}} t^b U^\dagger_{\boldsymbol{y}}) - \frac{1}{2} C_A \delta_{de} G_{Y,\boldsymbol{yz}}\, \tilde{U}^{db}_{\boldsymbol{z}}\, \mathrm{tr}(t^e U_{\boldsymbol{x}} t^b U^\dagger_{\boldsymbol{y}}) \\
&= -\frac{1}{2} C_A (G_{Y,\boldsymbol{xz}} + G_{Y,\boldsymbol{yz}})\, \tilde{U}^{db}_{\boldsymbol{z}}\, \mathrm{tr}(t^d U_{\boldsymbol{x}} t^b U^\dagger_{\boldsymbol{y}}) \\
&= -\frac{1}{2} C_A (G_{Y,\boldsymbol{xz}} + G_{Y,\boldsymbol{yz}})\, \tilde{U}^{ab}_{\boldsymbol{z}}\, \mathrm{tr}(t^a U_{\boldsymbol{x}} t^b U^\dagger_{\boldsymbol{y}}) && (3.28)
\end{aligned}$$

and the third term of Equation 3.23 is identical. Finally, the last term becomes

$$\begin{aligned}
&\int d^2u\, d^2v\, G_{Y,\boldsymbol{uv}}\, \tilde{U}^{ab}_{\boldsymbol{z}} \Big(i\bar{\nabla}^c_{\boldsymbol{u}} i\bar{\nabla}^c_{\boldsymbol{v}} \mathrm{tr}(t^a U_{\boldsymbol{x}} t^b U^\dagger_{\boldsymbol{y}}) \Big) \\
&= \int d^2u\, d^2v\, G_{Y,\boldsymbol{uv}}\, \tilde{U}^{ab}_{\boldsymbol{z}} \Big(\mathrm{tr}(t^a t^c t^c U_{\boldsymbol{x}} t^b U^\dagger_{\boldsymbol{y}}) \delta_{\boldsymbol{vx}} \delta_{\boldsymbol{ux}} - \mathrm{tr}(t^a t^c U_{\boldsymbol{x}} t^b U^\dagger_{\boldsymbol{y}} t^c) \delta_{\boldsymbol{vy}} \delta_{\boldsymbol{ux}} \\
&\qquad\qquad - \mathrm{tr}(t^a t^c U_{\boldsymbol{x}} t^b U^\dagger_{\boldsymbol{y}} t^c) \delta_{\boldsymbol{vx}} \delta_{\boldsymbol{uy}} + \mathrm{tr}(t^a U_{\boldsymbol{x}} t^b U^\dagger_{\boldsymbol{y}} t^c t^c) \delta_{\boldsymbol{vy}} \delta_{\boldsymbol{uy}} \Big) \\
&= G_{Y,\boldsymbol{xx}} \tilde{U}^{ab}_{\boldsymbol{z}}\, \mathrm{tr}(t^a t^c t^c U_{\boldsymbol{x}} t^b U^\dagger_{\boldsymbol{y}}) - G_{Y,\boldsymbol{xy}} \tilde{U}^{ab}_{\boldsymbol{z}}\, \mathrm{tr}(t^a t^c U_{\boldsymbol{x}} t^b U^\dagger_{\boldsymbol{y}} t^c) - G_{Y,\boldsymbol{yx}} \tilde{U}^{ab}_{\boldsymbol{z}}\, \mathrm{tr}(t^a t^c U_{\boldsymbol{x}} t^b U^\dagger_{\boldsymbol{y}} t^c) \\
&\qquad\qquad + G_{Y,\boldsymbol{yy}} \tilde{U}^{ab}_{\boldsymbol{z}}\, \mathrm{tr}(t^a U_{\boldsymbol{x}} t^b U^\dagger_{\boldsymbol{y}} t^c t^c) \\
&= C_f\, G_{Y,\boldsymbol{xx}} \tilde{U}^{ab}_{\boldsymbol{z}}\, \mathrm{tr}(t^a U_{\boldsymbol{x}} t^b U^\dagger_{\boldsymbol{y}}) - 2\, G_{Y,\boldsymbol{xy}} \tilde{U}^{ab}_{\boldsymbol{z}}\, \mathrm{tr}(t^c t^a t^c U_{\boldsymbol{x}} t^b U^\dagger_{\boldsymbol{y}}) + C_f\, G_{Y,\boldsymbol{yy}} \tilde{U}^{ab}_{\boldsymbol{z}}\, \mathrm{tr}(t^a U_{\boldsymbol{x}} t^b U^\dagger_{\boldsymbol{y}}).
\end{aligned} \tag{3.29}$$

The second term of this expression can be further simplified by noting that

$$\begin{aligned}
t^c t^a t^c &= t^a t^c t^c + [t^c, t^a] t^c \\
&= t^a C_f + i f^{cad} t^d t^c \\
&= t^a C_f + i f^{cad} \Big(\frac{1}{2} i f^{dce} t^e \Big) \\
&= t^a C_f - \frac{C_A}{2} \delta_{ae} t^e \\
&= t^a (C_f - \frac{C_A}{2}).
\end{aligned} \tag{3.30}$$

Then Equation 3.29 becomes

$$\begin{aligned}
&\int d^2u\, d^2v\, G_{Y,\boldsymbol{uv}}\, \tilde{U}^{ab}_{\boldsymbol{z}} \Big(i\bar{\nabla}^c_{\boldsymbol{u}} i\bar{\nabla}^c_{\boldsymbol{v}} \mathrm{tr}(t^a U_{\boldsymbol{x}} t^b U^\dagger_{\boldsymbol{y}}) \Big) \\
&= C_f G_{Y,\boldsymbol{xx}}\, \tilde{U}^{ab}_{\boldsymbol{z}} \mathrm{tr}(t^a U_{\boldsymbol{x}} t^b U^\dagger_{\boldsymbol{y}}) - 2(C_f - \frac{C_A}{2})\, G_{Y,\boldsymbol{xy}} \tilde{U}^{ab}_{\boldsymbol{z}}\, \mathrm{tr}(t^a U_{\boldsymbol{x}} t^b U^\dagger_{\boldsymbol{y}}) + C_f G_{Y,\boldsymbol{yy}} \tilde{U}^{ab}_{\boldsymbol{z}}\, \mathrm{tr}(t^a U_{\boldsymbol{x}} t^b U^\dagger_{\boldsymbol{y}}) \\
&= -2C_f\, \mathcal{G}'_{Y,\boldsymbol{xy}}\, \tilde{U}^{ab}_{\boldsymbol{z}} \mathrm{tr}(t^a U_{\boldsymbol{x}} t^b U^\dagger_{\boldsymbol{y}}) + C_A\, G_{Y,\boldsymbol{xy}}\, \tilde{U}^{ab}_{\boldsymbol{z}}\, \mathrm{tr}(t^a U_{\boldsymbol{x}} t^b U^\dagger_{\boldsymbol{y}})
\end{aligned} \tag{3.31}$$

Putting all the pieces of Equation 3.23 together results in

$$\begin{aligned}
&\int d^2u\, d^2v\, G_{Y,\boldsymbol{uv}}\, i\bar{\nabla}^c_{\boldsymbol{u}} i\bar{\nabla}^c_{\boldsymbol{v}} \Big(\tilde{U}^{ab}_{\boldsymbol{z}}\, \mathrm{tr}(t^a U_{\boldsymbol{x}} t^b U^\dagger_{\boldsymbol{y}}) \Big) \\
&= C_A\, G_{Y,\boldsymbol{zz}}\, \tilde{U}^{ab}_{\boldsymbol{z}} \mathrm{tr}(t^a U_{\boldsymbol{x}} t^b U^\dagger_{\boldsymbol{y}}) - C_A (G_{Y,\boldsymbol{xz}} + G_{Y,\boldsymbol{yz}})\, \tilde{U}^{ab}_{\boldsymbol{z}}\, \mathrm{tr}(t^a U_{\boldsymbol{x}} t^b U^\dagger_{\boldsymbol{y}}) - 2C_f\, \mathcal{G}'_{Y,\boldsymbol{xy}}\, \tilde{U}^{ab}_{\boldsymbol{z}} \mathrm{tr}(t^a U_{\boldsymbol{x}} t^b U^\dagger_{\boldsymbol{y}}) \\
&\qquad\qquad + C_A\, G_{Y,\boldsymbol{xy}}\, \tilde{U}^{ab}_{\boldsymbol{z}}\, \mathrm{tr}(t^a U_{\boldsymbol{x}} t^b U^\dagger_{\boldsymbol{y}}) \\
&= \Big[C_A \Big(G_{Y,\boldsymbol{zz}} - G_{Y,\boldsymbol{xz}} - G_{Y,\boldsymbol{yz}} + G_{Y,\boldsymbol{xy}} \Big) - 2C_f\, \mathcal{G}'_{Y,\boldsymbol{xy}} \Big] \tilde{U}^{ab}_{\boldsymbol{z}}\, \mathrm{tr}(t^a U_{\boldsymbol{x}} t^b U^\dagger_{\boldsymbol{y}}) \\
&= -\Big[C_A \Big(\mathcal{G}'_{Y,\boldsymbol{xz}} + \mathcal{G}'_{Y,\boldsymbol{yz}} - \mathcal{G}'_{Y,\boldsymbol{xy}} \Big) + 2C_f\, \mathcal{G}'_{Y,\boldsymbol{xy}} \Big] \tilde{U}^{ab}_{\boldsymbol{z}}\, \mathrm{tr}(t^a U_{\boldsymbol{x}} t^b U^\dagger_{\boldsymbol{y}})
\end{aligned} \tag{3.32}$$

which, at last, can be substituted into Equation 3.21 to yield

$$\frac{d}{dY} \Big\langle \tilde{U}^{ab}_{\boldsymbol{z}}\, \mathrm{tr}(t^a U_{\boldsymbol{x}} t^b U^\dagger_{\boldsymbol{y}}) \Big\rangle_Y = -\Big[\frac{C_A}{2} \Big(\mathcal{G}'_{Y,\boldsymbol{xz}} + \mathcal{G}'_{Y,\boldsymbol{yz}} - \mathcal{G}'_{Y,\boldsymbol{xy}} \Big) + C_f\, \mathcal{G}'_{Y,\boldsymbol{xy}} \Big] \Big\langle \tilde{U}^{ab}_{\boldsymbol{z}}\, \mathrm{tr}(t^a U_{\boldsymbol{x}} t^b U^\dagger_{\boldsymbol{y}}) \Big\rangle. \tag{3.33}$$

This differential equation also has an exponential solution like the 2-point correlator:

$$\left\langle \tilde{U}^{ab}_{\boldsymbol{z}} \operatorname{tr}(t^a U_{\boldsymbol{x}} t^b U^\dagger_{\boldsymbol{y}}) \right\rangle_Y = C_f d_f \exp\Big\{ -\frac{C_A}{2}\big(\mathcal{G}_{Y,\boldsymbol{xz}} + \mathcal{G}_{Y,\boldsymbol{yz}} - \mathcal{G}_{Y,\boldsymbol{xy}}\big) - C_f\, \mathcal{G}_{Y,\boldsymbol{xy}} \Big\} \tag{3.34}$$

where the normalisation factor is written as $C_f d_f$*.

3.1.4 Energy evolution of G

With Equations 3.20 and 3.34 serving as expressions for the 2-point and 3-point correlators, respectively, the Balitsky equation given in Equation 3.1 can be written as

$$\frac{d}{dY}\Big[d_f \exp\Big\{ - C_f \mathcal{G}_{Y,\boldsymbol{xy}} \Big\}\Big] = \frac{\alpha_s}{\pi^2} \int d^2 z\, \mathcal{K}_{\boldsymbol{xzy}} \Bigg(C_f d_f \exp\Big\{ -\frac{C_A}{2}\big(\mathcal{G}_{Y,\boldsymbol{xz}} + \mathcal{G}_{Y,\boldsymbol{yz}} - \mathcal{G}_{Y,\boldsymbol{xy}}\big) - C_f\, \mathcal{G}_{Y,\boldsymbol{xy}} \Big\} - C_f \Big[d_f \exp\Big\{ - C_f \mathcal{G}_{Y,\boldsymbol{xy}} \Big\}\Big] \Bigg). \tag{3.35}$$

Differentiating both sides by Y and cancelling common factors gives a more enlightening expression for the energy evolution of $\mathcal{G}$:

$$\frac{d}{dY}\mathcal{G}_{Y,\boldsymbol{xy}} = \frac{\alpha_s}{\pi^2} \int d^2 z\, \mathcal{K}_{\boldsymbol{xzy}} \Bigg(1 - \exp\Big\{ -\frac{C_A}{2}\big(\mathcal{G}_{Y,\boldsymbol{xz}} + \mathcal{G}_{Y,\boldsymbol{yz}} - \mathcal{G}_{Y,\boldsymbol{xy}}\big) \Big\} \Bigg). \tag{3.36}$$

This is the energy evolution of the Gaussian 2-point function, which was the goal of the calculation. Although the Wilson lines for the quarks were taken to be in the fundamental representation, in [65] it was shown that the GT actually gets to this result regardless of representation.

*This comes from the normalisation of $[\tilde{U}_{\boldsymbol{z}}]^{ab}\operatorname{tr}(t^a U_{\boldsymbol{x}} t^b U^\dagger_{\boldsymbol{y}})$.

Local limits

One of the advantages of the GT is that it *automatically* satisfies the group theory constraints. These can be checked by taking local limits in the transverse coordinates of the Wilson lines in the correlators, thereby doing consistency checks to make sure results are in agreement with each other. For example, taking the limit

$$\lim_{\boldsymbol{y}\to\boldsymbol{x}} \tilde{U}^{ab}_{\boldsymbol{z}} \mathrm{tr}(t^a U_{\boldsymbol{x}} t^b U^\dagger_{\boldsymbol{y}}) = C_f \frac{d_f}{d_A} \mathrm{tr}(\tilde{U}_{\boldsymbol{z}} \tilde{U}^\dagger_{\boldsymbol{x}}) \tag{3.37}$$

results in two lines in the adjoint, which it should (a quark and an antiquark line on top of each other looks like a gluon line). Other limits can also be considered,

$$\lim_{\boldsymbol{z}\to\boldsymbol{y} \text{ or } \boldsymbol{x}} \tilde{U}^{ab}_{\boldsymbol{z}} \mathrm{tr}(t^a U_{\boldsymbol{x}} t^b U^\dagger_{\boldsymbol{y}}) = C_f \mathrm{tr}(U_{\boldsymbol{x}} U^\dagger_{\boldsymbol{y}}) \tag{3.38}$$

$$\lim_{\substack{\boldsymbol{z}\to\boldsymbol{y}\\ \boldsymbol{y}\to\boldsymbol{x}}} \tilde{U}^{ab}_{\boldsymbol{z}} \mathrm{tr}(t^a U_{\boldsymbol{x}} t^b U^\dagger_{\boldsymbol{y}}) = C_f d_f. \tag{3.39}$$

Checks of this kind seem trivial when the correlators of interest are simple 2- and 3-point functions but will become useful when 4- and even 6-point functions are considered later.

3.2 The 4-point Correlator

Due to the presence of the 4-point correlator

$$\left\langle \frac{\mathrm{tr}(U_{\boldsymbol{y}'} U^\dagger_{\boldsymbol{x}'})}{N_c} \frac{\mathrm{tr}(U_{\boldsymbol{x}} U^\dagger_{\boldsymbol{y}})}{N_c} \right\rangle_Y$$

in the vector-meson production cross-section, one is led to consider a target diagram of the type 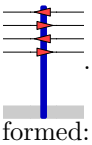 . Given two quarks and two antiquarks, there are now two nonequivalent basis states that can be formed:

(3.40)

with normalisation factors $= N_c$ and $= = \frac{d_A}{4}$ (the $\frac{1}{4}$ comes from the normalisation of generators $\mathrm{tr}(t^a t^b) = \frac{1}{2}\delta^{ab}$). An alternative choice of bases is

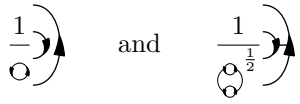

(3.41)

but this is completely equivalent to the first set. Projecting both the left and right sides of the 4-point target diagram onto the first basis state gives

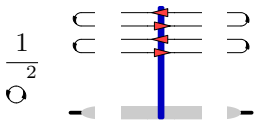

(3.42)

which is the 4-point correlator

$$\left\langle \frac{\mathrm{tr}(U_{\boldsymbol{y}'}U^\dagger_{\boldsymbol{x}'})}{N_c}\frac{\mathrm{tr}(U_{\boldsymbol{x}}U^\dagger_{\boldsymbol{y}})}{N_c}\right\rangle_Y$$

required.

In addition to the fact that the 4-point correlator appears in the vector-meson cross-section, there is another strong motivation to consider 4- and higher-point functions. Consider, for example, the 3-point correlator 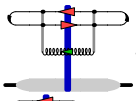 . The same mathematical expression can be obtained by considering the 4-point correlator 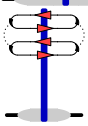 in the coincidence limit in which the bottom quark and antiquark interact with the target field at the same transverse coordinate. Then 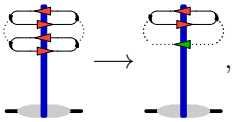 , which is the same as 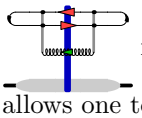 in terms of the target interaction. Studying higher-point correlators in local limits therefore allows one to study gluon lines that cross the target field without much more difficulty.

3.2.1 The correlator matrix

Since there are two basis states, there are actually four different 4-point correlators that can be formed:

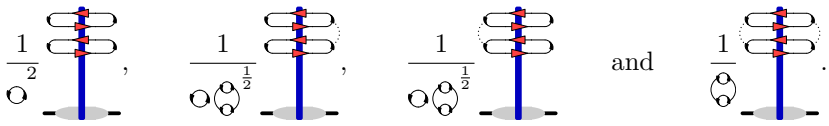

(3.43)

As a matter of convenience, one can write these four terms in a matrix

$$\mathcal{A}(Y) :=$$

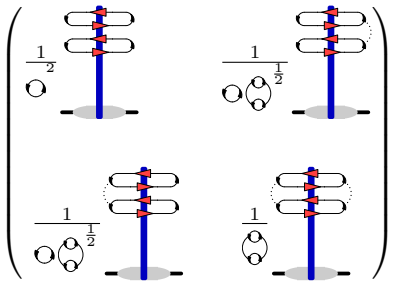

(3.44)

$$= \begin{pmatrix} \frac{\left\langle \mathrm{tr}(U_{\boldsymbol{y}'} U^\dagger_{\boldsymbol{x}'}) \mathrm{tr}(U_{\boldsymbol{x}} U^\dagger_{\boldsymbol{y}}) \right\rangle_Y}{N_c^2} & \frac{\left\langle \mathrm{tr}(U_{\boldsymbol{y}'} t^a U^\dagger_{\boldsymbol{x}'}) \mathrm{tr}(U_{\boldsymbol{x}} t^a U^\dagger_{\boldsymbol{y}}) \right\rangle_Y}{N_c \sqrt{d_A/4}} \\ \frac{\left\langle \mathrm{tr}(U_{\boldsymbol{y}'} U^\dagger_{\boldsymbol{x}'} t^b) \mathrm{tr}(U_{\boldsymbol{x}} U^\dagger_{\boldsymbol{y}} t^b) \right\rangle_Y}{N_c \sqrt{d_A/4}} & \frac{\left\langle \mathrm{tr}(U_{\boldsymbol{y}'} t^a U^\dagger_{\boldsymbol{x}'} t^b) \mathrm{tr}(U_{\boldsymbol{x}} t^a U^\dagger_{\boldsymbol{y}} t^b) \right\rangle_Y}{d_A/4} \end{pmatrix}$$

(3.45)

where the transition elements have been placed on the off-diagonals. The elements of this correlator matrix may generically mix if the off-diagonal elements are non-zero. The 2-dipole analogue of Equation 3.7 is therefore a matrix equation

$$\frac{d}{dY}\mathcal{A}(Y) = -\mathcal{M}(Y)\mathcal{A}(Y) \tag{3.46}$$

where matrix

$$\mathcal{M}(Y) := \begin{pmatrix} a_Y & c_Y \\ c_Y & b_Y \end{pmatrix} \tag{3.47}$$

has elements containing the relevant G content. To make these elements more explicit, it is beneficial to write the diagrammatic equivalent of Equation 3.46:

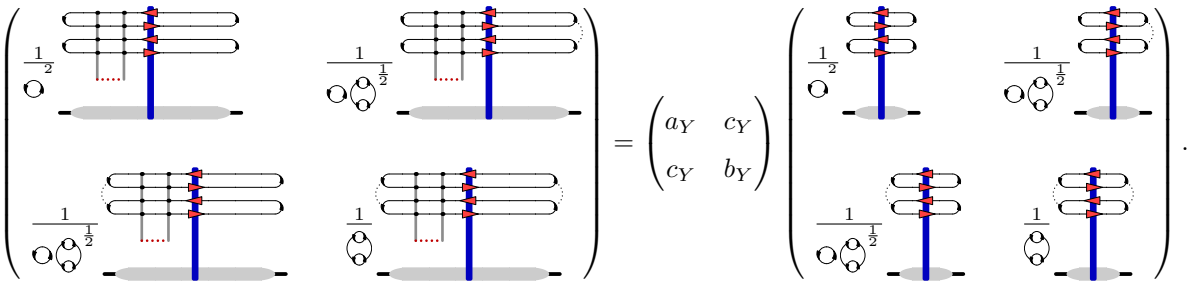

(3.48)

As an example, consider the result of matrix multiplication for the top left element of $\mathcal{A}(Y)$:

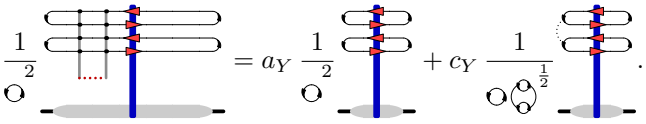

(3.49)

On the other hand, the differential operator $\int d^2u\, d^2v\, G_{\boldsymbol{uv}} i\bar{\nabla}^a_{\boldsymbol{u}} i\bar{\nabla}^a_{\boldsymbol{v}}$ (the Y subscript on G will be suppressed for clarity from here on out) acting on this element of $\mathcal{A}(Y)$ gives

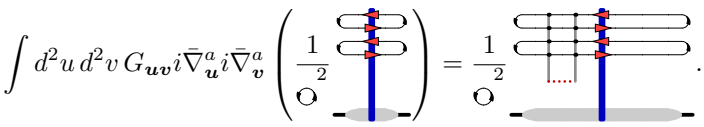

(3.50)

The G content of the righthand side can be separated from the target interaction by inserting a complete set of singlet states

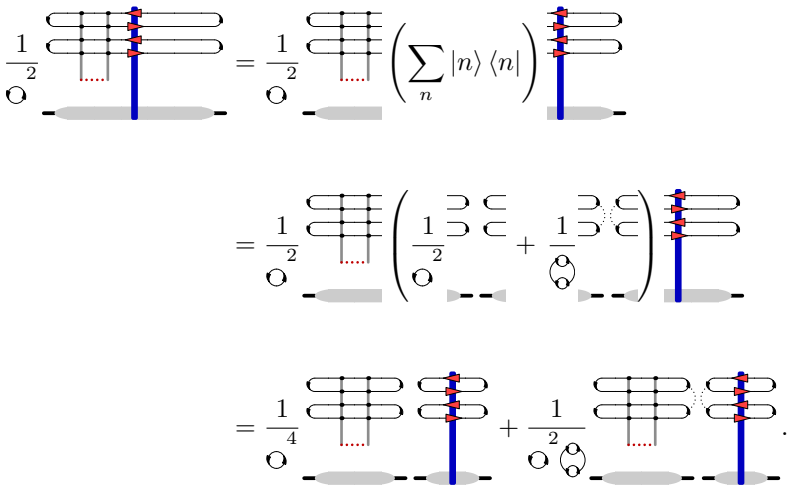

(3.51)

Direct comparison with Equation 3.49 implies

$a_Y = -$ 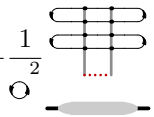 and $c_Y = -$ 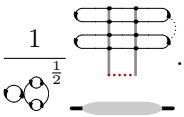 .

Similarly, multiplying out the other three elements in Equation 3.48 gives the complete matrix

$$\begin{pmatrix} a_Y & c_Y \\ c_Y & b_Y \end{pmatrix} = - \left(\text{ 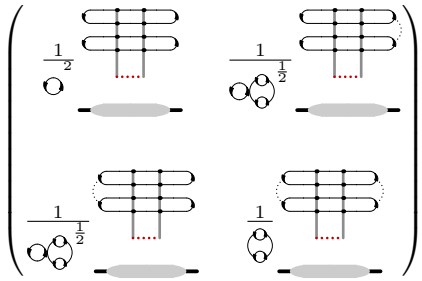 } \right). \tag{3.52}$$

The procedure for calculating these elements exactly has already been outlined in great detail in the previous section for the 2-point and 3-point correlators. The same method can be used to determine a_Y, b_Y and c_Y in terms of G, as has been done in [2]. The results are

$$a_Y = C_f(\mathcal{G}'_{\boldsymbol{xy}} + \mathcal{G}'_{\boldsymbol{x'y'}}) \tag{3.53}$$

$$b_Y = \left(C_f - \frac{C_A}{2}\right)(\mathcal{G}'_{\boldsymbol{xy}} + \mathcal{G}'_{\boldsymbol{x'y'}}) + \frac{C_d + C_A}{4}\left(\mathcal{G}'_{\boldsymbol{x'x}} + \mathcal{G}'_{\boldsymbol{y'y}}\right) - \frac{C_d - C_A}{4}\left(\mathcal{G}'_{\boldsymbol{x'y}} + \mathcal{G}'_{\boldsymbol{y'x}}\right) \tag{3.54}$$

$$c_Y = \frac{\sqrt{d_A/4}}{C_A}\left(\mathcal{G}'_{\boldsymbol{x'x}} + \mathcal{G}'_{\boldsymbol{y'y}} - \mathcal{G}'_{\boldsymbol{x'y}} - \mathcal{G}'_{\boldsymbol{y'x}}\right) \tag{3.55}$$

where $C_d = \frac{N_c^2 - 4}{N_c}$.

Local limits

Taking the limit $\boldsymbol{x} \to \boldsymbol{y}$ on the expressions above gives

$$\lim_{\boldsymbol{x}\to\boldsymbol{y}} a_Y = C_f(\mathcal{G}'_{\boldsymbol{yy}} + \mathcal{G}'_{\boldsymbol{x'y'}}) \tag{3.56}$$

$$\lim_{\boldsymbol{x}\to\boldsymbol{y}} b_Y = \left(C_f - \frac{C_A}{2}\right)(\mathcal{G}'_{\boldsymbol{yy}} + \mathcal{G}'_{\boldsymbol{x'y'}}) + \frac{C_A}{2}(\mathcal{G}'_{\boldsymbol{x'y}} + \mathcal{G}'_{\boldsymbol{y'y}}) \tag{3.57}$$

$$\lim_{\boldsymbol{x}\to\boldsymbol{y}} c_Y = 0. \tag{3.58}$$

The off-diagonal elements of $\mathcal{A}(Y)$ become zero because of the unitarity of the Wilson lines, $U_{\boldsymbol{x}}U^\dagger_{\boldsymbol{x}} = \mathbb{1}$. In either of these limits then, $\mathcal{A}(Y)$ becomes diagonal with the top element a 2-point correlator and the bottom element a 3-point correlator. By Equation 3.46, the diagonalisation of $\mathcal{A}(Y)$ leads to a decoupling of the differential equations for its individual elements. The solutions of such simple differential equations for correlators have already been discussed in the previous section, the resulting expressions being Equations 3.20 and 3.34, respectively. Taking a second limit, $\boldsymbol{x'} \to \boldsymbol{y'}$, reduces the results further to

$$\lim_{\substack{\boldsymbol{x}\to\boldsymbol{y}\\ \boldsymbol{x'}\to\boldsymbol{y'}}} a_Y = C_f(\mathcal{G}'_{\boldsymbol{yy}} + \mathcal{G}'_{\boldsymbol{y'y'}}) \tag{3.59}$$

$$\lim_{\substack{\boldsymbol{x}\to\boldsymbol{y}\\ \boldsymbol{x'}\to\boldsymbol{y'}}} b_Y = \left(C_f - \frac{C_A}{2}\right)(\mathcal{G}'_{\boldsymbol{yy}} + \mathcal{G}'_{\boldsymbol{y'y'}}) + C_A\mathcal{G}'_{\boldsymbol{y'y}}. \tag{3.60}$$

The limits $\boldsymbol{x} \to \boldsymbol{y'}$ and $\boldsymbol{x'} \to \boldsymbol{y}$ have a similar outcome. The last set of limits is $\boldsymbol{x} \to \boldsymbol{x'}$ and $\boldsymbol{y} \to \boldsymbol{y'}$, corresponding to taking the two quarks on top of each other and the two antiquarks on top of each other. To make sense of this, it is necessary to change to a third set of equivalent basis states,

$$\frac{1}{\left(\frac{N_c(N_c+1)}{2}\right)^{\frac{1}{2}}}$$  and $$\frac{1}{\left(\frac{N_c(N_c-1)}{2}\right)^{\frac{1}{2}}}$$  (3.61)

where

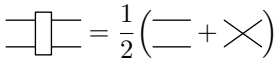 and 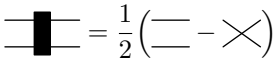 (3.62)

are symmetry and antisymmetry operators, respectively. A more detailed discussion of this case is given in [2].

3.2.2 Exponential solution for $\mathcal{A}(Y)$

Outside of the limits, there exists a differential matrix equation, Equation 3.46, with non-trivial expressions for the elements of $\mathcal{M}(Y)$ given above. This can be integrated to yield

$$\mathcal{A}(Y) = P_Y \exp\left\{ -\int_{Y_0}^{Y} dY' \, \mathcal{M}(Y') \right\} \mathcal{A}(Y_0) \tag{3.63}$$

where P_Y denotes path ordering in rapidity and the normalisation factor $\mathcal{A}(Y_0)$ is set by the initial condition. The information given up until now is insufficient to determine $\mathcal{A}(Y_0)$ but constraints can be imposed by coincidence limits such as those discussed in Section 3.1.4.

Rigid exponential solution

The part of the solution unconstrained by the coincidence limits is contained in the difference between the full solution given in Equation 3.63 and the *rigid exponential*

$$\mathcal{A}^{\text{rigid}}(Y) := \exp\left\{ -\int^{Y} dY' \mathcal{M}(Y') \right\} \tag{3.64}$$

$$= \exp\left\{ -\begin{pmatrix} \mathsf{a}_Y & \mathsf{c}_Y \\ \mathsf{c}_Y & \mathsf{b}_Y \end{pmatrix} \right\} \tag{3.65}$$

$$= \exp\left\{ -\frac{1}{2}(\mathsf{a}_Y + \mathsf{b}_Y) \right\} \begin{pmatrix} \cosh k - \frac{\mathsf{a}_Y - \mathsf{b}_Y}{\sqrt{\Delta_Y}} \sinh k & -2\frac{\mathsf{c}_Y}{\sqrt{\Delta_Y}} \sinh k \\ -2\frac{\mathsf{c}_Y}{\sqrt{\Delta_Y}} \sinh k & \cosh k + \frac{\mathsf{a}_Y - \mathsf{b}_Y}{\sqrt{\Delta_Y}} \sinh k \end{pmatrix} \tag{3.66}$$

where

$$\mathsf{a}_Y := \int^{Y} dY' a_{Y'}, \qquad \mathsf{b}_Y := \int^{Y} dY' b_{Y'}, \qquad \mathsf{c}_Y := \int^{Y} dY' c_{Y'} \qquad \text{and} \qquad k := \frac{1}{2}\sqrt{(\mathsf{a}_Y - \mathsf{b}_Y)^2 + 4\mathsf{c}_Y^2}.$$

$\mathcal{A}^{\text{rigid}}(Y)$ is an expression solely in terms of $\mathcal{G}(Y)$ and involves no rapidity-ordered terms $\mathcal{G}'(Y)$. In the local limits, it is identical to $\mathcal{A}(Y)$.

The large N_c limit is not useful here because it over-simplifies all expressions for $\mathcal{A}(Y)$, losing all path-ordering. What is useful, however, is to write an ansatz for $\mathcal{G}$ that separates Y-dependence from transverse coordinate-dependence,

$$\mathcal{G}_{\boldsymbol{xy}}(Y) \to f(Y) g(\boldsymbol{x}, \boldsymbol{y}). \tag{3.67}$$

This is the approach taken by the Golec-Biernat-Wüsthoff parametrisation [66] and the McLerran-Venugopalan model [67], which have been successful in phenomenological studies. It is not consistent with the GT since it assumes that Y-ordering plays no role in $\mathcal{A}(Y)$. For comparisons to data within the GT, one can use

$$\mathcal{A}(Y) := P_Y \exp\left\{ -\int_{Y_0-\Delta Y}^{Y} dY' \mathcal{M}(Y') \right\} \cdot \mathcal{A}^{\text{rigid}}(Y_0 - \Delta Y) \tag{3.68}$$

in the region $Y > Y_0$. The assumption is made that nonlinearities in the evolution equation erase most of the arbitrariness introduced by the initial condition. Such studies are beyond the scope of this work.

3.2.3 Symmetrisation of the GT definition

The most obvious extension of the GT is to consider differential operators $i\nabla^a_{\boldsymbol{u}} i\nabla^a_{\boldsymbol{v}}$ acting to the right of the target line in the argument of the exponential of Equation 3.5. Since the only *effective* difference between the operation of $i\nabla^a_{\boldsymbol{u}}$ and $i\bar{\nabla}^a_{\boldsymbol{u}}$ on the same Wilson line is a sign (c.f. Equations 2.41 and 2.42), it turns out that all the arguments discussed in this chapter hold equally well for this new case but with one small difference. Recall Equation 3.63,

$$\mathcal{A}(Y) = P_Y \exp\left\{ -\int_{Y_0}^{Y} dY' \, \mathcal{M}(Y') \right\} \mathcal{A}(Y_0), \tag{3.69}$$

with P_Y denoting path-ordering in rapidity. This was the result corresponding to differential operators acting to the left of the target, with sequential gluon insertion lines being added further away from the target line. If one now considers differential operators acting to the right of the target, then the path-ordering should be reversed to ensure that sequential gluon lines still get added at increasing distance from the target. Since $\mathcal{M}(Y)$ is a symmetric matrix, there is no need to worry about transposing it.

Including the differential operator $i\nabla^a_{\boldsymbol{u}} i\nabla^a_{\boldsymbol{v}}$ in the GT introduced in [2] is therefore a trivial matter. The new, symmetric approximation is then

$$\frac{d}{dY}\Big\langle F\big[U\big]\Big\rangle_Y = -\frac{1}{2}\Big\langle \int d^2u\, d^2v\, G_{Y,\boldsymbol{uv}}\, \frac{1}{2}\Big(i\bar{\nabla}^a_{\boldsymbol{u}} i\bar{\nabla}^a_{\boldsymbol{v}} + i\nabla^a_{\boldsymbol{u}} i\nabla^a_{\boldsymbol{v}}\Big)\, F\big[U\big]\Big\rangle \tag{3.70}$$

and all the conceptual arguments presented in this section still hold. Including the mixed operator $i\nabla^a_{\boldsymbol{u}} i\bar{\nabla}^a_{\boldsymbol{v}}$ on the other hand, is a more complicated affair because it requires changing the target interaction to include a gluon Wilson line. Such studies are beyond the scope of this work but it is still possible to go beyond the GT in a meaningful way by considering higher-order differential operators.

Chapter 4

Beyond the Gaussian Truncation

In the previous chapter, the Gaussian truncation of the JIMWLK equation was introduced by approximating the average of a generic correlator by

$$\Big\langle F\big[U\big]\Big\rangle_Y = \exp\bigg\{-\frac{1}{2}\int^Y dY' \int d^2u\, d^2v\, G_{\boldsymbol{uv}}\, i\bar{\nabla}^a_{\boldsymbol{u}} i\bar{\nabla}^a_{\boldsymbol{v}}\bigg\} F\big[U\big].$$

With this providing the baseline for a calculation, any higher-order extensions act as corrections. This chapter introduces the leading-order correction to the GT in Section 4.1 and then looks at the 4-point correlator in this extension in Section 4.2. The last section uses these results to modify the parametrisation equations for the 2-point and 3-point correlators.

4.1 Extension of the GT Differential Operator

The GT can be expanded in the first instance by including triple-derivative terms in the parametrisation of a Wilson line average:

$$\begin{aligned}\Big\langle F\big[U\big]\Big\rangle_Y = \exp\bigg\{-\int^Y dY'\Big(&\frac{1}{2}\int d^2u\, d^2v\, G_{\boldsymbol{uv}}\, i\bar{\nabla}^a_{\boldsymbol{u}} i\bar{\nabla}^a_{\boldsymbol{v}} \\ &+\int d^2u\, d^2v\, d^2w\,\Big[f^{abc}G^f_{\boldsymbol{uvw}} + d^{abc}G^d_{\boldsymbol{uvw}}\Big] i\bar{\nabla}^a_{\boldsymbol{u}} i\bar{\nabla}^b_{\boldsymbol{v}} i\bar{\nabla}^c_{\boldsymbol{w}}\Big)\bigg\} F\big[U\big]. \qquad (4.1)\end{aligned}$$

Two new terms are introduced to take into account the antisymmetric and symmetric three-gluon states, respectively. While the GT differential operator corresponds to diagrams of the kind

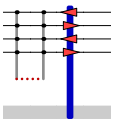

in the 2-dipole correlator case, these new differential operators correspond to diagrams of the kind

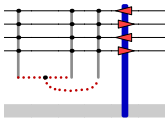
and
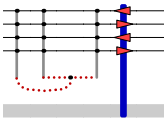

for the f^{abc} term and

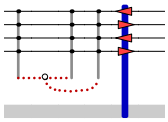
and
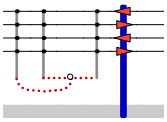

for the d^{abc} term. Of course, this holds just as well if one wants to consider a correlator with an arbitrary number of quarks and antiquarks, 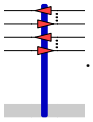 .

As with the GT, the properties of the 3-point functions G^f and G^d are not known *a priori* but will need to be determined. The coordinate integrals that appear on the righthand side of Equation 4.1 automatically symmetrise both G^f and G^d. If one wants to investigate the symmetry properties of these 3-point functions, they need to be written as linear combinations of all possible permutations of $\boldsymbol{u}, \boldsymbol{v}, \boldsymbol{w}$:

$$G^f_{\boldsymbol{uvw}} i\bar{\nabla}^a_{\boldsymbol{u}} i\bar{\nabla}^b_{\boldsymbol{v}} i\bar{\nabla}^c_{\boldsymbol{w}} \longrightarrow \frac{1}{6}\Big[G^f_{\boldsymbol{uvw}} i\bar{\nabla}^a_{\boldsymbol{u}} i\bar{\nabla}^b_{\boldsymbol{v}} i\bar{\nabla}^c_{\boldsymbol{w}} + G^f_{\boldsymbol{vwu}} i\bar{\nabla}^a_{\boldsymbol{v}} i\bar{\nabla}^b_{\boldsymbol{w}} i\bar{\nabla}^c_{\boldsymbol{u}} + G^f_{\boldsymbol{wuv}} i\bar{\nabla}^a_{\boldsymbol{w}} i\bar{\nabla}^b_{\boldsymbol{u}} i\bar{\nabla}^c_{\boldsymbol{v}} + G^f_{\boldsymbol{uwv}} i\bar{\nabla}^a_{\boldsymbol{u}} i\bar{\nabla}^b_{\boldsymbol{w}} i\bar{\nabla}^c_{\boldsymbol{v}} + G^f_{\boldsymbol{vuw}} i\bar{\nabla}^a_{\boldsymbol{v}} i\bar{\nabla}^b_{\boldsymbol{u}} i\bar{\nabla}^c_{\boldsymbol{w}} + G^f_{\boldsymbol{wvu}} i\bar{\nabla}^a_{\boldsymbol{w}} i\bar{\nabla}^b_{\boldsymbol{v}} i\bar{\nabla}^c_{\boldsymbol{u}}\Big] \tag{4.2}$$

$$G^d_{\boldsymbol{uvw}} i\bar{\nabla}^a_{\boldsymbol{u}} i\bar{\nabla}^b_{\boldsymbol{v}} i\bar{\nabla}^c_{\boldsymbol{w}} \longrightarrow \frac{1}{6}\Big[G^d_{\boldsymbol{uvw}} i\bar{\nabla}^a_{\boldsymbol{u}} i\bar{\nabla}^b_{\boldsymbol{v}} i\bar{\nabla}^c_{\boldsymbol{w}} + G^d_{\boldsymbol{vwu}} i\bar{\nabla}^a_{\boldsymbol{v}} i\bar{\nabla}^b_{\boldsymbol{w}} i\bar{\nabla}^c_{\boldsymbol{u}} + G^d_{\boldsymbol{wuv}} i\bar{\nabla}^a_{\boldsymbol{w}} i\bar{\nabla}^b_{\boldsymbol{u}} i\bar{\nabla}^c_{\boldsymbol{v}} + G^d_{\boldsymbol{uwv}} i\bar{\nabla}^a_{\boldsymbol{u}} i\bar{\nabla}^b_{\boldsymbol{w}} i\bar{\nabla}^c_{\boldsymbol{v}} + G^d_{\boldsymbol{vuw}} i\bar{\nabla}^a_{\boldsymbol{v}} i\bar{\nabla}^b_{\boldsymbol{u}} i\bar{\nabla}^c_{\boldsymbol{w}} + G^d_{\boldsymbol{wvu}} i\bar{\nabla}^a_{\boldsymbol{w}} i\bar{\nabla}^b_{\boldsymbol{v}} i\bar{\nabla}^c_{\boldsymbol{u}}\Big] \tag{4.3}$$

The positions of the coordinate indices on the G's should be taken literally in these expressions. If all the indices on the differential operators are put in order in these expressions, then an overall factor of $i\bar{\nabla}^a_{\boldsymbol{u}} i\bar{\nabla}^b_{\boldsymbol{v}} i\bar{\nabla}^c_{\boldsymbol{w}}$ can be pulled out and these somewhat lengthy expressions can be simplified.

4.1.1 Ordering the transverse coordinates

The commutator,

$$[i\bar{\nabla}^a_{\boldsymbol{u}}, i\bar{\nabla}^b_{\boldsymbol{v}}] = if^{abd}\delta_{\boldsymbol{uv}} i\bar{\nabla}^d_{\boldsymbol{u}} = \frac{1}{2} if^{abd}\delta_{\boldsymbol{uv}}\Big(i\bar{\nabla}^d_{\boldsymbol{u}} + i\bar{\nabla}^d_{\boldsymbol{v}}\Big), \tag{4.4}$$

can be used to order the indices $\boldsymbol{u}, \boldsymbol{v}, \boldsymbol{w}$. To illustrate how this is done, consider the term $G^f_{\boldsymbol{vuw}} i\bar{\nabla}^a_{\boldsymbol{v}} i\bar{\nabla}^b_{\boldsymbol{v}} i\bar{\nabla}^c_{\boldsymbol{w}}$ from Equation 4.2 as an example:

$$\begin{aligned}
&G^f_{\boldsymbol{vuw}}\Big(i\bar{\nabla}^a_{\boldsymbol{v}} i\bar{\nabla}^b_{\boldsymbol{u}}\Big) i\bar{\nabla}^c_{\boldsymbol{w}} \\
&= G^f_{\boldsymbol{vuw}}\Big(i\bar{\nabla}^b_{\boldsymbol{u}} i\bar{\nabla}^a_{\boldsymbol{v}} + [i\bar{\nabla}^a_{\boldsymbol{v}}, i\bar{\nabla}^b_{\boldsymbol{u}}]\Big) i\bar{\nabla}^c_{\boldsymbol{w}} \\
&= G^f_{\boldsymbol{vuw}}\Big(i\bar{\nabla}^b_{\boldsymbol{u}} i\bar{\nabla}^a_{\boldsymbol{v}} + \frac{1}{2} if^{abd}\delta_{\boldsymbol{uv}}\big(i\bar{\nabla}^d_{\boldsymbol{u}} + i\bar{\nabla}^d_{\boldsymbol{v}}\big)\Big) i\bar{\nabla}^c_{\boldsymbol{w}} \\
&= G^f_{\boldsymbol{vuw}} i\bar{\nabla}^b_{\boldsymbol{u}} i\bar{\nabla}^a_{\boldsymbol{v}} i\bar{\nabla}^c_{\boldsymbol{w}} + \frac{1}{2} if^{abd}\delta_{\boldsymbol{uv}} G^f_{\boldsymbol{vuw}}\Big(i\bar{\nabla}^d_{\boldsymbol{u}} i\bar{\nabla}^c_{\boldsymbol{w}} + i\bar{\nabla}^d_{\boldsymbol{v}} i\bar{\nabla}^c_{\boldsymbol{w}}\Big) \\
&= G^f_{\boldsymbol{vuw}} i\bar{\nabla}^b_{\boldsymbol{u}} i\bar{\nabla}^a_{\boldsymbol{v}} i\bar{\nabla}^c_{\boldsymbol{w}} + \frac{1}{2} if^{abd}\Big(G^f_{\boldsymbol{uuw}} i\bar{\nabla}^d_{\boldsymbol{u}} i\bar{\nabla}^c_{\boldsymbol{w}} + G^f_{\boldsymbol{vvw}} i\bar{\nabla}^d_{\boldsymbol{v}} i\bar{\nabla}^c_{\boldsymbol{w}}\Big).
\end{aligned} \tag{4.5}$$

In the last line, the delta function $\delta_{\boldsymbol{uv}}$ introduces some freedom in choosing indices for the G^f's of the last two terms. To keep things completely democratic, the second term has been assigned $\boldsymbol{v} \to \boldsymbol{u}$ and the third term has been assigned $\boldsymbol{u} \to \boldsymbol{v}$. It is equally possible to choose either $\boldsymbol{u}$ or $\boldsymbol{v}$ for both terms but this would invite an unnecessary asymmetry in expressions 4.2 and 4.3. Notice that for each use of the commutator, two new terms are introduced, both of which contain only two coordinate indices.

Once this procedure is carried out on all terms in Equation 4.2, the result is

$$\begin{aligned}
&f^{abc} G^f_{\boldsymbol{uvw}} i\bar{\nabla}^a_{\boldsymbol{u}} i\bar{\nabla}^b_{\boldsymbol{v}} i\bar{\nabla}^c_{\boldsymbol{w}} \longrightarrow \\
&\frac{1}{6} f^{abc}\Bigg[G^f_{\boldsymbol{uvw}} i\bar{\nabla}^a_{\boldsymbol{u}} i\bar{\nabla}^b_{\boldsymbol{v}} i\bar{\nabla}^c_{\boldsymbol{w}} + G^f_{\boldsymbol{vwu}} i\bar{\nabla}^c_{\boldsymbol{u}} i\bar{\nabla}^a_{\boldsymbol{v}} i\bar{\nabla}^b_{\boldsymbol{w}} + \frac{1}{2} if^{acd}\Big(G^f_{\boldsymbol{uwu}} i\bar{\nabla}^d_{\boldsymbol{u}} i\bar{\nabla}^b_{\boldsymbol{w}} + G^f_{\boldsymbol{vwv}} i\bar{\nabla}^d_{\boldsymbol{v}} i\bar{\nabla}^b_{\boldsymbol{w}}\Big) \\
&+ \frac{1}{2} if^{bcd}\Big(G^f_{\boldsymbol{vuu}} i\bar{\nabla}^a_{\boldsymbol{v}} i\bar{\nabla}^d_{\boldsymbol{u}} + G^f_{\boldsymbol{vww}} i\bar{\nabla}^a_{\boldsymbol{v}} i\bar{\nabla}^d_{\boldsymbol{w}}\Big) + G^f_{\boldsymbol{wuv}} i\bar{\nabla}^b_{\boldsymbol{u}} i\bar{\nabla}^c_{\boldsymbol{v}} i\bar{\nabla}^a_{\boldsymbol{w}} + \frac{1}{2} if^{abd}\Big(G^f_{\boldsymbol{uuv}} i\bar{\nabla}^d_{\boldsymbol{u}} i\bar{\nabla}^c_{\boldsymbol{v}} + G^f_{\boldsymbol{wwv}} i\bar{\nabla}^d_{\boldsymbol{w}} i\bar{\nabla}^c_{\boldsymbol{v}}\Big) \\
&+ \frac{1}{2} if^{acd}\Big(G^f_{\boldsymbol{vuv}} i\bar{\nabla}^b_{\boldsymbol{u}} i\bar{\nabla}^d_{\boldsymbol{v}} + G^f_{\boldsymbol{wuw}} i\bar{\nabla}^b_{\boldsymbol{u}} i\bar{\nabla}^d_{\boldsymbol{w}}\Big) + G^f_{\boldsymbol{uwv}} i\bar{\nabla}^a_{\boldsymbol{u}} i\bar{\nabla}^c_{\boldsymbol{v}} i\bar{\nabla}^b_{\boldsymbol{w}} + \frac{1}{2} if^{bcd}\Big(G^f_{\boldsymbol{uvv}} i\bar{\nabla}^a_{\boldsymbol{u}} i\bar{\nabla}^d_{\boldsymbol{v}} + G^f_{\boldsymbol{uww}} i\bar{\nabla}^a_{\boldsymbol{u}} i\bar{\nabla}^d_{\boldsymbol{w}}\Big) \\
&+ G^f_{\boldsymbol{vuw}} i\bar{\nabla}^b_{\boldsymbol{u}} i\bar{\nabla}^a_{\boldsymbol{v}} i\bar{\nabla}^c_{\boldsymbol{w}} + \frac{1}{2} if^{abd}\Big(G^f_{\boldsymbol{uuw}} i\bar{\nabla}^d_{\boldsymbol{u}} i\bar{\nabla}^c_{\boldsymbol{w}} + G^f_{\boldsymbol{vvw}} i\bar{\nabla}^d_{\boldsymbol{v}} i\bar{\nabla}^c_{\boldsymbol{w}}\Big) + G^f_{\boldsymbol{wvu}} i\bar{\nabla}^c_{\boldsymbol{u}} i\bar{\nabla}^b_{\boldsymbol{v}} i\bar{\nabla}^a_{\boldsymbol{w}} \\
&+ \frac{1}{2} if^{bcd}\Big(G^f_{\boldsymbol{wuu}} i\bar{\nabla}^a_{\boldsymbol{w}} i\bar{\nabla}^d_{\boldsymbol{u}} + G^f_{\boldsymbol{wvv}} i\bar{\nabla}^a_{\boldsymbol{w}} i\bar{\nabla}^d_{\boldsymbol{v}}\Big) + \frac{1}{2} if^{acd}\Big(G^f_{\boldsymbol{uvu}} i\bar{\nabla}^d_{\boldsymbol{u}} i\bar{\nabla}^b_{\boldsymbol{v}} + G^f_{\boldsymbol{wvw}} i\bar{\nabla}^d_{\boldsymbol{w}} i\bar{\nabla}^b_{\boldsymbol{v}}\Big) \\
&+ \frac{1}{2} if^{abd}\Big(G^f_{\boldsymbol{vvu}} i\bar{\nabla}^c_{\boldsymbol{u}} i\bar{\nabla}^d_{\boldsymbol{v}} + G^f_{\boldsymbol{wwu}} i\bar{\nabla}^c_{\boldsymbol{u}} i\bar{\nabla}^d_{\boldsymbol{w}}\Big)\Bigg].
\end{aligned} \tag{4.6}$$

This expression is messy but it can be simplified by splitting it into two contributions: one for terms

with two differential operators and one for terms with three differential operators:

$$f^{abc}G^f_{\boldsymbol{uvw}}i\bar{\nabla}^a_{\boldsymbol{u}}i\bar{\nabla}^b_{\boldsymbol{v}}i\bar{\nabla}^c_{\boldsymbol{w}} \longrightarrow \left(\hat{G}^{f2}+\hat{G}^{f3}\right) \tag{4.7}$$

where

$$\begin{aligned}\hat{G}^{f2} := \frac{1}{12}if^{abc}\Big[&f^{acd}\Big(G^f_{\boldsymbol{uwu}}i\bar{\nabla}^d_{\boldsymbol{u}}i\bar{\nabla}^b_{\boldsymbol{w}}+G^f_{\boldsymbol{vwv}}i\bar{\nabla}^d_{\boldsymbol{v}}i\bar{\nabla}^b_{\boldsymbol{w}}\Big)+f^{bcd}\Big(G^f_{\boldsymbol{vuu}}i\bar{\nabla}^a_{\boldsymbol{v}}i\bar{\nabla}^d_{\boldsymbol{u}}+G^f_{\boldsymbol{vww}}i\bar{\nabla}^a_{\boldsymbol{v}}i\bar{\nabla}^d_{\boldsymbol{w}}\Big)\\&+f^{abd}\Big(G^f_{\boldsymbol{uuv}}i\bar{\nabla}^d_{\boldsymbol{u}}i\bar{\nabla}^c_{\boldsymbol{v}}+G^f_{\boldsymbol{wwv}}i\bar{\nabla}^d_{\boldsymbol{w}}i\bar{\nabla}^c_{\boldsymbol{v}}\Big)+f^{acd}\Big(G^f_{\boldsymbol{vuv}}i\bar{\nabla}^b_{\boldsymbol{u}}i\bar{\nabla}^d_{\boldsymbol{v}}+G^f_{\boldsymbol{wuw}}i\bar{\nabla}^b_{\boldsymbol{u}}i\bar{\nabla}^d_{\boldsymbol{w}}\Big)\\&+f^{bcd}\Big(G^f_{\boldsymbol{uvv}}i\bar{\nabla}^a_{\boldsymbol{u}}i\bar{\nabla}^d_{\boldsymbol{v}}+G^f_{\boldsymbol{uww}}i\bar{\nabla}^a_{\boldsymbol{u}}i\bar{\nabla}^d_{\boldsymbol{w}}\Big)+f^{abd}\Big(G^f_{\boldsymbol{uuw}}i\bar{\nabla}^d_{\boldsymbol{u}}i\bar{\nabla}^c_{\boldsymbol{w}}+G^f_{\boldsymbol{vvw}}i\bar{\nabla}^d_{\boldsymbol{v}}i\bar{\nabla}^c_{\boldsymbol{w}}\Big)\\&+f^{bcd}\Big(G^f_{\boldsymbol{wuu}}i\bar{\nabla}^a_{\boldsymbol{w}}i\bar{\nabla}^d_{\boldsymbol{u}}+G^f_{\boldsymbol{wvv}}i\bar{\nabla}^a_{\boldsymbol{w}}i\bar{\nabla}^d_{\boldsymbol{v}}\Big)+f^{acd}\Big(G^f_{\boldsymbol{uvu}}i\bar{\nabla}^d_{\boldsymbol{u}}i\bar{\nabla}^b_{\boldsymbol{v}}+G^f_{\boldsymbol{wvw}}i\bar{\nabla}^d_{\boldsymbol{w}}i\bar{\nabla}^b_{\boldsymbol{v}}\Big)\\&+f^{abd}\Big(G^f_{\boldsymbol{vvu}}i\bar{\nabla}^c_{\boldsymbol{u}}i\bar{\nabla}^d_{\boldsymbol{v}}+G^f_{\boldsymbol{wwu}}i\bar{\nabla}^c_{\boldsymbol{u}}i\bar{\nabla}^d_{\boldsymbol{w}}\Big)\Big]\end{aligned} \tag{4.8}$$

and

$$\begin{aligned}\hat{G}^{f3} := \frac{1}{6}f^{abc}\Big[&G^f_{\boldsymbol{uvw}}i\bar{\nabla}^a_{\boldsymbol{u}}i\bar{\nabla}^b_{\boldsymbol{v}}i\bar{\nabla}^c_{\boldsymbol{w}}+G^f_{\boldsymbol{vwu}}i\bar{\nabla}^c_{\boldsymbol{u}}i\bar{\nabla}^a_{\boldsymbol{v}}i\bar{\nabla}^b_{\boldsymbol{w}}+G^f_{\boldsymbol{wuv}}i\bar{\nabla}^b_{\boldsymbol{u}}i\bar{\nabla}^c_{\boldsymbol{v}}i\bar{\nabla}^a_{\boldsymbol{w}}\\&+G^f_{\boldsymbol{uwv}}i\bar{\nabla}^a_{\boldsymbol{u}}i\bar{\nabla}^c_{\boldsymbol{v}}i\bar{\nabla}^b_{\boldsymbol{w}}+G^f_{\boldsymbol{vuw}}i\bar{\nabla}^b_{\boldsymbol{u}}i\bar{\nabla}^a_{\boldsymbol{v}}i\bar{\nabla}^c_{\boldsymbol{w}}+G^f_{\boldsymbol{wvu}}i\bar{\nabla}^c_{\boldsymbol{u}}i\bar{\nabla}^b_{\boldsymbol{v}}i\bar{\nabla}^a_{\boldsymbol{w}}\Big].\end{aligned} \tag{4.9}$$

The G^d result is much simpler because every time the commutator is used to re-order indices, terms with an f^{abc} cancel with the overall d^{abc}. Therefore, only terms with three distinct coordinates can survive -

$$d^{abc}G^d_{\boldsymbol{uvw}}i\bar{\nabla}^a_{\boldsymbol{u}}i\bar{\nabla}^b_{\boldsymbol{v}}i\bar{\nabla}^c_{\boldsymbol{w}} \longrightarrow \hat{G}^d \tag{4.10}$$

where

$$\begin{aligned}\hat{G}^{d} := \frac{1}{6}d^{abc}\Big[&G^d_{\boldsymbol{uvw}}i\bar{\nabla}^a_{\boldsymbol{u}}i\bar{\nabla}^b_{\boldsymbol{v}}i\bar{\nabla}^c_{\boldsymbol{w}}+G^d_{\boldsymbol{wuv}}i\bar{\nabla}^b_{\boldsymbol{u}}i\bar{\nabla}^c_{\boldsymbol{v}}i\bar{\nabla}^a_{\boldsymbol{w}}+G^d_{\boldsymbol{vwu}}i\bar{\nabla}^c_{\boldsymbol{u}}i\bar{\nabla}^a_{\boldsymbol{v}}i\bar{\nabla}^b_{\boldsymbol{w}}\\&+G^d_{\boldsymbol{uwv}}i\bar{\nabla}^a_{\boldsymbol{u}}i\bar{\nabla}^c_{\boldsymbol{v}}i\bar{\nabla}^b_{\boldsymbol{w}}+G^d_{\boldsymbol{vuw}}i\bar{\nabla}^b_{\boldsymbol{u}}i\bar{\nabla}^a_{\boldsymbol{v}}i\bar{\nabla}^c_{\boldsymbol{w}}+G^d_{\boldsymbol{wvu}}i\bar{\nabla}^c_{\boldsymbol{u}}i\bar{\nabla}^b_{\boldsymbol{v}}i\bar{\nabla}^a_{\boldsymbol{w}}\Big].\end{aligned} \tag{4.11}$$

4.1.2 Ordering the colour indices

$\hat{G}^{f2}$, $\hat{G}^{f3}$ and $\hat{G}^d$ are only half of the story; reshuffling coordinate indices has resulted in colour indices being disordered. This can be fixed using the antisymmetry/symmetry of f^{abc}/d^{abc}. This procedure will be outlined below separately for the two-derivative operator, $\hat{G}^{f2}$, and the three-derivative operators $\hat{G}^{f3}$ and $\hat{G}^d$.

The two-derivative operator $\hat{G}^{f2}$

Every term in Equation 4.8 has only two coordinates, which can be relabelled according to the following prescription:

- In terms containing $\boldsymbol{u}$ and $\boldsymbol{w}$, replace $\boldsymbol{w} \to \boldsymbol{v}$
- In terms containing $\boldsymbol{v}$ and $\boldsymbol{w}$, replace $\boldsymbol{w} \to \boldsymbol{u}$.

Then Equation 4.8 becomes

$$\begin{aligned}\hat{G}^{f2} = \frac{1}{12} i f^{abc} \Big[& f^{acd}\Big(G^f_{\boldsymbol{uvu}} i\bar{\nabla}^d_{\boldsymbol{u}} i\bar{\nabla}^b_{\boldsymbol{v}} + G^f_{\boldsymbol{vuv}} i\bar{\nabla}^d_{\boldsymbol{v}} i\bar{\nabla}^b_{\boldsymbol{u}}\Big) + f^{bcd}\Big(G^f_{\boldsymbol{vuu}} i\bar{\nabla}^a_{\boldsymbol{v}} i\bar{\nabla}^d_{\boldsymbol{u}} + G^f_{\boldsymbol{vuu}} i\bar{\nabla}^a_{\boldsymbol{v}} i\bar{\nabla}^d_{\boldsymbol{u}}\Big) \\ & + f^{abd}\Big(G^f_{\boldsymbol{uuv}} i\bar{\nabla}^d_{\boldsymbol{u}} i\bar{\nabla}^c_{\boldsymbol{v}} + G^f_{\boldsymbol{uuv}} i\bar{\nabla}^d_{\boldsymbol{u}} i\bar{\nabla}^c_{\boldsymbol{v}}\Big) + f^{acd}\Big(G^f_{\boldsymbol{vuv}} i\bar{\nabla}^b_{\boldsymbol{u}} i\bar{\nabla}^d_{\boldsymbol{v}} + G^f_{\boldsymbol{vuv}} i\bar{\nabla}^b_{\boldsymbol{u}} i\bar{\nabla}^d_{\boldsymbol{v}}\Big) \\ & + f^{bcd}\Big(G^f_{\boldsymbol{uvv}} i\bar{\nabla}^a_{\boldsymbol{u}} i\bar{\nabla}^d_{\boldsymbol{v}} + G^f_{\boldsymbol{uvv}} i\bar{\nabla}^a_{\boldsymbol{u}} i\bar{\nabla}^d_{\boldsymbol{v}}\Big) + f^{abd}\Big(G^f_{\boldsymbol{uuv}} i\bar{\nabla}^d_{\boldsymbol{u}} i\bar{\nabla}^c_{\boldsymbol{v}} + G^f_{\boldsymbol{vvu}} i\bar{\nabla}^d_{\boldsymbol{v}} i\bar{\nabla}^c_{\boldsymbol{u}}\Big) \\ & + f^{bcd}\Big(G^f_{\boldsymbol{vuu}} i\bar{\nabla}^a_{\boldsymbol{v}} i\bar{\nabla}^d_{\boldsymbol{u}} + G^f_{\boldsymbol{uvv}} i\bar{\nabla}^a_{\boldsymbol{u}} i\bar{\nabla}^d_{\boldsymbol{v}}\Big) + f^{acd}\Big(G^f_{\boldsymbol{uvu}} i\bar{\nabla}^d_{\boldsymbol{u}} i\bar{\nabla}^b_{\boldsymbol{v}} + G^f_{\boldsymbol{uvu}} i\bar{\nabla}^d_{\boldsymbol{u}} i\bar{\nabla}^b_{\boldsymbol{v}}\Big) \\ & + f^{abd}\Big(G^f_{\boldsymbol{vvu}} i\bar{\nabla}^c_{\boldsymbol{u}} i\bar{\nabla}^d_{\boldsymbol{v}} + G^f_{\boldsymbol{vvu}} i\bar{\nabla}^c_{\boldsymbol{u}} i\bar{\nabla}^d_{\boldsymbol{v}}\Big)\Big]. \end{aligned} \tag{4.12}$$

A few straightforward simplifications can be made:

$$\begin{aligned}\hat{G}^{f2} = \frac{1}{12} i f^{abc} \Big[& 2f^{acd} G^f_{\boldsymbol{uvu}} i\bar{\nabla}^d_{\boldsymbol{u}} i\bar{\nabla}^b_{\boldsymbol{v}} + f^{acd} G^f_{\boldsymbol{vuv}} i\bar{\nabla}^d_{\boldsymbol{v}} i\bar{\nabla}^b_{\boldsymbol{u}} + 2f^{acd} G^f_{\boldsymbol{vuv}} i\bar{\nabla}^b_{\boldsymbol{u}} i\bar{\nabla}^d_{\boldsymbol{v}} + f^{acd} G^f_{\boldsymbol{uvu}} i\bar{\nabla}^d_{\boldsymbol{u}} i\bar{\nabla}^b_{\boldsymbol{v}} \\ & + 3f^{bcd} G^f_{\boldsymbol{uvv}} i\bar{\nabla}^a_{\boldsymbol{u}} i\bar{\nabla}^d_{\boldsymbol{v}} + 3f^{bcd} G^f_{\boldsymbol{vuu}} i\bar{\nabla}^a_{\boldsymbol{v}} i\bar{\nabla}^d_{\boldsymbol{u}} + 3f^{abd} G^f_{\boldsymbol{uuv}} i\bar{\nabla}^d_{\boldsymbol{u}} i\bar{\nabla}^c_{\boldsymbol{v}} \\ & + 2f^{abd} G^f_{\boldsymbol{vvu}} i\bar{\nabla}^c_{\boldsymbol{u}} i\bar{\nabla}^d_{\boldsymbol{v}} + f^{abd} G^f_{\boldsymbol{vvu}} i\bar{\nabla}^d_{\boldsymbol{v}} i\bar{\nabla}^c_{\boldsymbol{u}}\Big] \end{aligned} \tag{4.13}$$

$$\begin{aligned} = \frac{1}{12} i f^{abc} \Big[& f^{acd}\Big(2G^f_{\boldsymbol{uvu}} i\bar{\nabla}^d_{\boldsymbol{u}} i\bar{\nabla}^b_{\boldsymbol{v}} + G^f_{\boldsymbol{uvu}} i\bar{\nabla}^d_{\boldsymbol{u}} i\bar{\nabla}^b_{\boldsymbol{v}} + 2G^f_{\boldsymbol{vuv}} i\bar{\nabla}^b_{\boldsymbol{u}} i\bar{\nabla}^d_{\boldsymbol{v}} + G^f_{\boldsymbol{vuv}} i\bar{\nabla}^d_{\boldsymbol{v}} i\bar{\nabla}^b_{\boldsymbol{u}}\Big) \\ & + 3f^{bcd}\Big(G^f_{\boldsymbol{uvv}} i\bar{\nabla}^a_{\boldsymbol{u}} i\bar{\nabla}^d_{\boldsymbol{v}} + G^f_{\boldsymbol{vuu}} i\bar{\nabla}^a_{\boldsymbol{v}} i\bar{\nabla}^d_{\boldsymbol{u}}\Big) \\ & + f^{abd}\Big(3G^f_{\boldsymbol{uuv}} i\bar{\nabla}^d_{\boldsymbol{u}} i\bar{\nabla}^c_{\boldsymbol{v}} + 2G^f_{\boldsymbol{vvu}} i\bar{\nabla}^c_{\boldsymbol{u}} i\bar{\nabla}^d_{\boldsymbol{v}} + G^f_{\boldsymbol{vvu}} i\bar{\nabla}^d_{\boldsymbol{v}} i\bar{\nabla}^c_{\boldsymbol{u}}\Big)\Big]. \end{aligned} \tag{4.14}$$

After writing each f^{abc} above as a difference of traces,

$$f^{abc} = -2i\Big(\mathrm{tr}(t^a t^b t^c) - \mathrm{tr}(t^a t^c t^b)\Big),$$

the Fierz identity can be used to simplify products of two f^{abc}'s. The result contains terms with traces over two t^a's, which can also be simplified using $\mathrm{tr}(t^a t^b) = \frac{1}{2}\delta_{ab}$:

$$\hat{G}^{f2} = \frac{iN_c}{6}\Big[-2G^f_{\boldsymbol{uvu}} i\bar{\nabla}^b_{\boldsymbol{u}} i\bar{\nabla}^b_{\boldsymbol{v}} - G^f_{\boldsymbol{uvu}} i\bar{\nabla}^b_{\boldsymbol{u}} i\bar{\nabla}^b_{\boldsymbol{v}} - 2G^f_{\boldsymbol{vuv}} i\bar{\nabla}^b_{\boldsymbol{u}} i\bar{\nabla}^b_{\boldsymbol{v}} - G^f_{\boldsymbol{vuv}} i\bar{\nabla}^b_{\boldsymbol{v}} i\bar{\nabla}^b_{\boldsymbol{u}} + 3G^f_{\boldsymbol{uvv}} i\bar{\nabla}^a_{\boldsymbol{u}} i\bar{\nabla}^a_{\boldsymbol{v}} + 3G^f_{\boldsymbol{vuu}} i\bar{\nabla}^a_{\boldsymbol{v}} i\bar{\nabla}^a_{\boldsymbol{u}} + 3G^f_{\boldsymbol{uuv}} i\bar{\nabla}^c_{\boldsymbol{u}} i\bar{\nabla}^c_{\boldsymbol{v}} + 2G^f_{\boldsymbol{vvu}} i\bar{\nabla}^c_{\boldsymbol{u}} i\bar{\nabla}^c_{\boldsymbol{v}} + G^f_{\boldsymbol{vvu}} i\bar{\nabla}^c_{\boldsymbol{v}} i\bar{\nabla}^c_{\boldsymbol{u}} \Big]. \tag{4.15}$$

Now that each term has only one colour index, these can be relabelled $b, c \to a$. Also using $[i\bar{\nabla}^a_{\boldsymbol{u}}, i\bar{\nabla}^a_{\boldsymbol{v}}] = 0$ gives

$$\begin{aligned}\hat{G}^{f2} &= \frac{iN_c}{6}\Big[-2G^f_{\boldsymbol{uvu}} - G^f_{\boldsymbol{uvu}} - 2G^f_{\boldsymbol{vuv}} - G^f_{\boldsymbol{vuv}} + 3G^f_{\boldsymbol{uvv}} + 3G^f_{\boldsymbol{vuu}} + 3G^f_{\boldsymbol{uuv}} + 2G^f_{\boldsymbol{vvu}} + G^f_{\boldsymbol{vvu}} \Big] i\bar{\nabla}^a_{\boldsymbol{u}} i\bar{\nabla}^a_{\boldsymbol{v}} \\ &= \frac{iN_c}{6}\Big[-3G^f_{\boldsymbol{uvu}} - 3G^f_{\boldsymbol{vuv}} + 3G^f_{\boldsymbol{uvv}} + 3G^f_{\boldsymbol{vuu}} + 3G^f_{\boldsymbol{uuv}} + 3G^f_{\boldsymbol{vvu}} \Big] i\bar{\nabla}^a_{\boldsymbol{u}} i\bar{\nabla}^a_{\boldsymbol{v}}. \end{aligned} \tag{4.16}$$

It may be useful to highlight the symmetry of the product $i\bar{\nabla}^a_{\boldsymbol{u}} i\bar{\nabla}^a_{\boldsymbol{v}}$ by writing it in terms of the anti-commutator

$$\hat{G}^{f2} = \frac{iN_c}{4}\Big[-G^f_{\boldsymbol{uvu}} - G^f_{\boldsymbol{vuv}} + G^f_{\boldsymbol{uvv}} + G^f_{\boldsymbol{vuu}} + G^f_{\boldsymbol{uuv}} + G^f_{\boldsymbol{vvu}} \Big] \{ i\bar{\nabla}^a_{\boldsymbol{u}}, i\bar{\nabla}^a_{\boldsymbol{v}} \}, \tag{4.17}$$

which is only possible because $\frac{1}{2}\{i\bar{\nabla}^a_{\boldsymbol{u}}, i\bar{\nabla}^a_{\boldsymbol{v}}\} = i\bar{\nabla}^a_{\boldsymbol{u}} i\bar{\nabla}^a_{\boldsymbol{v}}$.* It will be shown in the next section (when the new differential operator acts on the 4-point correlator) that this particular linear combination of G^f's is a common feature. One may therefore introduce the symmetric linear combination

$$G^{(2)}_{\boldsymbol{uv}} := \Big(G^f_{\boldsymbol{uuv}} - G^f_{\boldsymbol{uvu}} + G^f_{\boldsymbol{vuu}} \Big) + \Big(G^f_{\boldsymbol{vvu}} - G^f_{\boldsymbol{vuv}} + G^f_{\boldsymbol{uvv}} \Big) \tag{4.18}$$

so that Equation 4.17 becomes

$$\hat{G}^{f2} = \frac{iN_c}{4}\, G^{(2)}_{\boldsymbol{uv}}\, \{ i\bar{\nabla}^a_{\boldsymbol{u}}, i\bar{\nabla}^a_{\boldsymbol{v}} \}. \tag{4.19}$$

After all the lengthy calculations, this is the final expression for the two-derivative piece of the new differential operator.

*This can be shown as follows:

$$\begin{aligned}\{ i\bar{\nabla}^a_{\boldsymbol{u}}, i\bar{\nabla}^a_{\boldsymbol{v}} \} &= i\bar{\nabla}^a_{\boldsymbol{u}} i\bar{\nabla}^a_{\boldsymbol{v}} + i\bar{\nabla}^a_{\boldsymbol{v}} i\bar{\nabla}^a_{\boldsymbol{u}} \\ &= i\bar{\nabla}^a_{\boldsymbol{u}} i\bar{\nabla}^a_{\boldsymbol{v}} + [i\bar{\nabla}^a_{\boldsymbol{v}}, i\bar{\nabla}^a_{\boldsymbol{u}}] + i\bar{\nabla}^a_{\boldsymbol{u}} i\bar{\nabla}^a_{\boldsymbol{v}} \\ &= i\bar{\nabla}^a_{\boldsymbol{u}} i\bar{\nabla}^a_{\boldsymbol{v}} + 0 + i\bar{\nabla}^a_{\boldsymbol{u}} i\bar{\nabla}^a_{\boldsymbol{v}} \\ &= 2i\bar{\nabla}^a_{\boldsymbol{u}} i\bar{\nabla}^a_{\boldsymbol{v}}. \end{aligned}$$

The three-derivative operators $\hat{G}^{f3}$ and $\hat{G}^{d}$

The expressions for $\hat{G}^{f3}$ and $\hat{G}^{d}$ require far less work to re-order colour indices. Since a, b, c are contracted within each term, one can relabel these and use the antisymmetry/symmetry of f^{abc}/d^{abc} to re-order the a, b, c's in the derivatives. The results of this procedure are

$$\hat{G}^{f3} = \frac{1}{6} f^{abc} \Big[G^{f}_{\boldsymbol{uvw}} + G^{f}_{\boldsymbol{vwu}} + G^{f}_{\boldsymbol{wuv}} - G^{f}_{\boldsymbol{uwv}} - G^{f}_{\boldsymbol{vuw}} - G^{f}_{\boldsymbol{wvu}} \Big] i\bar{\nabla}^{a}_{\boldsymbol{u}} i\bar{\nabla}^{b}_{\boldsymbol{v}} i\bar{\nabla}^{c}_{\boldsymbol{w}} \tag{4.20}$$

and

$$\hat{G}^{d} = \frac{1}{6} d^{abc} \Big[G^{f}_{\boldsymbol{uvw}} + G^{f}_{\boldsymbol{vwu}} + G^{f}_{\boldsymbol{wuv}} + G^{f}_{\boldsymbol{uwv}} + G^{f}_{\boldsymbol{vuw}} + G^{f}_{\boldsymbol{wvu}} \Big] i\bar{\nabla}^{a}_{\boldsymbol{u}} i\bar{\nabla}^{b}_{\boldsymbol{v}} i\bar{\nabla}^{c}_{\boldsymbol{w}}. \tag{4.21}$$

4.1.3 Symmetry properties of the complete operator

Now that there are simple, explicit expressions for the various parts of the new differential operator terms introduced in Equation 4.1, their symmetry properties can be determined. These will prove very useful in the following section, where these properties can be used to modify results and maintain correct signs.

The symmetry properties of $\hat{G}^{f2}$, $\hat{G}^{f3}$ and $\hat{G}^{d}$ will be discussed using the symmetry and antisymmetry operators

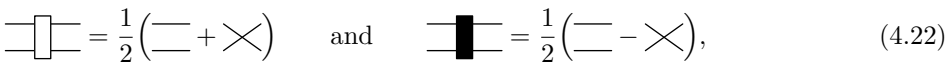

(4.22)

respectively, as defined in the notation of [68]. A generic three-variable object can be expanded into four terms,

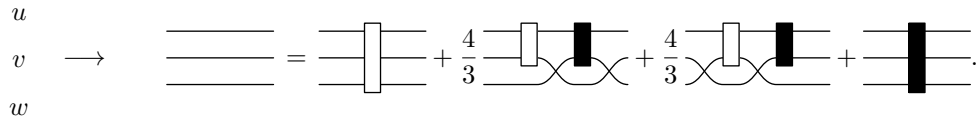

(4.23)

This can be applied to the coordinate indices of each G in Equations 4.2 and 4.3. In order to keep G's corresponding to each of these four terms separated, auxiliary factors m_i ($i \in \{1, 2, 3, 4\}$) are introduced

corresponding to

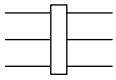 $\longrightarrow \quad m_1$ (4.24)

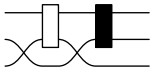 $\longrightarrow \quad m_2$ (4.25)

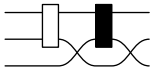 $\longrightarrow \quad m_3$ (4.26)

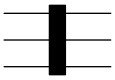 $\longrightarrow \quad m_4.$ (4.27)

The m_i will be set to 1 at the end of the calculation. They are merely a bookkeeping device used to wrap together specific linear combinations of terms corresponding to particular symmetry properties. Separating terms this way results in

$$\begin{aligned}\hat{G}^{f2} = \frac{iN_c}{18}\Big[& m_1\Big[2\Big(G^f_{\boldsymbol{uuv}} + 2G^f_{\boldsymbol{uvu}} + G^f_{\boldsymbol{vuu}}\Big) + G^f_{\boldsymbol{vvu}} + G^f_{\boldsymbol{vuv}} + G^f_{\boldsymbol{uvv}}\Big] \\ & + m_2\Big[2\Big(2G^f_{\boldsymbol{uuv}} - G^f_{\boldsymbol{uvu}} - G^f_{\boldsymbol{vuu}} + G^f_{\boldsymbol{vvu}}\Big) - G^f_{\boldsymbol{vuv}} - G^f_{\boldsymbol{uvv}}\Big] \\ & + m_3\Big[3(-2G^f_{\boldsymbol{uvu}} + 2G^f_{\boldsymbol{vuu}} - G^f_{\boldsymbol{vuv}} + G^f_{\boldsymbol{uvv}})\Big]\Big]\{i\bar{\nabla}^a_{\boldsymbol{u}}, i\bar{\nabla}^a_{\boldsymbol{v}}\}\end{aligned} \tag{4.28}$$

for the two-derivative term. Since the mixed symmetry terms, m_1 and m_2 survive, one can conclude that $\hat{G}^{f2}$ has both symmetric and antisymmetric pieces.

For the $\hat{G}^{f3}$ case, only the m_4 term survives, which means that this operator is totally antisymmetric. Instead of writing the six terms of Equation 4.20, it is more convenient to write

$$\frac{1}{6}\Big[G^f_{\boldsymbol{uvw}} + G^f_{\boldsymbol{vwu}} + G^f_{\boldsymbol{wuv}} - G^f_{\boldsymbol{uwv}} - G^f_{\boldsymbol{vuw}} - G^f_{\boldsymbol{wvu}}\Big] = G^f_{\boldsymbol{uvw}} \tag{4.29}$$

and the complete operator

$$\hat{G}^{f3} = f^{abc}G^f_{\boldsymbol{uvw}}i\bar{\nabla}^a_{\boldsymbol{u}}i\bar{\nabla}^b_{\boldsymbol{v}}i\bar{\nabla}^c_{\boldsymbol{w}} \qquad \text{with } G^f_{\boldsymbol{uvw}} \text{ antisymmetric.} \tag{4.30}$$

(where $G^f_{\boldsymbol{uvw}}$ is understood to be totally antisymmetric).

Lastly, for the $\hat{G}^d$ case, only the m_1 term survives. This means that this operator is totally symmetric and can be written compactly as

$$\hat{G}^d = d^{abc}G^d_{\boldsymbol{uvw}}i\bar{\nabla}^a_{\boldsymbol{u}}i\bar{\nabla}^b_{\boldsymbol{v}}i\bar{\nabla}^c_{\boldsymbol{w}} \qquad \text{with } G^d_{\boldsymbol{uvw}} \text{ symmetric.} \tag{4.31}$$

Putting all the pieces together, the final form of the differential operator in the GT and beyond is

$$\Big\langle F\big[U\big]\Big\rangle_Y = \exp\Bigg\{ -\int^Y dY' \Bigg(\frac{1}{2}\int d^2u\, d^2v \left(G_{Y,\boldsymbol{uv}} + iN_c G^{(2)}_{\boldsymbol{uv}}\right) i\bar{\nabla}^a_{\boldsymbol{u}} i\bar{\nabla}^a_{\boldsymbol{v}} + \int d^2u\, d^2v\, d^2w\, f^{abc} G^f_{\boldsymbol{uvw}} i\bar{\nabla}^a_{\boldsymbol{u}} i\bar{\nabla}^b_{\boldsymbol{v}} i\bar{\nabla}^c_{\boldsymbol{w}} + \int d^2u\, d^2v\, d^2w\, d^{abc} G^d_{\boldsymbol{uvw}} i\bar{\nabla}^a_{\boldsymbol{u}} i\bar{\nabla}^b_{\boldsymbol{v}} i\bar{\nabla}^c_{\boldsymbol{w}} \Bigg)\Bigg\} F\big[U\big] \tag{4.32}$$

with $G^f_{\boldsymbol{uvw}}$ antisymmetric and $G^d_{\boldsymbol{uvw}}$ symmetric. The piece that contributes to the old Gaussian term contains both symmetric and antisymmetric components. It is useful to separate this piece from $\hat{G}^{f3}$ since all the symmetry of the original term, $f^{abc}G^f_{\boldsymbol{uvw}} i\bar{\nabla}^a_{\boldsymbol{u}} i\bar{\nabla}^b_{\boldsymbol{v}} i\bar{\nabla}^c_{\boldsymbol{w}}$, is contained wholly in this two-derivative component, leaving $G^f_{\boldsymbol{uvw}}$ in Equation 4.32 to be totally antisymmetric.

4.2 The 4-point Correlator Beyond the GT

Recall that the 4-point correlator is the object required for the cross-section calculation of interest, so this is the correlator on which the new approximation, Equation 4.32, will be applied. As before, it is convenient to write this as a Y-derivative,

$$\frac{d}{dY}\Big\langle F\big[U\big]\Big\rangle_Y = -\Bigg\langle \Bigg(\frac{1}{2}\int d^2u\, d^2v \left(G_{Y,\boldsymbol{uv}} + iN_c G^{(2)}_{\boldsymbol{uv}}\right) i\bar{\nabla}^a_{\boldsymbol{u}} i\bar{\nabla}^a_{\boldsymbol{v}} + \int d^2u\, d^2v\, d^2w\, f^{abc} G^f_{\boldsymbol{uvw}} i\bar{\nabla}^a_{\boldsymbol{u}} i\bar{\nabla}^b_{\boldsymbol{v}} i\bar{\nabla}^c_{\boldsymbol{w}} + \int d^2u\, d^2v\, d^2w\, d^{abc} G^d_{\boldsymbol{uvw}} i\bar{\nabla}^a_{\boldsymbol{u}} i\bar{\nabla}^b_{\boldsymbol{v}} i\bar{\nabla}^c_{\boldsymbol{w}} \Bigg) F\big[U\big] \Bigg\rangle. \tag{4.33}$$

Since the terms of Equation 4.33 are additive, one can consider acting on $F\big[U\big]$ term-by-term and then adding all results to each other at the end.

The procedure followed here to determine energy evolution equations for the new degrees of freedom, G^f and G^d, is the same as that of Chapter 3. In analogy to Equation 3.47, define new matrices

$$\mathcal{M}_2(Y) := \begin{pmatrix} a_2^Y & c_2^Y \\ c_2^Y & b_2^Y \end{pmatrix}, \qquad \mathcal{M}_f(Y) := \begin{pmatrix} a_f^Y & c_f^Y \\ c_f^Y & b_f^Y \end{pmatrix} \qquad \text{and} \qquad \mathcal{M}_d(Y) := \begin{pmatrix} a_d^Y & c_d^Y \\ c_d^Y & b_d^Y \end{pmatrix} \tag{4.34}$$

corresponding to the second, third and fourth terms in Equation 4.33, respectively. Carrying out the relevant differentiation on the 4-point correlator will determine the elements of these matrices, which

will be expressions in terms of $G^{(2)}$, G^f and G^d, respectively. These will allow one to write new expressions for the 2-point and 3-point correlators in the Balitsky equation for the 2-point correlator by taking the appropriate coincidence limits on the 4-point correlator. This convoluted process will hopefully become clearer to the reader once executed in this section. Not all matrix elements from Equation 4.34 are necessary for the final calculation and not all coincidence limits will be used. For completeness, however, all this information will be included below.

4.2.1 The two-derivative operator $\hat{G}^{f2}$

Consider the differential equation

$\frac{d}{dY}$ 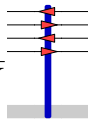 $= -\frac{iN_c}{2}\int d^2u\, d^2v\, G^{(2)}_{\boldsymbol{uv}} i\bar{\nabla}^a_{\boldsymbol{u}} i\bar{\nabla}^a_{\boldsymbol{v}}$ 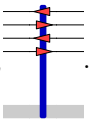 . (4.35)

After applying the differential operator on the righthand side, the final and initial states can be projected onto, to make up the correlator matrix

$\mathcal{A}(Y) =$ 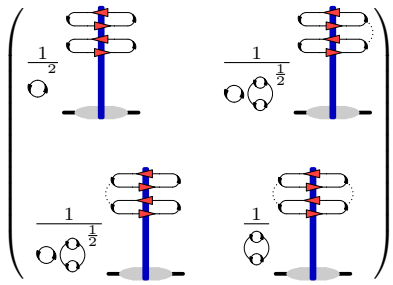 (4.36)

but with "G insertion lines" to the left of the target. The elements of the matrix $\mathcal{M}_2(Y)$ that result are

$$a_2^Y = \frac{iN_c^3}{2}\left(G^f_{\boldsymbol{xxx}} + G^f_{\boldsymbol{yyy}} + G^f_{\boldsymbol{x'x'x'}} + G^f_{\boldsymbol{y'y'y'}} - G^{(2)}_{\boldsymbol{xy}} - G^{(2)}_{\boldsymbol{x'y'}}\right) \tag{4.37}$$

$$b_2^Y = \frac{iN_c d_A}{32}\Big(d_A\Big[G^f_{\boldsymbol{xxx}} + G^f_{\boldsymbol{yyy}} + G^f_{\boldsymbol{x'x'x'}} + G^f_{\boldsymbol{y'y'y'}}\Big] + G^{(2)}_{\boldsymbol{xy}} + G^{(2)}_{\boldsymbol{x'y'}} - 2\Big[G^{(2)}_{\boldsymbol{xx'}} + G^{(2)}_{\boldsymbol{yy'}}\Big] + (1-d_A)\Big[G^{(2)}_{\boldsymbol{xy'}} + G^{(2)}_{\boldsymbol{yx'}}\Big]\Big) \tag{4.38}$$

$$c_2^Y = \frac{iN_c^3\sqrt{d_A}}{8}\left(G^{(2)}_{\boldsymbol{xx'}} - G^{(2)}_{\boldsymbol{xy'}} - G^{(2)}_{\boldsymbol{yx'}} + G^{(2)}_{\boldsymbol{yy'}}\right). \tag{4.39}$$

These results require some interpretation. a_2^Y consists solely of G^f's with indices belonging to a single dipole. Cross-terms, with both primed and unprimed indices, do not appear because this would mean that colour gets carried between the two dipoles (which are in singlet states 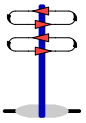 in this case). b_2^Y, on the other hand, contains all possible G^f's with two indices. Here, cross-terms are allowed because the colour transfer they cause can be compensated for by the octet states on either side of the target (recall that b_2^Y corresponds to the correlator 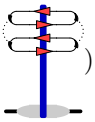). Finally, the transition element c_2^Y, contains all the terms that a_2^Y does not. Since colour is now being exchanged between the two dipoles via the octet state on one side (the transition elements are 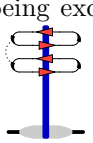 and 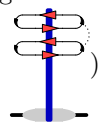), only terms with one-gluon exchange between the dipoles are allowed.

$\mathcal{M}_2(Y)$ in the local limits

In the limit $\boldsymbol{x} \to \boldsymbol{y}$, in which the quark and antiquark of the first dipole are at the same transverse coordinate, the elements of $\mathcal{M}_2(Y)$ become

$$\lim_{\boldsymbol{x}\to\boldsymbol{y}} a_2^Y = \frac{iN_c^3}{2}\left(G^f_{\boldsymbol{x}'\boldsymbol{x}'\boldsymbol{x}'} + G^f_{\boldsymbol{y}'\boldsymbol{y}'\boldsymbol{y}'} - G^{(2)}_{\boldsymbol{x}'\boldsymbol{y}'}\right) \tag{4.40}$$

$$\lim_{\boldsymbol{x}\to\boldsymbol{y}} b_2^Y = \frac{iN_c d_A}{32}\left(2N_c^2 G^f_{\boldsymbol{y}\boldsymbol{y}\boldsymbol{y}} + d_A\left[G^f_{\boldsymbol{x}'\boldsymbol{x}'\boldsymbol{x}'} + G^f_{\boldsymbol{y}'\boldsymbol{y}'\boldsymbol{y}'}\right] - N_c^2\left[G^{(2)}_{\boldsymbol{y}\boldsymbol{x}'} + G^{(2)}_{\boldsymbol{y}\boldsymbol{y}'}\right] + G^{(2)}_{\boldsymbol{x}'\boldsymbol{y}'}\right) \tag{4.41}$$

$$\lim_{\boldsymbol{x}\to\boldsymbol{y}} c_2^Y = 0. \tag{4.42}$$

In this limit, all traces of the first dipole vanish in a_2^Y because there is no way for it to connect to the second dipole. c_2^Y becomes zero as all terms cancel pairwise, which can be deduced easily by looking at Equation 4.39.* In addition to the limit $\boldsymbol{x} \to \boldsymbol{y}$, one can impose a second limit, $\boldsymbol{x}' \to \boldsymbol{y}'$, on these

*Writing $\hat{G}^{f2}$ in the expansion of Equation 4.28 shows that each m_i goes to zero independently in the limit $\boldsymbol{x} \to \boldsymbol{y}$.

expressions. This gives

$$\lim_{\substack{\boldsymbol{x}\to\boldsymbol{y}\\ \boldsymbol{x}'\to\boldsymbol{y}'}} a_2^Y = 0 \tag{4.43}$$

$$\lim_{\substack{\boldsymbol{x}\to\boldsymbol{y}\\ \boldsymbol{x}'\to\boldsymbol{y}'}} b_2^Y = \frac{iN_c^3 d_A}{16}\Big(G^f_{\boldsymbol{yyy}} + G^f_{\boldsymbol{y'y'y'}} - G^{(2)}_{\boldsymbol{yy'}}\Big). \tag{4.44}$$

a_2^Y goes to zero by the same logic that all one-dipole terms vanished in the first limit.

The other limit that can be studied is $\boldsymbol{x} \to \boldsymbol{y'}$, which corresponds to the quark of the first dipole and the antiquark of the second dipole sharing the same transverse coordinate. The results for the elements of $\mathcal{M}_2(Y)$ are

$$\lim_{\boldsymbol{x}\to\boldsymbol{y'}} a_2^Y = \frac{iN_c^3}{2}\Big(G^f_{\boldsymbol{yyy}} + G^f_{\boldsymbol{x'x'x'}} + G^f_{\boldsymbol{y'y'y'}} - G^{(2)}_{\boldsymbol{yy'}} - G^{(2)}_{\boldsymbol{x'y'}}\Big) \tag{4.45}$$

$$\lim_{\boldsymbol{x}\to\boldsymbol{y'}} b_2^Y = \frac{iN_c d_A}{32}\Big(d_A G^f_{\boldsymbol{yyy}} + d_A G^f_{\boldsymbol{x'x'x'}} + 2G^f_{\boldsymbol{y'y'y'}} + (1-d_A)G^{(2)}_{\boldsymbol{yx'}}\Big) \tag{4.46}$$

$$\lim_{\boldsymbol{x}\to\boldsymbol{y'}} c_2^Y = \frac{iN_c^3\sqrt{d_A}}{8}\Big(-2G^f_{\boldsymbol{y'y'y'}} - G^{(2)}_{\boldsymbol{yx'}} + G^{(2)}_{\boldsymbol{yy'}} + G^{(2)}_{\boldsymbol{x'y'}}\Big). \tag{4.47}$$

The terms in a_2^Y that vanished in the limit $\boldsymbol{x} \to \boldsymbol{y}$ no longer vanish because the limit now connects the two dipoles to each other. c_2^Y also has a chance to survive because there is no longer a pairwise cancellation of terms. Taking a second limit, $\boldsymbol{x'} \to \boldsymbol{y'}$, in these results gives:

$$\lim_{\substack{\boldsymbol{x}\to\boldsymbol{y'}\\ \boldsymbol{x}'\to\boldsymbol{y}}} a_2^Y = iN_c^3\Big(G^f_{\boldsymbol{yyy}} + G^f_{\boldsymbol{y'y'y'}} - G^{(2)}_{\boldsymbol{yy'}}\Big) \tag{4.48}$$

$$\lim_{\substack{\boldsymbol{x}\to\boldsymbol{y'}\\ \boldsymbol{x}'\to\boldsymbol{y}}} b_2^Y = \frac{iN_c d_A}{16}\Big(G^f_{\boldsymbol{yyy}} + G^f_{\boldsymbol{y'y'y'}} - G^{(2)}_{\boldsymbol{yy'}}\Big) \tag{4.49}$$

$$\lim_{\substack{\boldsymbol{x}\to\boldsymbol{y'}\\ \boldsymbol{x}'\to\boldsymbol{y}}} c_2^Y = -\frac{iN_c^3\sqrt{d_A}}{4}\Big(G^f_{\boldsymbol{yyy}} + G^f_{\boldsymbol{y'y'y'}} - G^{(2)}_{\boldsymbol{yy'}}\Big). \tag{4.50}$$

In this case, all the elements have the same G content but different pre-factors.

As in the GT, it is possible to study other limits as well, such as $\boldsymbol{x} \to \boldsymbol{x'}$. This would require a change of basis, as discussed briefly in Chapter 3.

4.2.2 The three-derivative operator $\hat{G}^{f3}$

It is now left to consider the triple-derivative terms in Equation 4.33. First, consider the differential equation

$$\frac{d}{dY}$$ 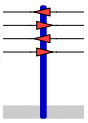 $$= -\int d^2u\, d^2v\, d^2w\, f^{abc} G^f_{\boldsymbol{uvw}} i\bar{\nabla}^a_{\boldsymbol{u}} i\bar{\nabla}^b_{\boldsymbol{v}} i\bar{\nabla}^c_{\boldsymbol{w}}$$ 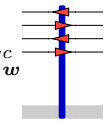 (4.51)

and then project onto initial and final states to make the 2×2 correlator matrix. Since $G^f_{\boldsymbol{uvw}}$ is totally antisymmetric, only G^f's with three coordinates indices can appear in $\mathcal{M}_f(Y)$. This sets a^Y_f to zero immediately because G^f's in the singlet-singlet element cannot connect to both dipoles.

The elements of $\mathcal{M}_f(Y)$ turn out to be

$$a^Y_f = 0 \tag{4.52}$$

$$b^Y_f = 0 \tag{4.53}$$

$$c^Y_f = \frac{3iN_c^2\sqrt{d_A}}{2}\left(G^f_{\boldsymbol{xyx'}} - G^f_{\boldsymbol{xyy'}} + G^f_{\boldsymbol{xx'y'}} - G^f_{\boldsymbol{yx'y'}}\right) \tag{4.54}$$

As expected, $a^Y_f = 0$. In practise, this happens because all terms contain a factor $\mathrm{tr}(t^a) = 0$. The disappearance of b^Y_f is somewhat unexpected. It can be explained by expanding each octet state into two terms using the Fierz identity (Equation 3.2):

2 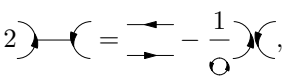 , which bent over, looks like 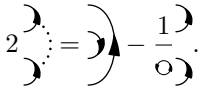 (4.55)

Then the octet-octet correlator becomes four terms,

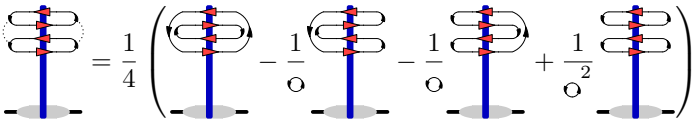 (4.56)

By the same reasoning that $a^Y_f = 0$, so too are the first and last terms of this expansion zero. The remaining terms,

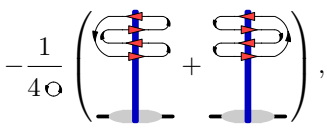

are traces in opposite directions and so cancel each other. Then all terms in Equation 4.56 disappear and b_f^Y becomes zero. c_f^Y, on the other hand, makes no colour flow transgressions and so all possible antisymmetric G^f's are present. The relative signs among the terms in c_f^Y are due to the sign difference between the differential operator $i\bar{\nabla}$ acting on a quark or antiquark.

$\mathcal{M}_f(Y)$ in the local limits

The coincidence limits are easy to evaluate for $\mathcal{M}_f(Y)$ because the antisymmetry of $\hat{G}^f$ makes the elements all zero. c_2^Y evaluated in the various limits becomes

$$\lim_{\boldsymbol{x}\to\boldsymbol{y}} c_f^Y = 0 \tag{4.57}$$

$$\lim_{\substack{\boldsymbol{x}\to\boldsymbol{y}\\ \boldsymbol{x}'\to\boldsymbol{y}'}} c_f^Y = 0 \tag{4.58}$$

$$\lim_{\boldsymbol{x}\to\boldsymbol{y}'} c_f^Y = 0 \tag{4.59}$$

$$\lim_{\substack{\boldsymbol{x}\to\boldsymbol{y}'\\ \boldsymbol{x}'\to\boldsymbol{y}}} c_f^Y = 0. \tag{4.60}$$

4.2.3 The three-derivative operator $\hat{G}^d$

The last term of Equation 4.33 that must be considered is the one containing the totally symmetric 3-point function, G^d. The corresponding differential equation to study is

$$\frac{d}{dY}$$ 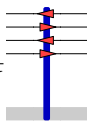 $$= -\int d^2u\, d^2v\, d^2w\, d^{abc} G^d_{\boldsymbol{uvw}} i\bar{\nabla}^a_{\boldsymbol{u}} i\bar{\nabla}^b_{\boldsymbol{v}} i\bar{\nabla}^c_{\boldsymbol{w}}$$ 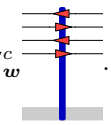 . (4.61)

One can expect the elements of $\mathcal{M}_d(Y)$ to be far richer than the those of $\mathcal{M}_f(Y)$ because the antisymmetry of G^f that lead to several terms cancelling then, is no longer present.

The elements of $\mathcal{M}_d(Y)$ are

$$a_d^Y = \frac{-3iC_dC_f}{2}\left(\frac{1}{3}\Big[G^d_{\boldsymbol{xxx}} - G^d_{\boldsymbol{yyy}} + G^d_{\boldsymbol{x'x'x'}} - G^d_{\boldsymbol{y'y'y'}}\Big] - G^{\mathcal{O}}_{\boldsymbol{xy}} - G^{\mathcal{O}}_{\boldsymbol{x'y'}}\right) \tag{4.62}$$

$$\begin{aligned} b_d^Y = \frac{-3iC_d}{4N_c}\Bigg(\frac{d_A}{3}\Big[G^d_{\boldsymbol{xxx}} - G^d_{\boldsymbol{yyy}} + G^d_{\boldsymbol{x'x'x'}} - G^d_{\boldsymbol{y'y'y'}}\Big] - 2\Big[G^d_{\boldsymbol{xxx'}} - G^d_{\boldsymbol{yyy'}} + G^d_{\boldsymbol{x'x'x}} - G^d_{\boldsymbol{y'y'y}}\Big] \\ +4\Big[G^d_{\boldsymbol{xyx'}} - G^d_{\boldsymbol{xyy'}} + G^d_{\boldsymbol{xx'y'}} - G^d_{\boldsymbol{yx'y'}}\Big] + G^{\mathcal{O}}_{\boldsymbol{xy}} + G^{\mathcal{O}}_{\boldsymbol{x'y'}} + (1-d_A)\Big[G^{\mathcal{O}}_{\boldsymbol{xy'}} - G^{\mathcal{O}}_{\boldsymbol{yx'}}\Big]\Bigg) \end{aligned} \tag{4.63}$$

$$\begin{aligned} c_d^Y = \frac{-3iN_cC_d\sqrt{d_A}}{4}\Bigg(G^d_{\boldsymbol{xxx'}} - G^d_{\boldsymbol{yyy'}} + G^d_{\boldsymbol{x'x'x}} - G^d_{\boldsymbol{y'y'y}} - 2\Big[G^d_{\boldsymbol{xyx'}} - G^d_{\boldsymbol{xyy'}} + G^d_{\boldsymbol{x'y'x}} - G^d_{\boldsymbol{x'y'y}}\Big] \\ +G^{\mathcal{O}}_{\boldsymbol{xy'}} + G^{\mathcal{O}}_{\boldsymbol{x'y}}\Bigg) \end{aligned} \tag{4.64}$$

where $G^{\mathcal{O}}_{\boldsymbol{xy}} := G^d_{\boldsymbol{xxy}} - G^d_{\boldsymbol{yyx}}$ is a convenient antisymmetric combination to define. As in the a_2^Y case, a_d^Y does not contain any cross terms between the two dipoles due to colour transfer considerations. The factor of $\frac{1}{3}$ that appears here (and also in b_d^Y) is a symmetry factor. All possible permutations of coordinate indices appear in b_d^Y. c_d^Y, however, only contains G^d's that link to both dipoles. This is necessary to compensate for the colour transfer by the octet state on one side of the correlator (recall that c_d^Y refers to the transition elements).

$\mathcal{M}_d(Y)$ in the local limits

These expressions simplify fairly drastically in the limit $\boldsymbol{x} \to \boldsymbol{y}$:

$$\lim_{\boldsymbol{x}\to\boldsymbol{y}} a_d^Y = \frac{-3iC_dC_f}{2}\left(\frac{1}{3}\Big[G^d_{\boldsymbol{x'x'x'}} - G^d_{\boldsymbol{y'y'y'}}\Big] + G^{\mathcal{O}}_{\boldsymbol{x'y'}}\right) \tag{4.65}$$

$$\lim_{\boldsymbol{x}\to\boldsymbol{y}} b_d^Y = \frac{-3iC_d}{4N_c}\left(\frac{d_A}{3}\Big[G^d_{\boldsymbol{x'x'x'}} - G^d_{\boldsymbol{y'y'y'}}\Big] + N_c^2\Big[G^{\mathcal{O}}_{\boldsymbol{yx'}} - G^{\mathcal{O}}_{\boldsymbol{yy'}}\Big] + G^{\mathcal{O}}_{\boldsymbol{x'y'}}\right) \tag{4.66}$$

$$\lim_{\boldsymbol{x}\to\boldsymbol{y}} c_d^Y = 0. \tag{4.67}$$

All terms related to the first dipole vanish in a_d^Y in this limit. Imposing $\boldsymbol{x}' \to \boldsymbol{y}'$ in addition gives zero in all cases:

$$\lim_{\substack{\boldsymbol{x}\to\boldsymbol{y}\\ \boldsymbol{x}'\to\boldsymbol{y}'}} a_d^Y \quad = \quad \lim_{\substack{\boldsymbol{x}\to\boldsymbol{y}\\ \boldsymbol{x}'\to\boldsymbol{y}'}} b_d^Y \quad = \quad 0. \tag{4.68}$$

In the limit $\boldsymbol{x} \to \boldsymbol{y}'$, the elements of $\mathcal{M}_d(Y)$ become

$$\lim_{\boldsymbol{x}\to\boldsymbol{y}'} a_d^Y = \frac{-3iC_dC_f}{2}\bigg(-\frac{1}{3}\Big[G^d_{\boldsymbol{yyy}} - G^d_{\boldsymbol{x}'\boldsymbol{x}'\boldsymbol{x}'}\Big] + G^{\mathcal{O}}_{\boldsymbol{yy}'} - G^{\mathcal{O}}_{\boldsymbol{x}'\boldsymbol{y}'}\bigg) \tag{4.69}$$

$$\lim_{\boldsymbol{x}\to\boldsymbol{y}'} b_d^Y = \frac{-3i}{4N_c}\bigg(\frac{d_A}{3}\Big[G^d_{\boldsymbol{yyy}} + G^d_{\boldsymbol{x}'\boldsymbol{x}'\boldsymbol{x}'}\Big] + G^{\mathcal{O}}_{\boldsymbol{yy}'} - G^{\mathcal{O}}_{\boldsymbol{x}'\boldsymbol{y}'} + (d_A-1)G^{\mathcal{O}}_{\boldsymbol{y}\boldsymbol{x}'}\bigg) \tag{4.70}$$

$$\lim_{\boldsymbol{x}\to\boldsymbol{y}'} c_d^Y = \frac{-3iN_cC_d\sqrt{d_A}}{4}\Big(G^{\mathcal{O}}_{\boldsymbol{y}\boldsymbol{x}'} - G^{\mathcal{O}}_{\boldsymbol{y}\boldsymbol{y}'} + G^{\mathcal{O}}_{\boldsymbol{x}'\boldsymbol{y}'}\Big). \tag{4.71}$$

Taking a second limit, $\boldsymbol{x}' \to \boldsymbol{y}$, once again gives zero in all cases:

$$\lim_{\substack{\boldsymbol{x}\to\boldsymbol{y}'\\ \boldsymbol{x}'\to\boldsymbol{y}}} a_d^Y \quad = \quad \lim_{\substack{\boldsymbol{x}\to\boldsymbol{y}'\\ \boldsymbol{x}'\to\boldsymbol{y}}} b_d^Y \quad = \quad \lim_{\substack{\boldsymbol{x}\to\boldsymbol{y}'\\ \boldsymbol{x}'\to\boldsymbol{y}}} c_d^Y \quad = \quad 0. \tag{4.72}$$

4.3 The Odderon Contribution to the 2- & 3-point Correlators

Now that all the elements of $\mathcal{M}(Y)$, $\mathcal{M}_2(Y)$, $\mathcal{M}_f(Y)$ and $\mathcal{M}_d(Y)$ have been determined and evaluated in all local possible limits, they can be used to write expressions for the four 4-point correlators in $\mathcal{A}(Y)$. These new parametrisation equations provide corrections to the G-expressions for the 2-point and 3-point correlators already calculated in Section 3.1, namely

$$\Big\langle \mathrm{tr}(U_{\boldsymbol{x}}U^\dagger_{\boldsymbol{y}})\Big\rangle_Y = d_f \exp\Big\{ -C_f\mathcal{G}_{\boldsymbol{xy}}\Big\}$$

and

$$\Big\langle \tilde{U}^{ab}_{\boldsymbol{z}}\,\mathrm{tr}(t^aU_{\boldsymbol{x}}t^bU^\dagger_{\boldsymbol{y}})\Big\rangle_Y = C_fd_f\exp\Big\{ -\frac{C_A}{2}\big(\mathcal{G}_{\boldsymbol{xz}}+\mathcal{G}_{\boldsymbol{yz}}-\mathcal{G}_{\boldsymbol{xy}}\big) - C_f\,\mathcal{G}_{\boldsymbol{xy}}\Big\}$$

(Equations 3.20 and 3.34, respectively).

Fortunately, not all of the lengthy expressions constituting these matrix elements are relevant. For the 2-point correlator, only the singlet-singlet elements in the limit $\boldsymbol{x}' \to \boldsymbol{y}'$ need to be considered

because in this limit,

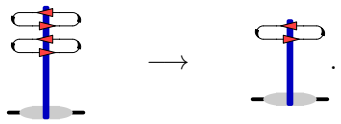

(4.73)

The transition elements and the octet-octet terms necessarily vanish since there is no second dipole for the octet project states to connect to. By similar reasoning, the only relevant matrix elements for the 3-point correlator are the octet-octet terms in the limit $\boldsymbol{x}' \to \boldsymbol{y}'$ because in this limit,

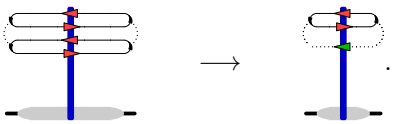

(4.74)

Given these limitations, the only new information that can be added to the parametrisation equations for the 2- and 3-point correlators, come from the elements of $\mathcal{M}_d$; the singlet-singlet and octet-octet elements of $\mathcal{M}_f$ are zero. This is called the *odderon*, the symmetric three-gluon state in the t-channel.

4.3.1 The new 2-point correlator parametrisation

The G^d content for the 2-point correlator is obtained from the matrix element

$$a_d^Y = \frac{-3iC_dC_f}{2}\left(\frac{1}{3}\left[G^d_{\boldsymbol{xxx}} - G^d_{\boldsymbol{yyy}} + G^d_{\boldsymbol{x'x'x'}} - G^d_{\boldsymbol{y'y'y'}}\right] - G^{\mathcal{O}}_{\boldsymbol{xy}} - G^{\mathcal{O}}_{\boldsymbol{x'y'}}\right)$$

given in Equation 4.62. It can be shown that translation invariance (equivalent to conservation of $U = \mathbb{1}$ under evolution) requires G^d with three like indices to be zero. In that case, a_d^Y simplifies neatly to

$$a_d^Y = \frac{3iC_dC_f}{2}\left(G^{\mathcal{O}}_{\boldsymbol{xy}} + G^{\mathcal{O}}_{\boldsymbol{x'y'}}\right). \tag{4.75}$$

Taking the limit $\boldsymbol{x}' \to \boldsymbol{y}'$ to make the second dipole vanish gives*

$$\lim_{\boldsymbol{x}' \to \boldsymbol{y}'} a_d^Y = \frac{3iC_dC_f}{2} G^{\mathcal{O}}_{\boldsymbol{xy}}. \tag{4.76}$$

This is the only new term to be included in the parametrisation of the dipole correlator:

$$\frac{d}{dY}\left\langle \mathrm{tr}(U_{\boldsymbol{x}}U^\dagger_{\boldsymbol{y}})\right\rangle_Y = -\left(C_f\mathcal{G}'_{\boldsymbol{xy}} + \frac{3iC_dC_f}{2} G^{\mathcal{O}}_{\boldsymbol{xy}}\right)(Y)\left\langle \mathrm{tr}(U_{\boldsymbol{x}}U^\dagger_{\boldsymbol{y}})\right\rangle_Y \tag{4.77}$$

*Recall the definition $G^{\mathcal{O}}_{\boldsymbol{xy}} := G^d_{\boldsymbol{xxy}} - G^d_{\boldsymbol{yyx}}$. Then $G^{\mathcal{O}}_{\boldsymbol{xx}}$ is zero under the assumption that $G^d_{\boldsymbol{xxx}}$ is zero by the translation invariance requirement.

(the overall minus sign comes from the definition of $\mathcal{M}(Y)$ - c.f. Equation 3.47). As before, the solution is an exponential,

$$\Big\langle \mathrm{tr}(U_{\boldsymbol{x}}U_{\boldsymbol{y}}^{\dagger})\Big\rangle_{Y} = d_f \exp -\left\{ C_f \mathcal{G}_{\boldsymbol{xy}} + \frac{3iC_dC_f}{2}\, G^{\mathcal{O}}_{\boldsymbol{xy}} \right\}(Y). \tag{4.78}$$

4.3.2 The new 3-point correlator parametrisation

Once again assuming $G^d_{\boldsymbol{xxx}} = 0$, the octet-octet element required for the 3-point correlator is

$$\begin{aligned} b_d^Y = \frac{-3iC_d}{4N_c}\Bigg(-2\Big[G^d_{\boldsymbol{xxx'}} - G^d_{\boldsymbol{yyy'}} + G^d_{\boldsymbol{x'x'x}} - G^d_{\boldsymbol{y'y'y}}\Big] + 4\Big[G^d_{\boldsymbol{xyx'}} - G^d_{\boldsymbol{xyy'}} + G^d_{\boldsymbol{xx'y'}} - G^d_{\boldsymbol{yx'y'}}\Big] \\ + G^{\mathcal{O}}_{\boldsymbol{xy}} + G^{\mathcal{O}}_{\boldsymbol{x'y'}} + (1-d_A)\Big[G^{\mathcal{O}}_{\boldsymbol{xy'}} - G^{\mathcal{O}}_{\boldsymbol{yx'}}\Big]\Bigg) \end{aligned} \tag{4.79}$$

which, in the limit $\boldsymbol{x'} \to \boldsymbol{y'}$, becomes

$$\begin{aligned} \lim_{\boldsymbol{x'}\to\boldsymbol{y'}} b_d^Y = \frac{-3iC_d}{4N_c}\Bigg(-2\Big[G^d_{\boldsymbol{xxy'}} - G^d_{\boldsymbol{yyy'}} + G^d_{\boldsymbol{y'y'x}} - G^d_{\boldsymbol{y'y'y}}\Big] + 4\Big[G^d_{\boldsymbol{xy'y'}} - G^d_{\boldsymbol{yy'y'}}\Big] \\ + G^{\mathcal{O}}_{\boldsymbol{xy}} + (1-d_A)\Big[G^{\mathcal{O}}_{\boldsymbol{xy'}} - G^{\mathcal{O}}_{\boldsymbol{yy'}}\Big]\Bigg). \end{aligned} \tag{4.80}$$

Expanding each $G^{\mathcal{O}}$ to simplify like terms and relabelling $\boldsymbol{y'} = \boldsymbol{z}$ gives

$$\lim_{\boldsymbol{x'}\to\boldsymbol{y'}=\boldsymbol{z}} b_d^Y = \frac{-3iC_d}{4N_c}\Big(G^{\mathcal{O}}_{\boldsymbol{xy}} + N_c^2 G^{\mathcal{O}}_{\boldsymbol{zx}} + N_c^2 G^{\mathcal{O}}_{\boldsymbol{yz}}\Big), \tag{4.81}$$

which is the odderon contribution to the 3-point correlator. This expression can be included in the differential equation for the 3-point correlator (Equation 3.33), resulting in

$$\begin{aligned} \frac{d}{dY}\Big\langle \tilde{U}^{ab}_{\boldsymbol{z}}\,\mathrm{tr}(t^aU_{\boldsymbol{x}}t^bU^{\dagger}_{\boldsymbol{y}})\Big\rangle_Y = -\Bigg[\frac{C_A}{2}\Big(\mathcal{G}'_{\boldsymbol{xz}} + \mathcal{G}'_{\boldsymbol{yz}} - \mathcal{G}'_{\boldsymbol{xy}}\Big) + C_f\,\mathcal{G}'_{\boldsymbol{xy}} \\ - \frac{3iC_d}{4N_c}\Big(G^{\mathcal{O}}_{\boldsymbol{xy}} + N_c^2 G^{\mathcal{O}}_{\boldsymbol{zx}} + N_c^2 G^{\mathcal{O}}_{\boldsymbol{yz}}\Big)\Bigg](Y)\,\Big\langle \tilde{U}^{ab}_{\boldsymbol{z}}\,\mathrm{tr}(t^aU_{\boldsymbol{x}}t^bU^{\dagger}_{\boldsymbol{y}})\Big\rangle_Y. \end{aligned} \tag{4.82}$$

The corresponding exponential solution is

$$\begin{aligned} \Big\langle \tilde{U}^{ab}_{\boldsymbol{z}}\,\mathrm{tr}(t^aU_{\boldsymbol{x}}t^bU^{\dagger}_{\boldsymbol{y}})\Big\rangle_Y = C_f d_f \exp -\Bigg\{ \frac{C_A}{2}\Big(\mathcal{G}_{\boldsymbol{xz}} + \mathcal{G}_{\boldsymbol{yz}} - \mathcal{G}_{\boldsymbol{xy}}\Big) + C_f\,\mathcal{G}_{\boldsymbol{xy}} \\ - \frac{3iC_d}{4N_c}\Big(G^{\mathcal{O}}_{\boldsymbol{xy}} + N_c^2 G^{\mathcal{O}}_{\boldsymbol{zx}} + N_c^2 G^{\mathcal{O}}_{\boldsymbol{yz}}\Big)\Bigg\}(Y). \end{aligned} \tag{4.83}$$

This solution can be verified using a consistency check: In the limit $\boldsymbol{z} \to \boldsymbol{x}$, the 3-point correlator should reduce to the dipole correlator and Equation 4.83 should become Equation 4.78. Since

$$\lim_{\boldsymbol{z}\to\boldsymbol{x}} \left\langle \tilde{U}^{ab}_{\boldsymbol{z}} \mathrm{tr}(t^a U_{\boldsymbol{x}} t^b U^\dagger_{\boldsymbol{y}}) \right\rangle (Y) = C_f d_f \exp - \left\{ C_f \, \mathcal{G}_{\boldsymbol{xy}} + \frac{3iC_dC_f}{2} \, G^{\mathcal{O}}_{\boldsymbol{xy}} \right\} (Y), \tag{4.84}$$

the arguments of the exponentials match and the results are consistent with each other.

4.3.3 Energy evolution of G^d

As with the energy evolution of G within the GT, the 2-point Balitsky equation can be used to determine the evolution of G^d. This time, however, the correct correlator parametrisations to use are Equations 4.78 and 4.83. Substituting these into Equation 3.1 gives

$$\begin{aligned}
&\frac{d}{dY} \left\langle d_f \exp - \left\{ C_f \mathcal{G}_{\boldsymbol{xy}} + \frac{3iC_dC_f}{2} \, G^{\mathcal{O}}_{\boldsymbol{xy}} \right\} (Y) \right\rangle_Y \\
&= \frac{\alpha_s}{\pi^2} \int d^2z \, \tilde{\mathcal{K}}_{\boldsymbol{xzy}} \left\langle C_f d_f \exp - \left\{ \frac{C_A}{2} \Big(\mathcal{G}_{\boldsymbol{xz}} + \mathcal{G}_{\boldsymbol{yz}} - \mathcal{G}_{\boldsymbol{xy}} \Big) + C_f \, \mathcal{G}_{\boldsymbol{xy}} \right.\right. \\
&\left.\left. - \frac{3iC_d}{4N_c} \Big(G^{\mathcal{O}}_{\boldsymbol{xy}} + N_c^2 G^{\mathcal{O}}_{\boldsymbol{zx}} + N_c^2 G^{\mathcal{O}}_{\boldsymbol{yz}} \Big) \right\} (Y) - C_f d_f \exp - \left\{ C_f \mathcal{G}_{\boldsymbol{xy}} + \frac{3iC_dC_f}{2} \, G^{\mathcal{O}}_{\boldsymbol{xy}} \right\} (Y) \right\rangle_Y .
\end{aligned} \tag{4.85}$$

Differentiating the lefthand side and cancelling like factors on both sides gives

$$\begin{aligned}
&\frac{d}{dY} \left\langle \Big(\mathcal{G}_{\boldsymbol{xy}} + \frac{3iC_d}{4} G^{\mathcal{O}}_{\boldsymbol{xy}} \Big) (Y) \right\rangle_Y \\
&= \frac{\alpha_s}{\pi^2} \int d^2z \, \tilde{\mathcal{K}}_{\boldsymbol{xzy}} \left\langle 1 - \exp - \frac{C_A}{2} \left\{ \mathcal{G}_{\boldsymbol{xz}} + \mathcal{G}_{\boldsymbol{yz}} - \mathcal{G}_{\boldsymbol{xy}} + \frac{3iC_d}{4} \Big(N_c^2 G^{\mathcal{O}}_{\boldsymbol{xz}} - N_c^2 G^{\mathcal{O}}_{\boldsymbol{yz}} - G^{\mathcal{O}}_{\boldsymbol{xy}} \Big) \right\} (Y) \right\rangle_Y .
\end{aligned} \tag{4.86}$$

The most striking characteristic about this result is that the odderon contribution has the same structure as the GT contribution. That is, within an overall factor and the actual difference between $\mathcal{G}$ and $G^{\mathcal{O}}$, the linear combination of terms that appear per contribution are the same.

Equation 4.86 is the final evolution equation one can determine for G^d, contained implicitly in $G^{\mathcal{O}}$. Ideally, this could be split into real and imaginary contributions, so that there are separate equations for $\mathcal{G}$ and $G^{\mathcal{O}}$. However, this would require the assumption that $\mathcal{G}$ and $G^{\mathcal{O}}$ are purely real, which cannot be deduced given the information thus far. An alternative approach is considered in [69]: the

dipole correlator is split into real and imaginary parts before evolution. Then there are two degrees of freedom, analogous to $\mathcal{G}$ and $G^{\mathcal{O}}$, with two separate equations from the start.

The next step in this calculation is to try to obtain more information about G^d, specifically G^d with *three distinct* coordinate indices. This can be done by considering the evolution equation for the 3-point correlator. Just as the evolution of the 2-point correlator required the 3-point correlator, so too does the evolution of the 3-point correlator require the 4-point correlator. This 4-point correlator is not like one of the elements of $\mathcal{A}(Y)$. Instead, it contains *two* gluons across the target line. To get this, one must consider a generic 6-point correlator and then look at the local limit in which two of the three dipoles becomes a gluon line. In pictures,

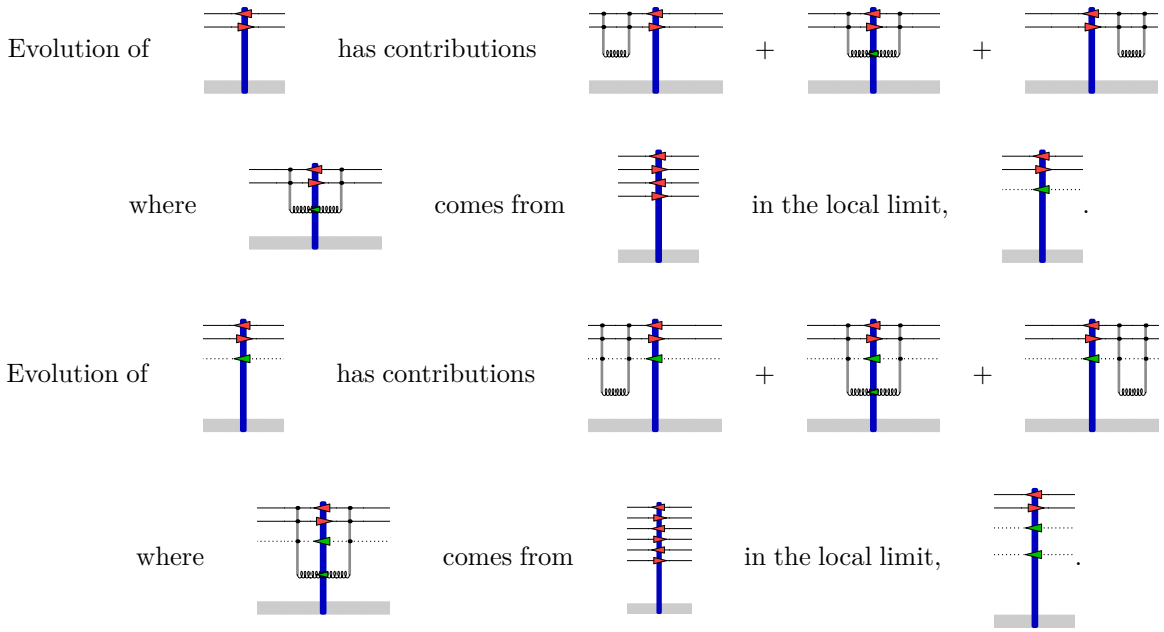

Now that the 6-point correlator has entered the picture, a full exposition of the new initial- and final-state bases and a new correlator matrix is required. An in-depth study of the 6-point correlator can lead to evolution equations for G^f and G^d with three different coordinate indices, unlike the 3-point functions $G^{\mathcal{O}}$ in this chapter, that have a repeated index.

Chapter 5

The 6-point Correlator

Introduction

This chapter consists of a technical discussion of the 6-point correlator, which is required to evaluate the evolution of the 3-point correlator, $\tilde{U}^{ab}_{\boldsymbol{z}}\mathrm{tr}(t^a U_{\boldsymbol{x}} t^b U^\dagger_{\boldsymbol{y}})/N_c$, as it appears in the Balitsky equation for the 2-point correlator $\mathrm{tr}(U_{\boldsymbol{x}}U^\dagger_{\boldsymbol{y}})/N_c$. The first section begins by setting up a basis of singlet states that can be constructed out of the three quarks and three antiquarks. There are six such non-equivalent basis states, which leads one to considering a 6×6 correlator matrix. The remainder of the chapter provides the results of differentiating each element of this new matrix according to Equation 4.33. These results will not be carried forward to the next chapter so the reader is welcome to skip ahead to Chapter 6.

5.1 The 6-point Correlator Matrix

Given three quarks and three antiquarks, the basis of singlets that can be formed consists of six elements. This is in agreement with [70], which provides a generic calculation for the number of orthogonal basis states required in SU(N_c) colour space, given some arbitrary number of partons. The normalised basis chosen in this chapter is

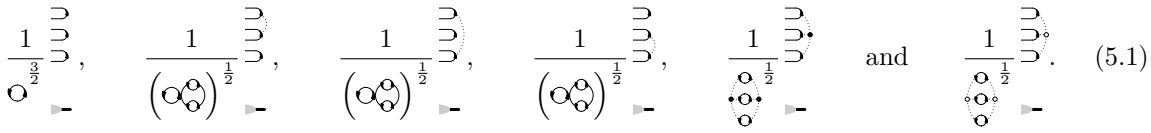

(5.1)

Since there are six states, there are 36 possible 6-point correlators. These can be written in a 6×6 matrix (analogous to $\mathcal{A}(Y)$ in the 4-point correlator case) that will be denoted $\mathcal{B}(Y)$. Instead of dealing with the full matrix, which may be cumbersome, $\mathcal{B}(Y)$ is split up into four smaller matrices,

$$\mathcal{B}(Y) = \begin{pmatrix} \mathcal{B}_1 & \mathcal{B}_2 \\ \mathcal{B}_3 & \mathcal{B}_4 \end{pmatrix} (Y). \tag{5.2}$$

The constituent matrices are defined as

$\mathcal{B}_1(Y) :=$

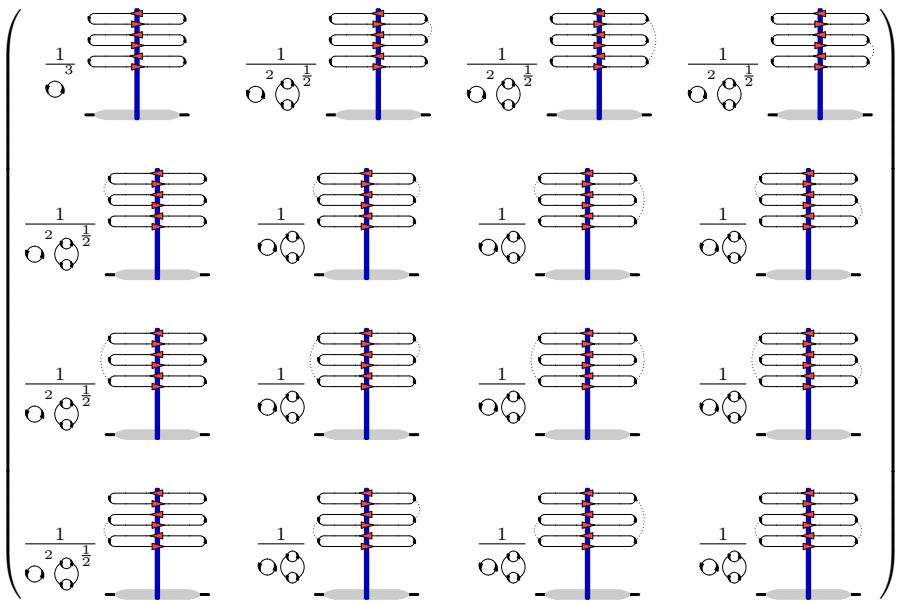

(5.3)

$$\mathcal{B}_2(Y) := \left(\right.$$

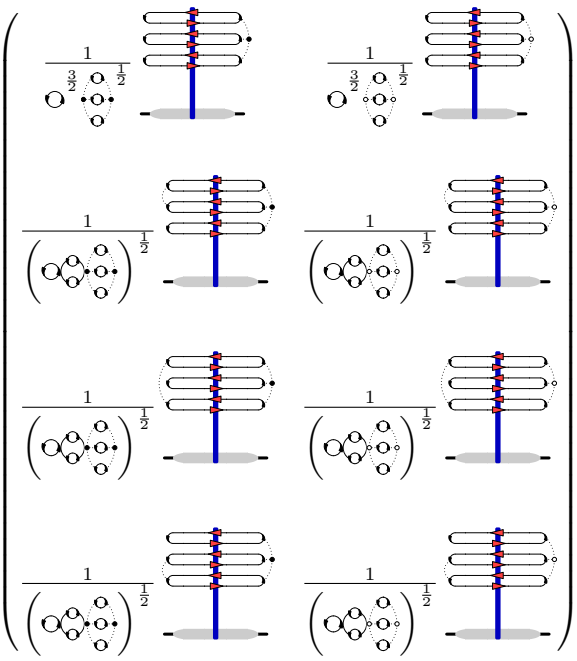

$$\left. \right) , \tag{5.4}$$

$$\mathcal{B}_3(Y) := \left(\right.$$

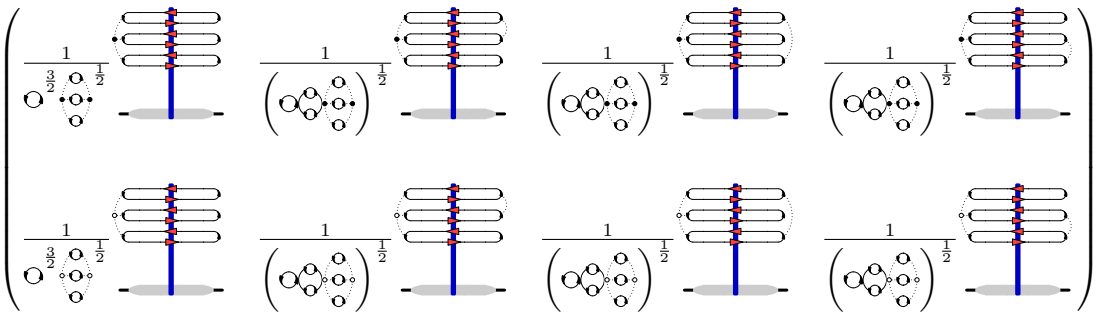

$$\left. \right) \tag{5.5}$$

and

$$\mathcal{B}_4(Y) := \left(\right.$$

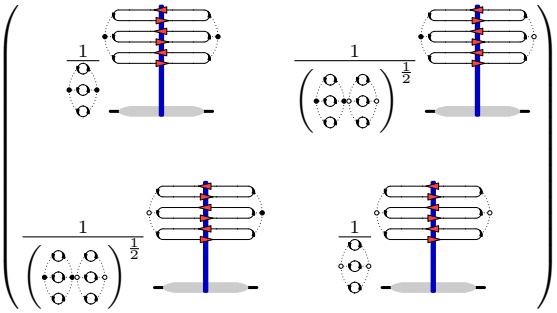

$$\left. \right) . \tag{5.6}$$

In terms of the mathematical expressions of the elements of the above matrices, $\mathcal{B}_2(Y)$ and $\mathcal{B}_3(Y)$ are transposes of each other. The designated splitting of the full $\mathcal{B}(Y)$ is chosen in this way so that only one of these off-diagonal constituent matrices need consideration.

As was done with the 4-point correlator matrix in Chapter 3, a differential equation

$$\frac{d}{dY}\mathcal{B}(Y) = -\mathcal{P}(Y)\mathcal{B}(Y) \tag{5.7}$$

is written from which the parametrisation equations for the matrix elements of $\mathcal{B}(Y)$ can be extracted. $\mathcal{P}(Y)$ is a symmetric matrix that is the 6-point correlator analogue of $\mathcal{M}(Y)$. It is composed of elements denoted p_{ij} according to

$$\mathcal{P}(Y) := \begin{pmatrix} p_{11} & p_{12} & p_{13} & p_{14} & p_{15} & p_{16} \\ p_{12} & p_{22} & p_{23} & p_{24} & p_{25} & p_{26} \\ p_{13} & p_{23} & p_{33} & p_{34} & p_{35} & p_{36} \\ p_{14} & p_{24} & p_{34} & p_{44} & p_{45} & p_{46} \\ p_{15} & p_{25} & p_{35} & p_{45} & p_{55} & p_{56} \\ p_{16} & p_{26} & p_{36} & p_{46} & p_{56} & p_{66} \end{pmatrix}. \tag{5.8}$$

This is also split into four smaller matrices, corresponding to $\mathcal{B}_i(Y)$ for $i = 1, 2, 3, 4$.

As an example of the parametrisation equations that can be obtained from Equation 5.7, consider the element

$$\frac{d}{dY}\left(\frac{1}{\text{O}\!\text{O}}\right.$$
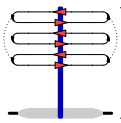
$$\left.\right) = \frac{1}{\text{O}\!\text{O}}$$
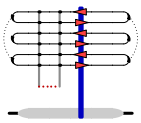
(5.9)

that appears on the lefthand side of the equation. A brief calculation will be done to explain exactly how the parametrisation equation for this correlator comes about. Executing matrix multiplication in Equation 5.7 for this element gives

$$\frac{1}{\text{O}\!\text{O}}$$
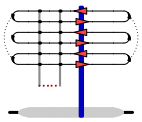
$$= -\left(p_{13}\frac{1}{\text{O}^2\text{O}^{\frac{1}{2}}}\right.$$
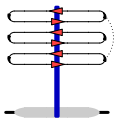
$$+ p_{23}\frac{1}{\text{O}\!\text{O}}$$
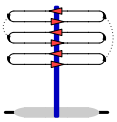
$$+ p_{33}\frac{1}{\text{O}\!\text{O}}$$
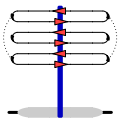
$$+ p_{34}\frac{1}{\text{O}\!\text{O}}$$
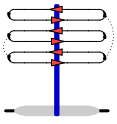
$$+ p_{35}\frac{1}{\left(\text{O}\!\text{O}\right)^{\frac{1}{2}}}$$
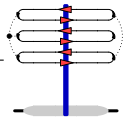
$$\left. + p_{36}\frac{1}{\left(\text{O}\!\text{O}\right)^{\frac{1}{2}}}\right)$$
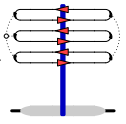
. (5.10)

On the other hand, inserting a complete set of states into the middle of the diagram on the righthand

side of Equation 5.9 gives

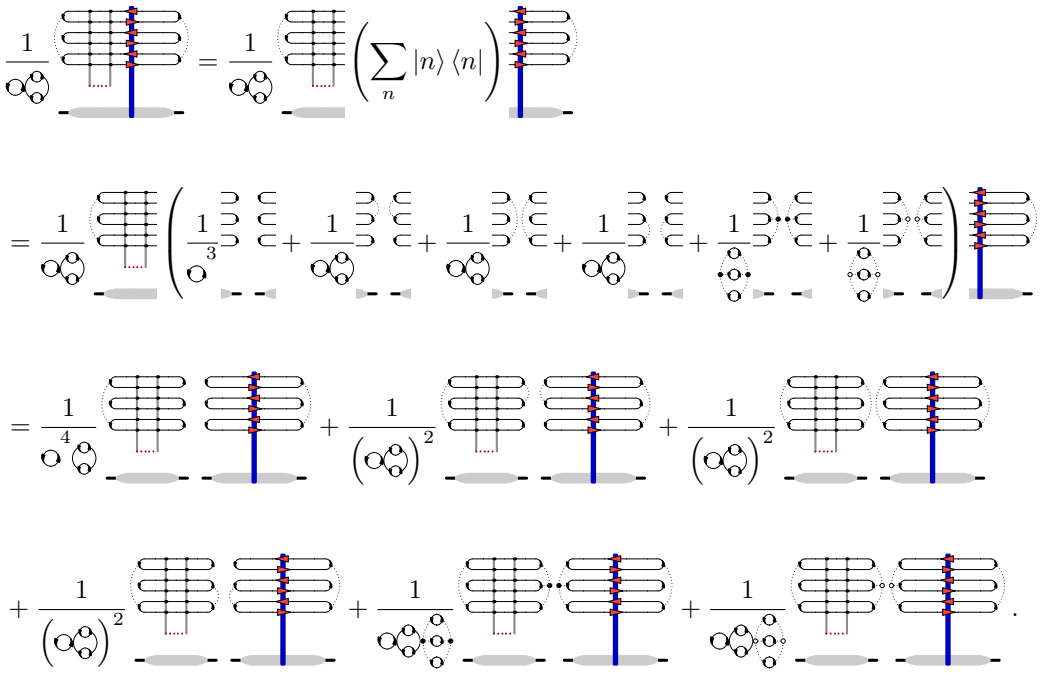

(5.11)

By matching coefficients of like diagrams in Equations 5.10 and 5.11, one finds the relations

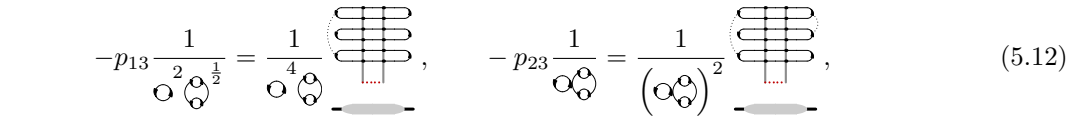

(5.12)

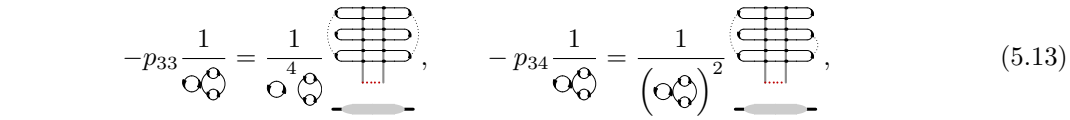

(5.13)

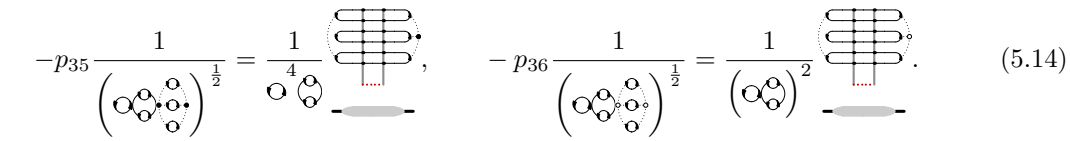

(5.14)

These equalities can be used to obtain the six elements of $\mathcal{P}(Y)$ that show up here. The newly determined p_{ij} can be inserted back into Equation 5.10, resulting in an explicit expression for 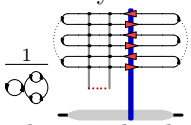 . All 36 elements of $\mathcal{B}(Y)$ can be obtained this way, although these calculations will not be done explicitly here, to save the reader the effort.

5.2 Differentiating the 6-point Correlator

In the previous section, the 6-point correlator matrix and a systematic method for obtaining parametrisations for its elements, was established. The 36 elements of $\mathcal{B}(Y)$ are ready to be differentiated. The differential operators introduced in the previous chapter, namely

$$\int d^2u\, d^2v\, d^2w\, f^{abc} G^f_{\boldsymbol{uvw}} i\bar{\nabla}^a_{\boldsymbol{u}} i\bar{\nabla}^b_{\boldsymbol{v}} i\bar{\nabla}^c_{\boldsymbol{w}} \qquad \text{and} \qquad \int d^2u\, d^2v\, d^2w\, d^{abc} G^d_{\boldsymbol{uvw}} i\bar{\nabla}^a_{\boldsymbol{u}} i\bar{\nabla}^b_{\boldsymbol{v}} i\bar{\nabla}^c_{\boldsymbol{w}},$$

will now be applied to $\mathcal{B}(Y)$ with the intention of extracting parametrisation equations for its elements. Recall that the ultimate goal of this chapter is to investigate the higher-order n-point functions that enter the parametrisation of the 3-point correlator, $\tilde{U}^{ab}_{\boldsymbol{z}} \mathrm{tr}(t^a U_{\boldsymbol{x}} t^b U^\dagger_{\boldsymbol{y}})/N_c$. A full discussion of the 6-point correlator will therefore be curtailed to suit these needs; only those elements of $\mathcal{B}(Y)$ that survive the coincidence limits that reduce the 6-point correlator to the 3-point correlator will be considered.

At the end of Chapter 4.1, it was mentioned that the object of interest is 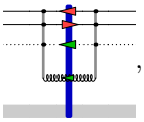 , which comes from the 6-point correlator

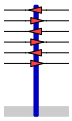
$= U_{\boldsymbol{x}} U^\dagger_{\boldsymbol{y}} U_{\boldsymbol{x}'} U^\dagger_{\boldsymbol{y}'} U_{\boldsymbol{x}''} U^\dagger_{\boldsymbol{y}''},$ (5.15)

in the limits that reduce it to 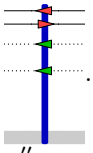 . Therefore, only the elements of $\mathcal{B}(Y)$ that are non-zero in the local limits $\boldsymbol{x}' \to y'$ and $\boldsymbol{x}'' \to y''$ are of interest.

5.2.1 The three-derivative operator $\hat{G}^{f3}$

Due to the complete antisymmetry of the 3-point function $G^f_{\boldsymbol{uvw}}$ in the differential operator $\hat{G}^{f3} = f^{abc} G^f_{\boldsymbol{uvw}} i\bar{\nabla}^a_{\boldsymbol{u}} i\bar{\nabla}^b_{\boldsymbol{v}} i\bar{\nabla}^c_{\boldsymbol{w}}$, some of the elements of $\mathcal{P}(Y)$ can be set to zero in the limits $\boldsymbol{x}' \to \boldsymbol{y}'$ and $\boldsymbol{x}'' \to \boldsymbol{y}''$ from the start. The second and third quark dipoles become gluon lines in the limits so any terms with a singlet projection state on these dipoles must vanish. In addition, any term with a projection state  on either side becomes zero as the d^{abc} from the state and the f^{abc} from $\hat{G}^{f3}$ cancel

each other.

This leaves the only potentially non-zero elements in $\mathcal{P}(Y)$, p_{44} and p_{45} and p_{55}. Evaluating these by applying the differential operator $\hat{G}^{f3}$ to 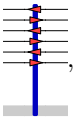 , projecting onto the relevant basis states and taking the two limits results in

$$\lim_{\substack{\boldsymbol{x}'\to\boldsymbol{y}'\\ \boldsymbol{x}''\to\boldsymbol{y}''}} p_{45} = -i\sqrt{\frac{9N_c^2}{2}}\quad G^f_{\boldsymbol{xyy}'} + G^f_{\boldsymbol{xyy}''} - G^f_{\boldsymbol{xy}'\boldsymbol{y}''} + G^f_{\boldsymbol{yy}'\boldsymbol{y}''}\Bigg) \tag{5.16}$$

and $p_{44} = p_{55} = 0$. The antisymmetry of the operator $\hat{G}^{f3}$ was very helpful in obtaining this simple result. The symmetric differential operator case will not be so trivial.

5.2.2 The three-derivative operator $\hat{G}^d$

Unlike the antisymmetric case, most of the elements of $\mathcal{P}(Y)$ survive being differentiated by the symmetric operator $\hat{G}^d = d^{abc}G^d_{\boldsymbol{uvw}}i\bar{\nabla}^a_{\boldsymbol{u}}i\bar{\nabla}^b_{\boldsymbol{v}}i\bar{\nabla}^c_{\boldsymbol{w}}$ where $G^d_{\boldsymbol{uvw}}$ is totally symmetric. There are 21 elements to be considered - 6 diagonal elements and 15 elements above the diagonal. The results for each are listed below. The linear combination introduced in Chapter 4, namely $G^{\mathcal{O}}_{\boldsymbol{xy}} = G^d_{\boldsymbol{xxy}} - G^d_{\boldsymbol{yyx}}$, makes an appearance.

Diagonal elements of $\mathcal{P}(Y)$

$$\lim_{\substack{\boldsymbol{x}'\to\boldsymbol{y}'\\ \boldsymbol{x}''\to\boldsymbol{y}''}} p_{11} = -\frac{iC_d d_A}{4N_c}\quad G^d_{\boldsymbol{xxx}} - G^d_{\boldsymbol{yyy}} - 3G^{\mathcal{O}}_{\boldsymbol{xy}}\Bigg) \tag{5.17}$$

$$\lim_{\substack{\boldsymbol{x}'\to\boldsymbol{y}'\\ \boldsymbol{x}''\to\boldsymbol{y}''}} p_{22} = -\frac{iC_d}{4N_c}\quad d_A\Big(G^d_{\boldsymbol{xxx}} - G^d_{\boldsymbol{yyy}}\Big) + 3\Big(G^{\mathcal{O}}_{\boldsymbol{xy}} - N_c^2 G^{\mathcal{O}}_{\boldsymbol{xy}'} + N_c^2 G^{\mathcal{O}}_{\boldsymbol{yy}'}\Big)\Bigg) \tag{5.18}$$

$$\lim_{\substack{\boldsymbol{x}'\to\boldsymbol{y}'\\ \boldsymbol{x}''\to\boldsymbol{y}''}} p_{33} = -\frac{iC_d}{4N_c}\quad d_A\Big(G^d_{\boldsymbol{xxx}} - G^d_{\boldsymbol{yyy}}\Big) + 3\Big(G^{\mathcal{O}}_{\boldsymbol{xy}} - N_c^2 G^{\mathcal{O}}_{\boldsymbol{xy}''} + N_c^2 G^{\mathcal{O}}_{\boldsymbol{yy}''}\Big)\Bigg) \tag{5.19}$$

$$\lim_{\substack{\boldsymbol{x}'\to\boldsymbol{y}'\\ \boldsymbol{x}''\to\boldsymbol{y}''}} p_{44} = -\frac{iC_d d_A}{4N_c}\left(G^d_{\boldsymbol{xxx}} - G^d_{\boldsymbol{yyy}} - 3G^{\mathcal{O}}_{\boldsymbol{xy}}\right) \tag{5.20}$$

$$\lim_{\substack{\boldsymbol{x}'\to\boldsymbol{y}'\\ \boldsymbol{x}''\to\boldsymbol{y}''}} p_{55} = -\frac{iC_d}{8N_c^2}\left(2d_A\Big(G^d_{\boldsymbol{xxx}} - G^d_{\boldsymbol{yyy}}\Big) + 6G^{\mathcal{O}}_{\boldsymbol{xy}} - N_c^2\Big(G^{\mathcal{O}}_{\boldsymbol{xy}'} + G^{\mathcal{O}}_{\boldsymbol{xy}''} - G^{\mathcal{O}}_{\boldsymbol{yy}'} - G^{\mathcal{O}}_{\boldsymbol{yy}''}\Big)\right) \tag{5.21}$$

$$\begin{aligned}\lim_{\substack{\boldsymbol{x}'\to\boldsymbol{y}'\\ \boldsymbol{x}''\to\boldsymbol{y}''}} p_{66} = &-\frac{i}{8N_c}\Bigg(2C_d d_A\Big(G^d_{\boldsymbol{xxx}} - G^d_{\boldsymbol{yyy}}\Big) + 48N_c\Big(G^d_{\boldsymbol{xy'y''}} - G^d_{\boldsymbol{yy'y''}}\Big) + 6N_c C_d G^{\mathcal{O}}_{\boldsymbol{xy}}\\ &- 3N_c^2 C_d\Big(G^d_{\boldsymbol{xxy'}} + G^d_{\boldsymbol{xxy''}} - G^d_{\boldsymbol{yyy'}} - G^d_{\boldsymbol{yyy''}}\Big)\\ &+ 3N_c(N_c^2-12)\Big(G^d_{\boldsymbol{xy'y'}} + G^d_{\boldsymbol{xy''y''}} - G^d_{\boldsymbol{yy'y'}} - G^d_{\boldsymbol{yy''y''}}\Big)\Bigg).\end{aligned} \tag{5.22}$$

Off-diagonal elements of $\mathcal{P}(Y)$

The off-diagonal elements of the first three rows of $\mathcal{P}(Y)$ are zero in the limits $\boldsymbol{x'}\to\boldsymbol{y'}$ and $\boldsymbol{x''}\to\boldsymbol{y''}$. The remaining three off-diagonal elements are given below, in terms of the linear combination $G^{\mathcal{O}3}_{\boldsymbol{xyz}} := G^d_{\boldsymbol{xxy}} - 2G^d_{\boldsymbol{xyz}} + G^d_{\boldsymbol{yzz}}$:

$$\lim_{\substack{\boldsymbol{x}'\to\boldsymbol{y}'\\ \boldsymbol{x}''\to\boldsymbol{y}''}} p_{45} = \frac{3iC_d}{\sqrt{8}}\left(G^{\mathcal{O}3}_{\boldsymbol{xy'y}} - G^{\mathcal{O}3}_{\boldsymbol{xy''y}}\right) \tag{5.23}$$

$$\lim_{\substack{\boldsymbol{x}'\to\boldsymbol{y}'\\ \boldsymbol{x}''\to\boldsymbol{y}''}} p_{46} = -i\sqrt{\frac{9N_cC_d}{32}}\left(G^{\mathcal{O}3}_{\boldsymbol{xy'y''}} - G^{\mathcal{O}3}_{\boldsymbol{y'yy''}}\right) \tag{5.24}$$

$$\begin{aligned}\lim_{\substack{\boldsymbol{x}'\to\boldsymbol{y}'\\ \boldsymbol{x}''\to\boldsymbol{y}''}} p_{56} = &\frac{3i}{16}\sqrt{\frac{C_d}{N_c}}\Bigg(N_cC_d\Big(G^d_{\boldsymbol{xxy'}} - G^d_{\boldsymbol{xxy''}} + G^d_{\boldsymbol{yyy'}} - G^d_{\boldsymbol{yyy''}}\Big) + 8\Big(G^d_{\boldsymbol{xyy'}} - G^d_{\boldsymbol{xyy''}}\Big)\\ &+ N_c^2\Big(-G^d_{\boldsymbol{xy'y'}} + G^d_{\boldsymbol{xy''y''}} - G^d_{\boldsymbol{yy'y'}} + G^d_{\boldsymbol{yy''y''}} + 2G^d_{\boldsymbol{y'y'y''}} - 2G^d_{\boldsymbol{y'y''y''}}\Big)\Bigg).\end{aligned} \tag{5.25}$$

In summary, the only element of $\mathcal{P}(Y)$ that survives differentiation by $\hat{G}^{f3}$ and the two limits is

p_{45}. For the $\hat{G}^d$ case, the non-trivial elements are

$$\begin{pmatrix} p_{11} & 0 & 0 & 0 & 0 & 0 \\ 0 & p_{22} & 0 & 0 & 0 & 0 \\ 0 & 0 & p_{33} & 0 & 0 & 0 \\ 0 & 0 & 0 & p_{44} & p_{45} & p_{46} \\ 0 & 0 & 0 & p_{45} & p_{55} & p_{56} \\ 0 & 0 & 0 & p_{46} & p_{56} & p_{66} \end{pmatrix}. \tag{5.26}$$

The second result is extremely convenient because it leads to the decoupling of three of the six coupled differential equations represented by Equation 5.7. A further discussion of the parametrisation equations from both the $\hat{G}^{f3}$ and $\hat{G}^d$ cases will be discussed below.

5.3 Parametrisation Equations

The only parametrisation equations of interest in this investigation are those of correlators that will contribute to the evolution of the 3-point correlator 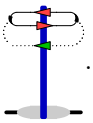 . At leading order, the evolution of this correlator looks like

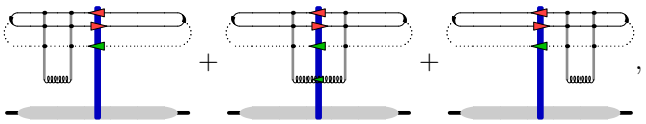

, (5.27)

as already discussed at the end of Chapter 4. The second diagram in this expression is the one that has contributions from the 6-point correlator in the limits $\boldsymbol{x}' \to \boldsymbol{y}'$ and $\boldsymbol{x}'' \to \boldsymbol{y}''$.

In considering the diagram 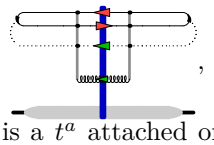 , one notices that only diagrams from the 6-point correlator matrix in which there is a t^a attached on both the left and the right of the first dipole, can survive. In other words, there must be a gluon line attached on both sides to the dipole that survives the coincidence limits.

By looking at correlator matrix $\mathcal{B}(Y)$, one can see that applying this reasoning results in only three

contributing elements:

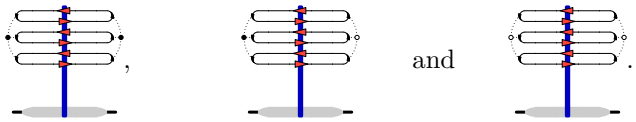

(5.28)

In the limits $\boldsymbol{x}' \to \boldsymbol{y}'$ and $\boldsymbol{x}'' \to \boldsymbol{y}''$, these become

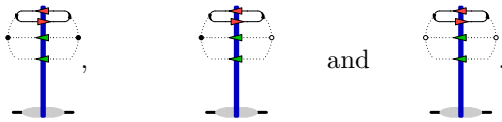

(5.29)

Instead of calculating 36 parametrisation equations, only three need to calculated, one for each of these diagrams. Furthermore, the $\hat{G}^{f3}$ parametrisations can be ignored because the only non-zero result in that case corresponds to the diagram 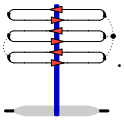 .

In the $\hat{G}^{d}$ case, the first three rows of the 6×6 matrix $\mathcal{P}(Y)$ in Equation 5.26 decouple, so these can be considered separately from the remaining non-trivial piece of the matrix, namely

$$\begin{pmatrix} p_{44} & p_{45} & p_{55} \\ p_{45} & p_{55} & p_{56} \\ p_{46} & p_{56} & p_{66} \end{pmatrix}. \tag{5.30}$$

Using this reduced matrix and applying Equation 5.7 yields three parametrisation equations for the three correlators from expression 5.29:

$$\frac{d}{dY}$$ 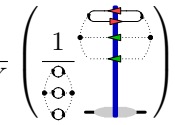 $$= p_{45}$$ 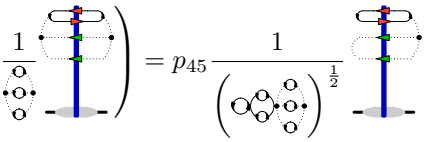 $$+ p_{55}$$ 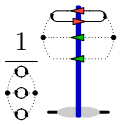 $$+ p_{56}$$ 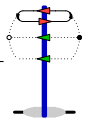 (5.31)

$$\frac{d}{dY}$$ 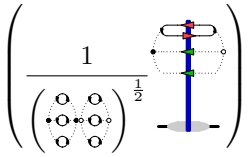 $$= p_{46}$$ 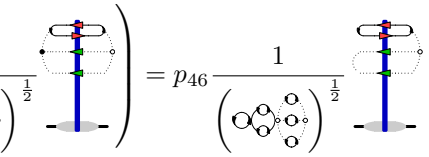 $$+ p_{56}$$ 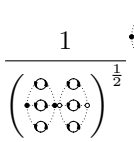 $$+ p_{66}$$ 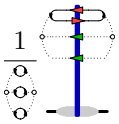 (5.32)

$$\frac{d}{dY}$$ 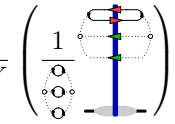 $$= p_{46}$$ 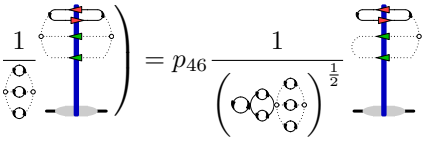 $$+ p_{56}$$ 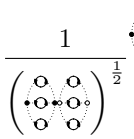 $$+ p_{66}$$ 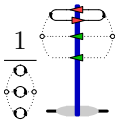 . (5.33)

The elements of $\mathcal{P}(Y)$ that appear in these equations can be substituted from the expressions given in the previous section. The righthand side of all three of these parametrisation equations are expected to contribute to 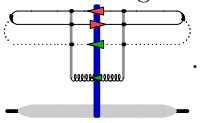 .

On this level, there is nothing more that can be done easily to simplify the result. One can attempt to diagonalise the matrix

$$\begin{pmatrix} p_{44} & p_{45} & p_{55} \\ p_{45} & p_{55} & p_{56} \\ p_{46} & p_{56} & p_{66} \end{pmatrix} \tag{5.34}$$

but the eigenvalues will be long, cumbersome expressions in terms of G^d. Success in this regard would lead to the three parametrisation equations decoupling. Then each can be solved independently and the correlators 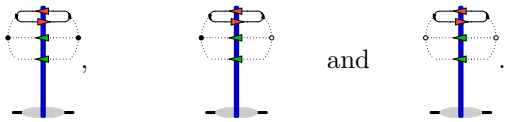
can be reparametrised in terms of G^d explicitly. This exercise is beyond the scope of this thesis but could lead to interesting results in future studies. The reader may be interested in consulting [74], in which the 6-point correlator has been explored in the large N_c limit.

Chapter 6

Exclusive J/Ψ Production Cross-section

The ultimate goal of this thesis is to determine all components of the cross-section calculation for exclusive J/Ψ vector-meson production in a nuclear collision. The foundational concepts of a generic cross-section calculation were covered in Section 1.2.2, in which it was shown that the square of the scattering amplitude needs to be determined to calculate a cross-section. Then in Section 2.2.2, the cross-section for deep inelastic scattering was discussed. The result consisted of two independent pieces, one containing the wave-function of the virtual photon that splits into the quark dipole and one containing information about the dipole interaction with the background field. Equation 2.20 is quoted here for convenience:

$$\sigma_{\mathrm{DIS}}(x_{\mathrm{Bj}}, Q^2) = 2 \int d^2\boldsymbol{r} \int_0^1 d\alpha \Big|\psi(\alpha, \boldsymbol{r}^2, Q^2)\Big|^2 \int d^2\boldsymbol{b}\, \hat{N}_{Y,\boldsymbol{xy}}$$

where $\hat{N}_{Y,\boldsymbol{xy}} := \left\langle \frac{\mathrm{tr}(1 - U_{\boldsymbol{x}} U_{\boldsymbol{y}}^\dagger)}{N_c} \right\rangle$ is the dipole operator.

In Chapter 3, the 4-point correlator in the GT was motivated by the claim that the term

$$\left\langle \frac{\mathrm{tr}(U_{\boldsymbol{y}'} U_{\boldsymbol{x}'}^\dagger)}{N_c} \frac{\mathrm{tr}(U_{\boldsymbol{x}} U_{\boldsymbol{y}}^\dagger)}{N_c} \right\rangle_Y$$

enters the cross-section calculation for vector-meson production. The origin of this expression will be

shown in Section 6.1, which follows the discussion from [2]. This will be followed by an exposition of the wave-function part of Equation 2.20, $\int d^2\boldsymbol{r} \int_0^1 d\alpha \left|\psi(\alpha, \boldsymbol{r}^2, Q^2)\right|^2$, which requires knowledge of the final state under consideration in a specific calculation.

6.1 Dipole Interaction Piece in the Cross-section

The quark dipole part of the total cross-section comes from the square of the difference between an interacting state and a non-interacting state,

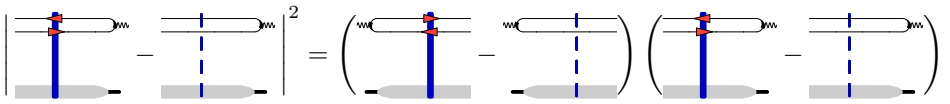

(6.1)

which can be expanded into four terms

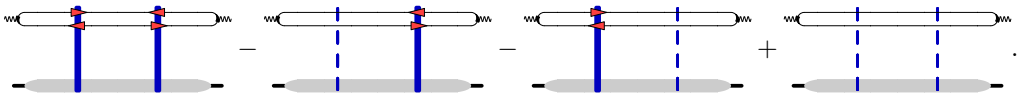

(6.2)

In terms of traces, this sum is

$$\left\langle \frac{\mathrm{tr}(U_{\boldsymbol{y}} U_{\boldsymbol{x}}^\dagger U_{\boldsymbol{x}} U_{\boldsymbol{y}}^\dagger)}{N_c} \right\rangle_Y - \left\langle \frac{\mathrm{tr}(U_{\boldsymbol{x}} U_{\boldsymbol{y}}^\dagger)}{N_c} \right\rangle_Y - \left\langle \frac{\mathrm{tr}(U_{\boldsymbol{y}} U_{\boldsymbol{x}}^\dagger)}{N_c} \right\rangle_Y + \left\langle \frac{\mathrm{tr}\mathbb{1}}{N_c} \right\rangle_Y . \tag{6.3}$$

Using the unitarity of U, the first term reduces to $\mathrm{tr}\mathbb{1}$. Then all that remains is the middle two terms, which encode all information about the non-trivial interaction of the dipole and target. Assuming these averages are real, these middle terms can be written as

$$-\left\langle \frac{\mathrm{tr}(U_{\boldsymbol{x}} U_{\boldsymbol{y}}^\dagger)}{N_c} \right\rangle_Y - \left\langle \frac{\mathrm{tr}(U_{\boldsymbol{y}} U_{\boldsymbol{x}}^\dagger)}{N_c} \right\rangle_Y = -2\left\langle \frac{\mathrm{tr}(U_{\boldsymbol{x}} U_{\boldsymbol{y}}^\dagger)}{N_c} \right\rangle_Y \tag{6.4}$$

so that expression 6.5 becomes

$$2\left\langle \frac{\mathrm{tr}\mathbb{1}}{N_c} \right\rangle_Y - 2\left\langle \frac{\mathrm{tr}(U_{\boldsymbol{x}} U_{\boldsymbol{y}}^\dagger)}{N_c} \right\rangle_Y = 2\left\langle \frac{\mathrm{tr}(\mathbb{1} - U_{\boldsymbol{x}} U_{\boldsymbol{y}}^\dagger)}{N_c} \right\rangle_Y = 2\hat{N}_{Y,\boldsymbol{xy}} \tag{6.5}$$

as appears in the σ_{DIS}.

Vector-meson production

This expression pertains to the total cross-section but only requires a small modification if the cross-section under scrutiny is that of inclusive or exclusive vector-meson production. In that case, the final

state of the quark dipole, once it has interacted with the target field, becomes a quark bound state that is the vector-meson.

Diagrammatically, the righthand side of Equation 6.1 is modified to

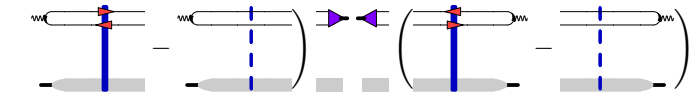

(6.6)

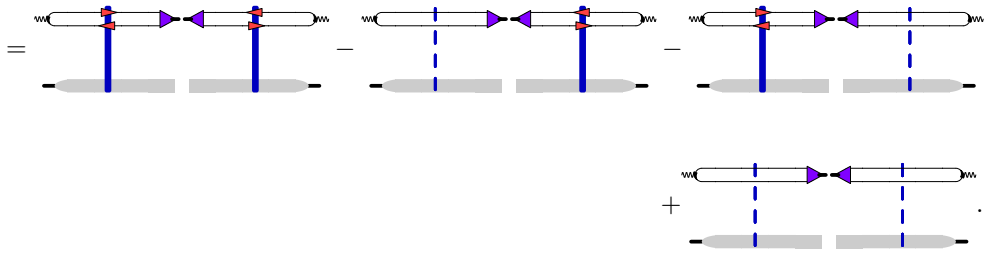

(6.7)

where the final state projection  must include all quantum numbers pertaining to the vector-meson of interest. Since the left and right bracketed factors in line 6.6 are now separated by the vector-meson final states in the middle, the Wilson lines in the two factors will no longer have the same transverse coordinates (as they do in the total cross-section case given in Equation 6.1). From the expanded expression in line 6.7, it can be seen that this only affects the first term, which contains Wilson lines to the left and the right of the final states. Instead of simplifying to a trace over the identity matrix, this term remains a non-trivial contribution,

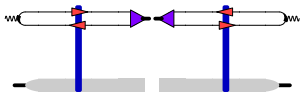

$$= \left\langle \frac{\mathrm{tr}(U_{\boldsymbol{y}'} U^{\dagger}_{\boldsymbol{x}'})}{N_c} \frac{\mathrm{tr}(U_{\boldsymbol{x}} U^{\dagger}_{\boldsymbol{y}})}{N_c} \right\rangle_Y .$$

6.2 Wave-functions in the Cross-section

In Section 2.2.2, the only wave-function that was relevant for the cross-section was that of the virtual photon projectile $\psi(\alpha, \boldsymbol{r}, Q^2)$, which appeared in the final state as well. Now that the final state projection is a vector-meson, its wave-function must also appear in the cross-section. This enters via the photon - vector-meson wave-function overlap $\big(\gamma|V\big) = \big(\gamma|V\big)(\alpha, \boldsymbol{r}, Q^2)$, where γ and V denote the photon and vector-meson, respectively. Since the wave-functions can be either transversely (T) or longitudinally (L) polarised, two separate wave-function overlaps must be considered, $(\gamma|V)_T$ and $(\gamma|V)_L$.

The linear combination of target averages given in Equation 6.7 can now be combined with these wave-function overlaps to write the overall expression for the cross-section of vector-meson production. This is given as a differential cross-section

$$\begin{aligned}\frac{d\sigma_{T,L}}{dt} =& \frac{1}{4\pi}\int_0^1 d\alpha\, d\alpha' \int d^2x\, d^2x'\, d^2y\, d^2y' e^{-i\boldsymbol{q}\cdot\left[\left(\alpha\boldsymbol{x}+(1-\alpha)\boldsymbol{y}\right)-\left(\alpha'\boldsymbol{x}'+(1-\alpha')\boldsymbol{y}'\right)\right]} \\ &\times \left(\gamma|V\right)^*_{T,L}(\alpha', \boldsymbol{x}'-\boldsymbol{y}', Q^2)\left(\gamma|V\right)_{T,L}(\alpha, \boldsymbol{x}-\boldsymbol{y}, Q^2) \\ &\times \left(\left\langle \frac{\mathrm{tr}(U_{\boldsymbol{y}'}U^\dagger_{\boldsymbol{x}'})}{N_c}\frac{\mathrm{tr}(U_{\boldsymbol{x}}U^\dagger_{\boldsymbol{y}})}{N_c}\right\rangle_Y - \left\langle \frac{\mathrm{tr}(U_{\boldsymbol{x}}U^\dagger_{\boldsymbol{y}})}{N_c}\right\rangle_Y - \left\langle \frac{\mathrm{tr}(U_{\boldsymbol{y}'}U^\dagger_{\boldsymbol{x}'})}{N_c}\right\rangle_Y + 1\right)\end{aligned} \tag{6.8}$$

where $t := -\boldsymbol{q}^2$ is the square of the transverse momentum transfer [71]. The quark dipole size $\boldsymbol{r}$ has been written in terms of $\boldsymbol{x}$ and $\boldsymbol{y}$ in this expression because these coordinates appear explicitly in the argument of the exponentials.

J/Ψ wave-function

The only thing left undetermined in this expression is the wave-function overlap. The transversely and longitudinally polarised wave-function overlaps are given in terms of the photon wave-function ψ_γ and the vector-meson wave-function ψ_V as

$$(\gamma|V)_T := \frac{1}{2}\sum_{h\bar{h}}\left((\psi^*_\gamma)^{h\bar{h}}_{+1}(\psi_V)^{h\bar{h}}_{+1} + (\psi^*_\gamma)^{h\bar{h}}_{-1}(\psi_V)^{h\bar{h}}_{-1}\right) \tag{6.9}$$

$$(\gamma|V)_L := \sum_{h\bar{h}}(\psi^*_\gamma)^{h\bar{h}}_{0}(\psi_V)^{h\bar{h}}_{0} \tag{6.10}$$

where h and $\bar{h}$ denote the helicities of the quark and antiquark, respectively, (they are either "+" or "−") and the subscripts $-1, 0, +1$ refer to polarisation states. The discussion in this section follows [72], which can be consulted for more detail about the origin of the expressions quoted below.

Whereas the photon wave-function is calculated from field theory, the vector-meson wave-function depends on phenomenological models to describe it. For a longitudinally polarised vector-meson, the wave-function can be expressed in momentum (k) space as

$$(\tilde{\psi}_V)_0^{h\bar{h}}(k,\alpha) = \frac{1}{\sqrt{2}}(\delta_{h+\,\bar{h}-} + \delta_{h-\,\bar{h}+})\tilde{\phi}_L(k,\alpha) \tag{6.11}$$

where $\tilde{\phi}_L(k,\alpha)$ is a new function that requires modelling. Similarly, the two transversely polarised vector-meson wave-functions can be written as

$$(\tilde{\psi}_V)_{+1}^{h\bar{h}}(k,\alpha) = \left[+ \frac{k}{m_f} e^{+i\varphi_k} \Big(\alpha\delta_{h+\,\bar{h}-} - (1-\alpha)\delta_{h-\,\bar{h}+} \Big) + \delta_{h+\,\bar{h}+} \right] \tilde{\phi}_T(k,\alpha) \tag{6.12}$$

$$(\tilde{\psi}_V)_{-1}^{h\bar{h}}(k,\alpha) = \left[- \frac{k}{m_f} e^{-i\varphi_k} \Big((1-\alpha)\delta_{h+\,\bar{h}-} - \alpha\delta_{h-\,\bar{h}+} \Big) + \delta_{h-\,\bar{h}-} \right] \tilde{\phi}_T(k,\alpha) \tag{6.13}$$

where m_f is the quark mass. A Fourier transform can be applied to these expressions to get from k-space to r-space if need be.

To give an idea of what kind of functions $\tilde{\phi}_{L,T}(k,\alpha)$ are, the expressions used in one of the more popular models, called the *light-cone Gaussian model*, are quoted:

$$\phi_L = N_L \exp\left\{ \frac{-r^2}{2R_L^2} \right\} \tag{6.14}$$

$$\phi_T = N_T\, \alpha(1-\alpha) \exp\left\{ \frac{-r^2}{2R_L^2} \right\}. \tag{6.15}$$

Here, $N_{L,T}$ and $R_{L,T}$ are parameters to be determined in the modelling procedure. Once these functions are specified by the model, they can be used to write explicit expressions for the vector-meson wave-functions that enter the cross-section.

Part I Summary

The purpose of Part I was to find an expression for the cross-section of exclusive J/Ψ production within the context of the CGC framework. In this final chapter, it has been shown that this expression requires input from the 4-point correlator $\left\langle \frac{\mathrm{tr}(U_{\boldsymbol{y}'}U^{\dagger}_{\boldsymbol{x}'})}{N_c}\frac{\mathrm{tr}(U_{\boldsymbol{x}}U^{\dagger}_{\boldsymbol{y}})}{N_c}\right\rangle_Y$. In [2], the evolution of such correlators is shown to be described by JIMWLK evolution, just as with 2-point correlators. Given Equation 6.8, the goal of the first part of this thesis is complete.

In the investigation of the 3-point functions $G^f_{\boldsymbol{uvw}}$ and $G^d_{\boldsymbol{uvw}}$, it was shown that the antisymmetric function $G^f_{\boldsymbol{uvw}}$ does not enter the parametrisation equation for the 3-point correlator at all. The symmetric function $G^d_{\boldsymbol{uvw}}$ makes an appearance, but only in a restricted form in which two of the three coordinate indices are repeated. This is the result of taking the appropriate coincidence limits on the 4-point correlators in matrix $\mathcal{A}(Y)$, so as to obtain the 3-point correlator being studied. Since the only way that the 3-point functions enter the parametrisation equations is via $G^{\mathcal{O}}$, the evolution equation for the full $G^d_{\boldsymbol{uvw}}$ could not be determined. The 6-point correlator is required for such an investigation but this discussion was shown to grow cumbersome quickly (see Chapter 5).

Besides $G^d_{\boldsymbol{uvw}}$, $G^f_{\boldsymbol{uvw}}$ has proven even more elusive. In Chapter 4, it was seen that this antisymmetric 3-point function enters the parametrisation equations as off-diagonal transition elements that play the role of mixing contributions to a correlator. Unfortunately, these off-diagonal contributions vanished in the coincidence limits that turned the 4-point correlator to the 3-point correlator of interest and so the true role of $G^f_{\boldsymbol{uvw}}$ remains unknown. The full 6-point correlator matrix (not in any local limits) needs to be evaluated to obtain an evolution equation for $G^f_{\boldsymbol{uvw}}$ so that its behaviour may be better understood.

Part II, which will now follow, picks up on the cross-section discussion from the experimental perspective. The work done in this second part of the thesis aims to discuss the experimental steps required for a determination of the cross-section for exclusive J/Ψ production at the LHC. This will take the form of a feasibility study using a Monte Carlo event generator within the framework of the ATLAS detector.

Part II:

Experiment

Chapter 7

The ATLAS Detector

The purpose of this chapter is to provide the necessary detail about the experimental context in which Chapter 8 lies. CERN, the LHC and ATLAS have been introduced briefly in Chapter 1. Much of the technical details provided here about the LHC and the ATLAS detector come from [32] and [75]. The chapter begins with a brief description of the accelerator complex that provides the particle beams for the LHC and the major components of the collider itself. Section 7.2 is a basic overall description of the ATLAS detector, with emphasis placed on the components required for muon detection. The section following that provides a discussion of muon reconstruction techniques implemented by ATLAS. Finally, the chapter is concluded with a section dedicated to Monte Carlo techniques, as an appetiser for the STARlight generator discussed in Chapter 8.

7.1 The LHC Machine

7.1.1 Accelerator complex

Figure 7.1 provides a schematic of the entire LHC complex, with pink arrows denoting the path of protons and purple arrows the path of heavy ions. These particles begin their journey at one of two linear accelerators, Linac 2 for protons and Linac 3 for lead ions. The proton source is a *duoplasmatron*, which is essentially a cathode filament in a gas chamber. The lead ions originate from an *electron cyclotron resonance* ion source, which is a multipole magnet inside a solenoid magnet. From here, the proton bunches enter the Proton Synchrotron (PS) Booster at 50 MeV and the lead bunches the Low Energy Ion Ring (LEIR) at 4.2 MeV. The PS Booster and the LEIR accelerate the particles to 1.4 GeV and 72 MeV, respectively, for injection into the PS. They allow for more particles to enter the PS than if injected straight from the linacs. From the PS, the particles enter the Super Proton Synchrotron (SPS), which is capable of accelerating 4×10^{13} protons per cycle at up to 450 GeV. Finally, the SPS injects the particles into the LHC in two separate beam pipes, directing the beams in opposite directions to each other. These pipes have interaction points at various designated positions around the ring. The final proton beams have design parameters of 2808 bunches with approximately 10^{11} particles per bunch and a bunch spacing of 25 ns (corresponding to a frequency of 40 MHz). During 2011 and 2012 runs, the true operational bunch spacing was 50 ns, corresponding to a frequency of only 20 MHz.

Protons versus HI

While the general mechanism required for proton and lead beams is more or less the same, there are some technical differences that must be accounted for. The two types of beams are the same geometrical size but the proton beams have larger bunch spacings. There are two major disadvantages in HI beams at the LHC. The first is the low luminosity and the second is the beam lifetime. The luminosity issue is due to the large cross-section for nuclear electromagnetic interactions in peripheral (long-range) collisions, which is approximately 507 b. In such processes, the charge state or mass of the ions in one of the colliding beams is changed and a secondary beam exits the collision point. On

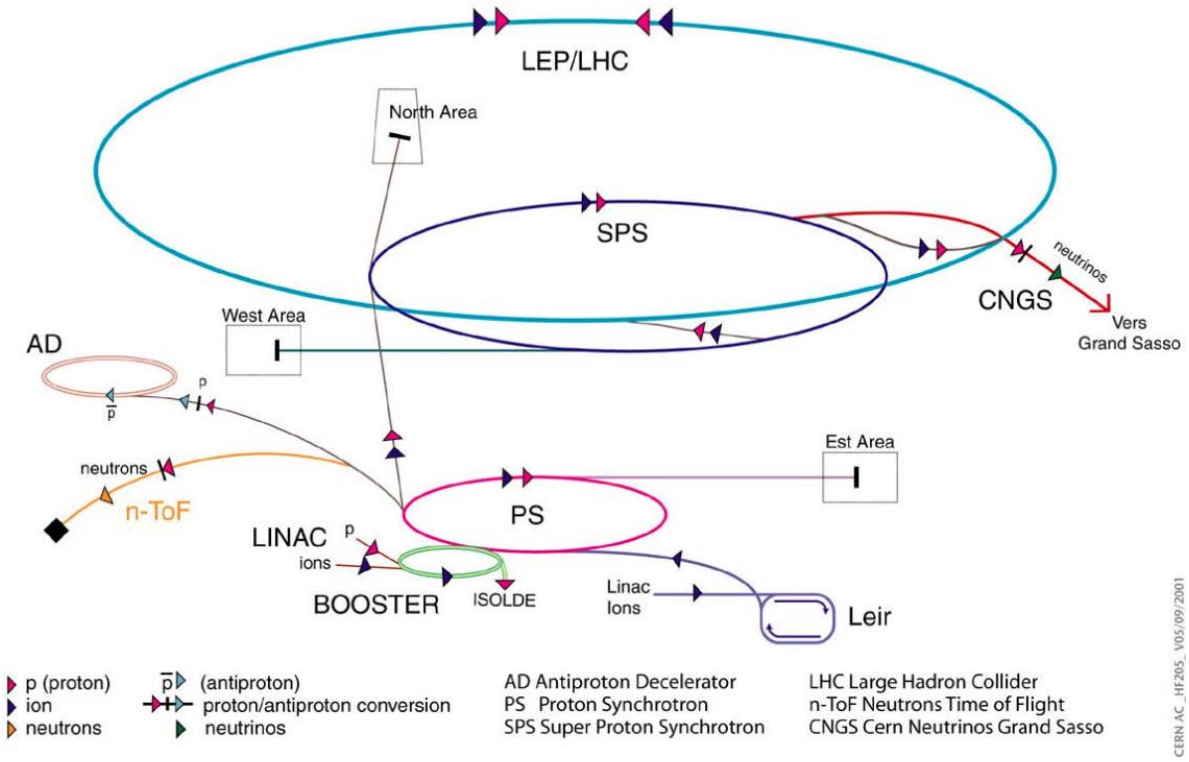

Figure 7.1: A schematic showing the layout of the the LHC accelerator complex [78].

the other hand, hadronic nuclear interactions of the kind

$$^{208}\mathrm{Pb}^{82+} +^{208}\mathrm{Pb}^{82+} \overset{\text{nuclear}}{\longrightarrow} X$$

have cross-sections around a mere 8 b. Other more minor causes are multiple Coulomb scattering, synchrotron radiation (which both occur in the proton case as well) and intra-beam scattering that diffuses the beam.

7.1.2 The LHC ring

The schematic layout of the LHC is shown in Figure 7.2. The tunnel consists of eight 528 m long straight sections and eight 106.9 m long arcs. The arcs are made of half cells that constitute the main bending and focusing parts of the ring; they contain 1104 of the 1232 main 16.5 m long dipoles in the LHC ring. Each half cell consists of a cryostat, a short straight section assembly and three dipole

magnets.

The schematic layout is divided into eight sectors, demarcated Octants 1 - 8 and governed by the arcs between two consecutive straight sections. Each octant has an Interaction Region (IR) with an Interaction Point (IP) at which the two beam pipes cross. Four of the eight IPs are used for collisions and are therefore the locations of the four major detectors at the LHC: ATLAS, ALICE, CMS and LHCb, located at IP 1, 2, 5 and 8, respectively. Proton collisions occur at all four points but HI collisions occur at IP 1, 2 and 5 only.

The SPS injects particles into Rings 1 and 2 in IR 2 and 8, respectively. The 2.5 km long transfer tunnels carrying the injection lines consist of dipole magnets that lie below and outside the LHC. The remaining four IRs, which do not contain detectors, have other necessary systems for LHC operation. IR 3 and IR 7 contain the beam cleaning systems. Particles with a large momentum offset and betatron amplitude are scattered by these systems, thus cleaning the beam. The Radio Frequency (RF) system as well as other LHC instrumentation is located at IR 4. It is a superconducting cavity system that captures, accelerates, stores and corrects the injected beam from IP 2 and 8. The beam dump, at which the beams exit the LHC, occurs in IR 6. It is carried out by a beam abort system constituted of magnets, that deflects the beams both horizontally and vertically. The beams are deflected to a carbon core absorber which dilutes the beam energy such that the absorber material (that has a high melting point and good thermal shock) does not overheat.

Dipole magnets

The beam pipes and their surrounding subsystems are complex, technical mechanisms that require almost perfect operation to ensure that the beams being collided within the various detectors around the LHC, are of a satisfactory standard. Figure 7.3 is included to provide some idea of these various components. It shows a cross-sectional view of one of the main dipole magnets that constitute the LHC ring.

The LHC tunnel arcs are only 3.7 m in internal diameter - a remnant from the LEP days. Due to this space restriction, a novel magnet design was required during the tunnel upgrade for the LHC. A cost-effective twin bore superconducting magnet design was used, that allows space for both the

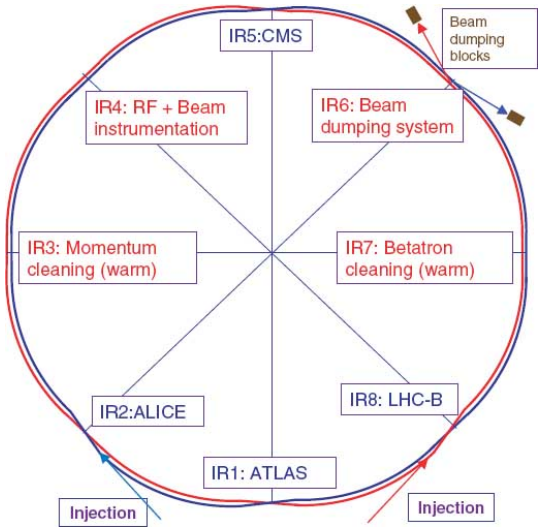

Figure 7.2: Schematic layout of the LHC machine [77].

beam rings in one tunnel. The magnets consist of two sets of coils and beam channels that share the same mechanical structure, cold mass and cryostat, but with magnetic fluxes circulating in opposite directions for the two channels. The main arcs therefore contain separate magnetic fields and vacuum chambers. All these magnetic components are submerged in a 1.3 bar helium superfluid bath at 1.9 K to facilitate superconductivity. At the crossing points where the detectors are located, the rings join and share a single beam pipe approximately 130 m long. Besides these extreme temperatures and strong magnetic fields, another extremity required is the vacuum in the beam pipe, which is on the order of 10^{-11} mbar.

In addition to the advanced accelerator physics that has gone into the LHC design, some extraordinary engineering feats, such as the superconducting dipole magnets, have been necessary to satisfy the ultimate experimental requirements of the collider.

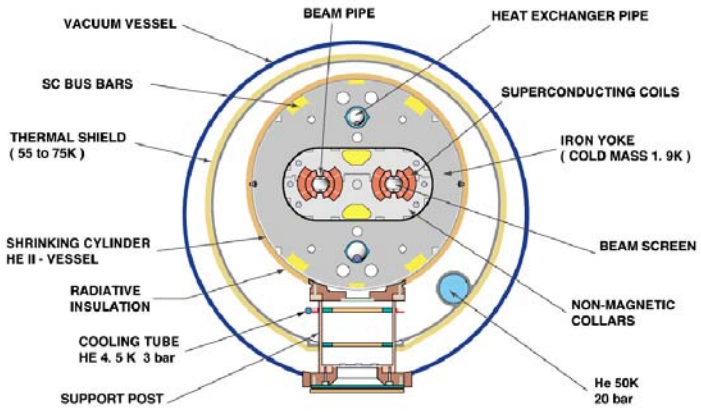

Figure 7.3: Cross-sectional view of an LHC dipole magnet [78].

7.2 The Detector

The ATLAS detector, located at IP 1, is a general-purpose detector capable of operating during all types of collisions at the LHC - p-p, p-Pb and Pb-Pb. Since two of the major goals at the LHC are the discovery of the Higgs boson and testing theories beyond the Standard Model, ATLAS has been designed to optimise performance for a variety of particle production and decay mechanisms. At the time of design, the mass of the Higgs boson was not well constrained and so the detector was built to cover a large mass range, spanning 100 GeV to several TeV. This feature has also left room for the possibility of new physics signatures, such as supersymmetric particles and their decay chains (as predicted by supersymmetric theories) and gravitons in the TeV region (as predicted by extra-dimensional theories).

From inside-out, ATLAS consists of several layers: a tracking chamber, EM calorimeter, hadronic calorimeter and muon spectrometer. The muon spectrometer is a key component and defines the overall dimensions of the detector - 25 m in height, 44 m in length and approximately 7000 tonnes in mass. These dimensions as well as the major detector components are illustrated in Figure 7.4. The rest of the design is governed by the magnet configuration. It consists of two parts: a thin superconducting solenoid that surrounds the inner cavity and three large, air-core superconducting toroids, consisting of one barrel and two end-caps. The solenoid is 5.3 m long and 2.5 m in diameter. It immerses the inner cavity in a 2 T field. The three toroids are arranged with an eight-fold symmetry around the calorimeters - each toroid consists of eight racetrack-like coils assembled radially and symmetrically

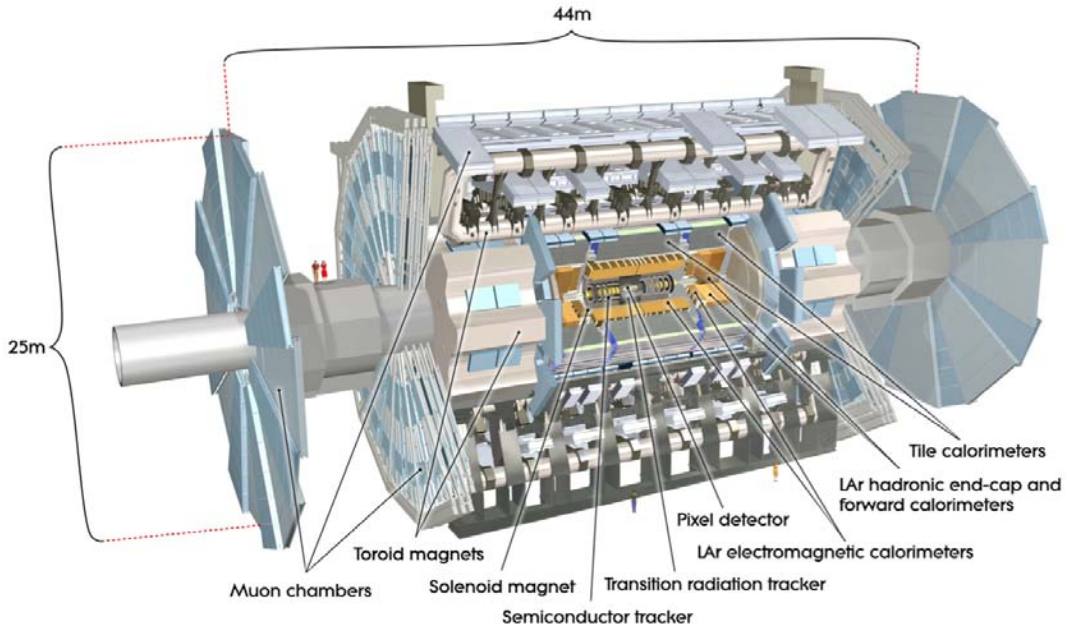

Figure 7.4: Cut-away view of the ATLAS detector.

around the beam axis.

ATLAS is forward-backward symmetric with respect to the interaction point, located in the centre of the detector along the beam line. The coordinate system defined about the detector places the origin at this nominal interaction point, the z-axis along the beam line, the positive x-axis directed towards the centre of the LHC and the positive y-axis directed upwards. The detector is further split into side-A and side-C, the positive and negative z-regions, respectively.

A more convenient coordinate system for physics analyses utilises two angles: the azimuthal angle, ϕ, defined around the beam axis and the polar angle, θ, defined as the angle from the beam axis. In addition, it is useful to define pseudorapidity $\eta := -\ln\tan\frac{\theta}{2}$, as well as transverse quantities in the $x-y$-plane, such as momentum p_T and energy E_T. These are used to write the four-momentum of a particle in the detector as $p^\mu = (E_T, p_T, \eta, \phi)$. A particle's four-momentum can be reconstructed by an appropriate algorithm using the signatures from various parts of the detector. In order to be able to infer what kind of particle has left these signatures, it is necessary to understand the many detector components and their detecting mechanisms. Particular attention will be paid to the muon spectrometer, since the analysis to come will consider the dimuon decay channel of J/Ψ vector-mesons.

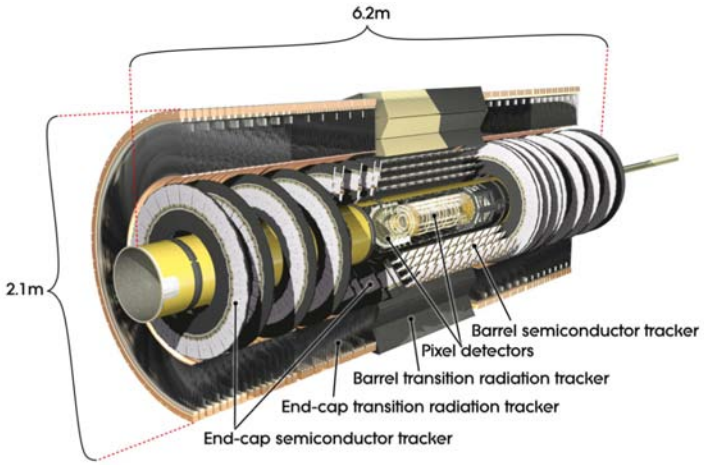

Figure 7.5: Cut-away view of the ATLAS inner detector.

7.2.1 Tracking chamber

The inner detector and its dimensions are shown in Figure 7.5. Closest to the beam line are discrete, high-resolution semiconductor pixel detectors and silicon mircostrip detectors. They cover the region used for precision physics, namely $|\eta| < 2.5$, and are used for pattern recognition, momentum and vertex measurements and electron identification. Secondary vertex measurements are especially good in the innermost layers of the pixels, at a radius of about 5 cm. In the barrel region, the cells are arranged on concentric cylinders around the beam axis; in the end-caps, they are located on disks perpendicular to the beam axis.

Surrounding the pixel and microstrip detectors are xenon-based, gas-filled, straw-tube tracking detectors used to detect transition radiation. These are arranged parallel to the beam axis in the barrel region and radially in wheels in the end-caps. Overall, they cover a range $|\eta| < 2.0$. For each beam crossing at design luminosity, the density of charged particle tracks in the inner detector is very large (on the order of 1000 tracks within $|\eta| < 2.5$). In order to locate vertex positions and momentum resolutions precisely, both the pixel and microstrip trackers as well as the transition radiation trackers are required.

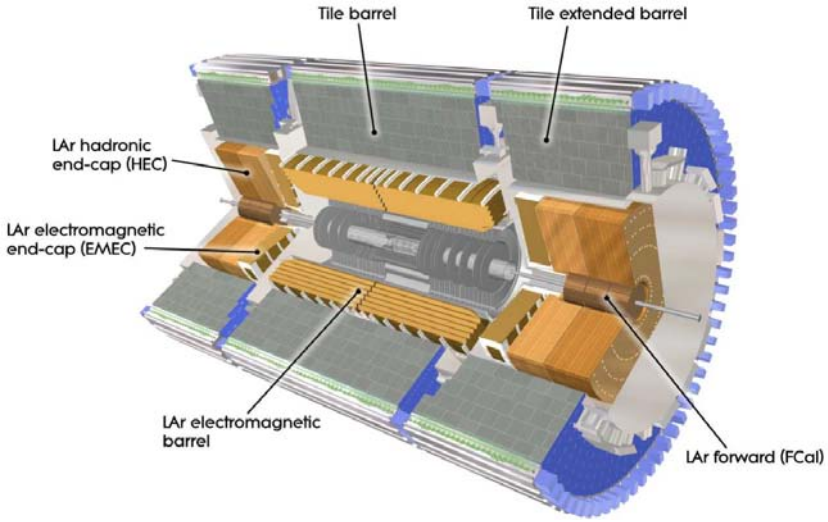

Figure 7.6: Cut-away view of the ATLAS calorimeter system.

7.2.2 Electromagnetic and hadronic calorimeters

The next concentric layer in the detector is the calorimeter, made of high-granularity liquid argon* (LAr). The various components of the calorimeter are shown in Figure 7.6. This sub-detector is designed for precision measurements of electrons and photons (fine grain EM calorimeter) and jets (coarse grain hadronic calorimeter). The thickness of the calorimeters have been designed specifically to minimise punch-through into the muon system, which is the outer layer surrounding the calorimeter.

The EM calorimeter is a lead-LAr detector covered with accordion-shaped kapton electrodes and lead absorber plates (the accordion geometry allows for complete ϕ symmetry). The barrel and two end-caps that constitute the calorimeter are housed in individual cryostats but the calorimeter and the central solenoid share a common vacuum vessel. The barrel consists of two identical half-barrels separated by a 4 mm gap at the origin. In the $|\eta| < 2.5$ region, the calorimeter is segmented in three sections: the end-caps are each divided into two coaxial wheels, the inner wheel being divided into two sections in depth.

There are three hadronic calorimeters. The first directly outside the EM calorimeter is the tile calorimeter, made of a steel absorber and scintillating tiles. It consists of a barrel in the region

*In order to facilitate high spatial resolution, the LAr has a large number of readout cells.

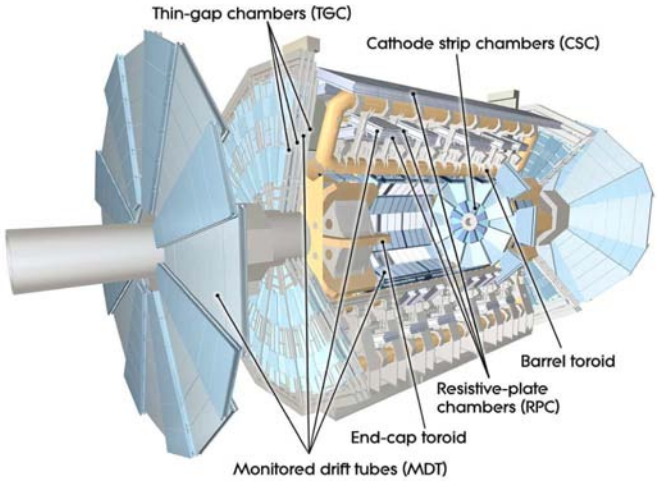

Figure 7.7: Cut-away view of the ATLAS muon system.

$|\eta| < 1.0$ and two extended barrels in the region $0.8 < |\eta| < 1.7$, all divided azimuthally. Next is the LAr hadronic end-cap calorimeter, which consists of two independent wheels for each end-cap and extends out from $|\eta| = 1.5$ to $|\eta| = 3.2$ (thus overlapping with the tile and forward calorimeters). These are located directly behind the EM calorimeter end-caps and share the same LAr cryostats with them and the third hadronic calorimeter, the LAr forward calorimeter. Each wheel consists of two sections in depth and 32 wedge-shaped modules. The wheels are made of parallel copper plates interleaved with LAr gaps, LAr being the active sampling medium. Finally, the LAr forward calorimeter, which is recessed by 1.2 m with respect to the EM calorimeter front face, consists of three modules per end-cap. The first module is made of copper and is used for EM measurements; the other two are made of tungsten and measure hadronic interactions. All the metal components are interspersed with the active LAr medium.

7.2.3 Muon spectrometer

The last of the three major sub-detectors of ATLAS is the muon spectrometer. Its components are found in the outermost layer, surrounding the calorimeter, as shown in Figure 7.7. The spectrometer consists of three high-precision tracking chambers with timing resolution of the order of $1.5 - 4$ ns. The first tracking chamber consists of monitored drift tubes that provide a precision measurement of the track coordinates over the range $|\eta| > 2.0$. Next are the cathode strip chambers, used at large pseudo-

rapidities to deal with the higher rate and background conditions in this region. The trigger chambers cover a region $|\eta| < 2.4$ and have three purposes: to provide bunch-crossing identification, well-defined p_T thresholds and a measure of the muon coordinate in the direction orthogonal to that determined by the precision tracking chambers. Finally, resistive plate chambers and thin gap chambers are located in the barrel and end-cap regions, respectively. They are used to make rough measurements in η and φ.

The three toroid magnets already mentioned, generate strong bending power for the spectrometer. This large deflection of muons in the η-direction leads to excellent muon momentum resolution and minimised multiple-scattering effects. The end-cap coil system is rotated by 22° with respect to the barrel coil system to optimise bending power at the interface between the two systems. The bending power, characterised by the field integral* $\int B\,dl$, is region-dependent. In the region

- $|\eta| < 1.4$: the large barrel toroid provides $1.5 - 5.5$ Tm bending power
- $1.6 < |\eta| < 2.7$: the two smaller end-cap magnets at the ends of the barrel toroid provide $1 - 7.5$ Tm bending power
- $1.4 < |\eta| < 1.6$: the combination of barrel and end-cap fields provides a lower bending power.

The resulting fields are essentially orthogonal to the muon trajectories and minimise multiple scattering. Magnetic field reconstruction is used to determine the bending power along the muon trajectory to a few parts in a thousand. 1800 Hall sensors are used to monitor the field throughout the spectrometer. These readings are compared to field simulations and used to reconstruct the position of the toroid coils as well as any nearby metallic structures that may cause deviation.

The inner detector and calorimeters also play a key role in muon detection. The inner detector's solenoid magnet makes an independent precise muon p_T measurement, which dominates at $p_T < 30$ GeV (but can go up to 200 GeV). The calorimeters have a tracking system that detects muons in the range $|\eta| < 2.5$. They measure energy loss of muons due to electromagnetic interactions (successive deflections, bremsstrahlung and direct e^+e^- pair production) with the detector material. Calorimeter

*B is the field component normal to the muon direction and the integral is taken along an infinite-momentum muon trajectory, between the innermost and outermost muon-chamber planes.

signals help in indirect ways too, for example, by absorbing hadrons, electrons and photons (thereby leaving a cleaner signature for the muon spectrometer).

The ATLAS detector has been designed to be efficient in muon detection since muons are an important part of a variety of physics analyses. In particular, events that have isolated and high p_T muons tend to be the interesting ones, whereas background events do not usually have muons of this type. High p_T muons have the advantage that they travel through all three parts of the muon spectrometer, making for much easier detection than muons with low p_T. Factors that affect momentum resolution at intermediate and high p_T include multiple scattering, tube resolution and autocalibration and chamber alignment.

ATLAS can measure muon kinematics precisely up to 1 TeV but low p_T muons often go undetected because they are not energetic enough to make it to the spectrometer. The inner material that a muon must pass before reaching the spectrometer is approximately 100 radiation lengths' worth. Analyses requiring low p_T muons are therefore very tricky and are often plagued by poor statistics. The main contributor to the momentum resolution for low p_T muons is energy loss fluctuations through the material in the front of the spectrometer.

7.2.4 Forward detectors

In addition to the main detector components, ATLAS also has three smaller detector sub-systems that cover the forward region. LUCID (LUminosity measurement using Cerenkov Integrating Detector) is the main online relative-luminosity detector, which detects inelastic p-p scattering in the forward region. ALFA (Absolute Luminosity For Atlas) consists of scintillating fibre trackers located inside Roman pots. Thirdly (and most importantly for this thesis due to its very rapidity-forward position) is the ZDC (Zero-Degree Calorimeter), located at the point where the single beam pipe divides back into two independent pieces.

The ZDC consists of layers of alternating quartz and tungsten plates, surrounded by photo-multiplier tubes. It is used to determine the centrality of HI collisions by detecting forward ($|\eta| > 8.3$) neutrons and photons. This sub-detector is also helpful in determining vertex locations without the use of the

inner detector: its time resolution is approximately 100 ps which allows it to locate the interaction point within 3 cm along the z-axis.

7.2.5 Trigger

For practical reasons, not all detected events are stored for offline processing. The p-p interaction rate at full design luminosity is approximately 1 GHz. Storing all event data at this rate would require an extraordinary amount of resources. Instead, ATLAS uses a multi-level trigger system to select what are likely the most interesting events, thereby reducing the final recorded output rate to about 800 Hz at full design luminosity. The event selection is carried out by three trigger systems: Level 1 (reduces the rate to $75-100$ kHz), Level 2 (reduces the rate to 5 kHz) and the Event Filter (reduces the rate to the final 800 Hz). This final selection is moved to the CERN computer centre for permanent storage, which can be accessed by all collaboration members at any time from anywhere.

7.3 Muon Reconstruction

The next step after particle detection by ATLAS is to use information from the detector to reconstruct the particles that these signatures suggest may have been created in a collision event. The purpose of muon reconstruction is to identify every muon in an event and measure its position and momentum. Muon signatures in the detector consist of a track in the inner detector and the spectrometer and little energy deposition in the calorimeter. An example of an event with two muons is shown in Figure 7.8 in a cross-sectional view of the detector. Inner detector tracks are shown in grey in the inner-most circle. Calorimeter energy deposits are shown with yellow spots. The two stark yellow lines are muons that make it all the way through the many layers of the detector to the muon spectrometer. Also shown in the figure at the bottom is a longitudinal view within the inner detector. The multi-coloured rings are vertex positions to which tracks are attributed. The two muons belong to the red vertex, in particular.

ATLAS uses various strategies to reconstruct muons, given detector signals from the inner tracking chamber, calorimeter and spectrometer. Track reconstruction in the inner detector occurs in three logical stages:

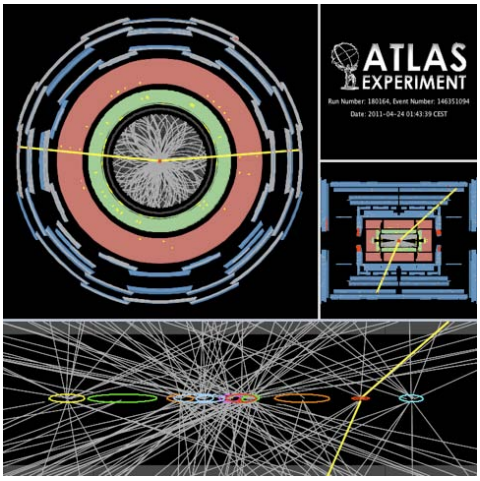

Figure 7.8: An event display showing a dimuon event in the ATLAS detector [79].

1. Pre-processing: raw data from the detector is converted into clusters.
2. Track-finding: various tracking algorithms are applied to the clusters to identify actual tracks.
3. Post-processing: primary vertices are reconstructed using a vertex finding algorithm, after which photon conversions and secondary vertices are identified by the relevant algorithms.

The various algorithms used to implement reconstruction strategies are classified into two broad families: *Staco* and *Muid*. Each reconstruction strategy has two algorithms, one belonging to the Staco family and one to the Muid family. The types of algorithms will be explained below within the context of the reconstruction strategy they implement.

Standalone muons are those reconstructed by extrapolating spectrometer tracks toward the beam line. Track segments are built in each station in the spectrometer and then linked together to form the muon track. Staco then calculates energy loss based on what material in the calorimeter has been traversed. Muid also uses this calorimeter energy deposition measurement. The standalone muon strategy has a larger coverage than strategies that use only inner detector tracks ($|\eta| < 2.7$ compared to $|\eta| < 2.5$), but it has holes near $\eta = 0.0$ and $\eta = 1.2$. It is also fairly poor for low momentum muons, since these seldom have tracks in the spectrometer.

Combined muons have both spectrometer tracks and inner detector tracks. The quality of the match between the two tracks is quantified using a chi-square parameter. Staco combines the inner

and outer track vectors statistically. Muid partially refits, starting with the inner track and adding on the spectrometer track. Combined muons have high efficiency and are therefore the preferred strategy in physics analyses. However, they do suffer from higher fake rates.

Tagged muons are identified starting with inner detector tracks and then extrapolating to a nearby hit in the spectrometer. As with the combined muons, Staco checks the difference between the extrapolated track and a spectrometer hit using a chi-square test. Muid, on the other hand, utilises an artificial neural network. Unlike the standalone and combined muons, Staco only supplements Muid in this case, i.e. it only uses inner detector tracks that Muid does not.

There are also several calorimeter-based muon tagging algorithms on the market. These are capable of recovering muons lost to the spectrometer, namely those with low p_T or those that pass through η regions poorly covered by the spectrometer. Examples of such algorithms are `LArMuID` and `TileMuID`), which measure energy hits within some range on a calorimeter cell cluster. This cluster can then be matched to a track in the inner detector by a track-seed algorithm such as `CaloMuonTag` or `CaloMuonLikelihoodTool`).

Reconstructed muon information is stored for all physics runs at the LHC, in varying levels of detail. Both the Staco and Muid results are always included. These data sets can be used for a variety of analyses, including dimuon decay of exclusive J/Ψ vector-mesons in HI collisions. The appropriate algorithm to use depends on the analysis being done. In most cases, the difference between Staco and Muid muons is negligible. For low p_T muons, however, the better algorithm is Muid since it relies more heavily on inner detector tracks.

7.4 Monte Carlo Simulations

Reconstructed data is simply a means of attempting to identify true events that occurred in a collision, based on measurements made by the various components of the detector. While these algorithms use cutting-edge techniques, there is no way of guaranteeing that the objects being reconstructed are the true particles. Computer simulations are therefore done side-by-side with detector measurements to simulate the behaviour of the system under various running conditions. Such algorithms are based on more generic Monte Carlo* (MC) techniques, a group of algorithms based on statistical methods. An MC event generator is software written to model any physical process that is governed by a statistical process. In addition to MC methods, it makes use of an array other computational techniques.

ATLAS utilises several different event generators, such as Pythia [80], Herwig [81] and Sherpa [82], to simulate physics processes. The various generators have their advantages and disadvantages, depending on the kind of particle process being studied. The output from these simulations can be fed subsequently through the full simulation of the ATLAS detector, which is implemented by a program called GEANT4 [83]. The results of this procedure are intended to model as closely as possible the detector response to a particle process. The majority of the generators used by ATLAS can be run independently or through the ATLAS framework (if knowledge of the detector response is desired). In the latter case, typical output files include both the truth event record, pertaining to the real objects in the event, as well as the reconstructed event record.

The MC generator used in this thesis is a specialist generator, called STARlight [84]. It is capable of simulating proton and HI collisions, but it is usually used to simulate the latter. More details about STARlight will be provided in the next chapter.

*The name *Monte Carlo* comes from the capital city of Monaco, famous for its casinos. Many of the games played at the casinos can be modelled using the statistical MC methods.

Chapter 8

A Monte Carlo Feasibility Study

High energy proton collisions are inherently plagued by large QCD backgrounds, dominated by hadron jet production. This large background makes the interesting events in a collision difficult to find due to poor statistics. The solution at the LHC to remedy this issue is to increase the integrated luminosity, thereby increasing the number of signal events. For low-p_T studies like exclusive J/Ψ production, high luminosity is more of a hindrance due to *pile-up* (an overwhelming number of events in a collision, expected to appear around $\int dt\,\mathcal{L} = 10^{33}$ cm^{-2}s^{-1}). Instead, one can turn to Pb-Pb collisions, in which the integrated luminosity is comparably low.

The main Pb-Pb data-taking period at the LHC was from 11 Nov to 7 Dec 2011, during which 3.5 TeV Pb beams were used. Data worth 160 μb^{-1} total integrated luminosity was collected during this time. MC samples were made sided-by-side to simulate these HI collisions. In particular, this work focuses on samples generated using STARlight and subsequently run through the ATLAS detector simulation framework.

The chapter begins with a Section dedicated to how the STARlight generator works. Section 8.2 follows with a muon reconstruction efficiency study using a STARlight sample. Then, Section 8.3 provides the results from the feasibility study done to estimate the expected cross-section for exclusive J/Ψ vector-meson production in Pb-Pb collisions in ATLAS. Finally, the chapter is closed with a brief

mention of exclusive studies done by other collaborations at the LHC.

8.1 STARlight

STARlight is an MC event generator that was written in 1995 for the STAR (Solenoidal Tracker At RHIC) collaboration at RHIC (Relativistic Heavy Ion Collider). Initially, it was dedicated to simulating ultra-relativistic gold-gold collisions at 200 GeV per nucleon, since this was its purpose at STAR. After being utilised for several years and after many modified versions of the code, the software is now more versatile. [85] provides a detailed description of the generator in terms of how it functions and how to implement it.

In its present form, STARlight can be used to simulate collisions between protons, deuteron and heavy ions. It has several final-state options, including J/Ψ, ρ, ω, φ, $\psi(2S)$, Υ, $\Upsilon(2S)$ and $\Upsilon(3S)$ vector-mesons. However, only decay channels that have two-body final states can be modelled, such as $J/\Psi \to \mu^+\mu^-$. In terms of user options, STARlight is fairly accommodating. If need be, it is able to incorporate a Breit-Wigner factor for wide particle resonances. It can model both photon-photon and photonuclear interactions, as described in the beginning of Chapter 2. The user is also given the choice between exclusive and inclusive interactions.

Since the process being studied in this work is exclusive vector-meson production via photonuclear interactions, this is the process that will be used as an example to explain how STARlight runs. The software uses the Gaussian Quadrature method to discretise integrals: the area under the curve is divided into n thin rectangles and then summed over. A $2n-1$ polynomial is then fitted to the curve. The package comes with its own random number generator, the *Mersenne Twister*. The Glauber model method is used to calculate the total cross-section [86]. The logical order of steps executed by STARlight when it is run is given below:

1. A reference table of total cross-sections (dependent on centre-of-mass energy and rapidity) for vector-meson production is created.
2. A table for the differential cross-section (also for different energies and rapidities) is created and stored to a file called slight.txt. The differential cross-section values are normalised by the total cross-section.
3. An event is generated with a randomly selected energy and rapidity that fit the probability distribution determined through an MC algorithm.
4. These values are compared to those on the table. If the values correspond, the event proceeds.
5. A collision is simulated with the given energy and rapidity and the meson is created.
6. In the case that deuterons or protons are collided, its momentum and the virtual photon mometum are calculated. These are used to determine the vector-meson's transverse momentum.
7. The transverse momentum and rapidity are used to calculate the meson's four-momentum.
8. The meson is decayed immediately into the products dictated by the chosen decay channel. STARlight then assigns the decay angles, ϕ and θ, as governed by spin and helicity conservation.
9. The four-momenta are transformed from the centre-of-mass frame to the laboratory frame.
10. The products' information (particle type, charge and four-momentum) is stored in the output file slight.out.
11. The whole process is repeated until the required number of vector-mesons has been produced.

The output file slight.out records all relevant event information, such as the event number, the number of tracks and vertices per event, the vertex coordinates and the track momenta. If STARlight is run independently on a personal computer, this output serves as sufficient information to study simulated vector-meson production. Alternatively, the file can get fed into a detector's MC framework to simulate the detector response.

The STARlight MC sample used for this analysis consists of 12 000 exclusive J/Ψ vector-mesons created in a 2.76 TeV simulated Pb-Pb collision. Since the cross-section for this process is 0.7 mb, the sample corresponds to an integrated luminosity of 17 μb^{-1}. These true events were then reconstructed

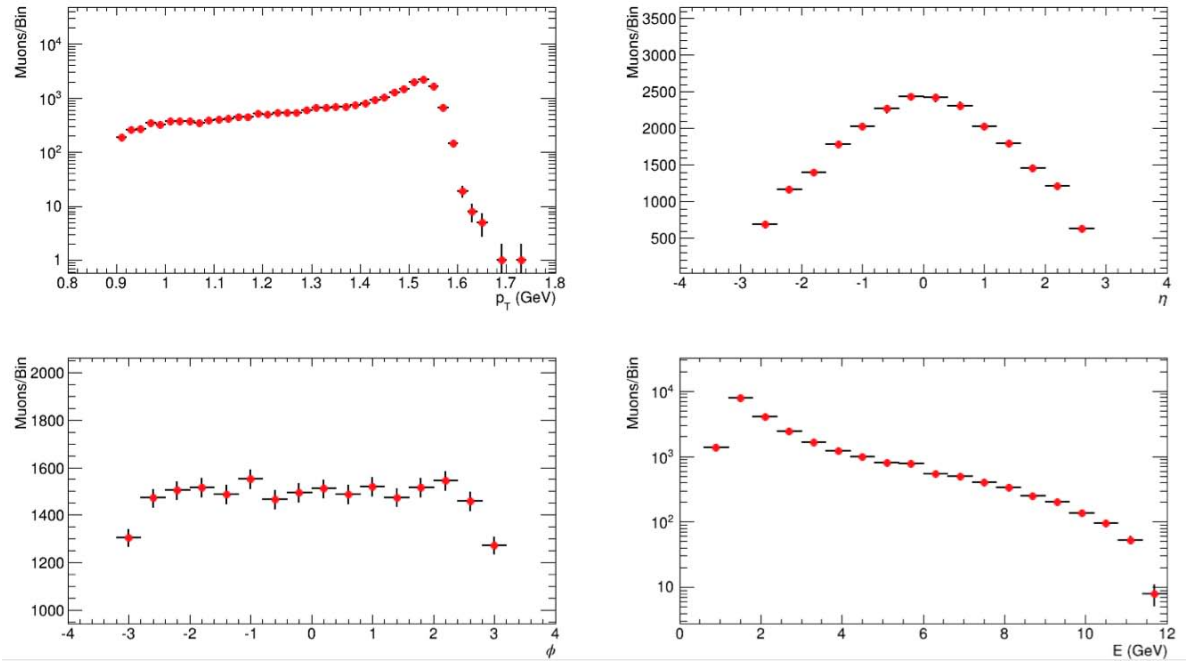

Figure 8.1: Kinematic histograms for the true muons produced by STARlight.

using ATLAS software to determine the detector response. The kinematic histograms for the true muons are shown in Figure 8.1.

8.2 Muon Reconstruction Efficiency

Performance studies done by ATLAS aim to quantify how effective the detector is at correctly identifying particle species at various momentum scales. Studies of this kind typically aim to calculate performance measures like *reconstruction efficiency*, *fake rate* and *momentum resolution*. In this analysis, the focus will be on muon efficiencies, although the fake rate and momentum resolution will also be described for posterity sake. Efficiency is the fraction of true muons that get reconstructed. Once quality cuts are applied to reconstructed muon tracks, the efficiency is calculated by dividing the the number of reconstructed muons that pass the cuts by the total number of true muons. The fake rate is the mean number of fake muons that get reconstructed per event. It is calculated as the fraction of reconstructed tracks that pass the cuts but are not matched to a true muon. Finally, the fractional

momentum resolution is defined as

$$\rho := -\frac{\Delta p_T}{p_T} = \frac{\frac{1}{p_{T\,(\text{true})}} - \frac{1}{p_{T\,(\text{reco})}}}{\frac{1}{p_{T\,(\text{true})}}} = \frac{p_{T\,(\text{reco})} - p_{T\,(\text{true})}}{p_{T\,(\text{reco})}} \tag{8.1}$$

where $p_{T\,(\text{true})}$ and $p_{T\,(\text{reco})}$ are the true muon and reconstructed muon transverse momenta, respectively. For a spectrometer uniform in η and ϕ, ρ would be normally distributed. In ATLAS, however, the magnetic field varies with η and ϕ, and a more appropriate distribution must be determined and used.

For standalone muons (as described in the previous chapter) the reconstruction efficiency can be calculated as the fraction of true muons that have a reconstructed muon match within a cone of $\Delta R < 0.05$ where

$$\Delta R = \sqrt{(\eta_{\text{reco}} - \eta_{\text{true}})^2 + (\phi_{\text{reco}} - \phi_{\text{true}})^2}. \tag{8.2}$$

The tag-and-probe method is usually used to calculate muon efficiencies in ATLAS. This method requires two reconstructed tracks in the inner detector and at least one associated track in the muon spectrometer. Unfortunately, this method is only effective at medium and large p_T (in the range $10 - 500$ GeV), where track reconstruction has an efficiency of 97% and a momentum resolution of $3 - 4\%$ [75]. Since the muons from exclusive J/Ψ decay have low p_T, there are very few tracks in the spectrometer. For this reason, the tag-and-probe method is not effective. Instead, a rudimentary calculation will be done below, in which the fraction of reconstructed muons over true muons is used as the efficiency.

8.2.1 Muon efficiency in the exclusive J/Ψ sample

The Muid reconstruction algorithm is used for this study because it tends to be slightly more efficient than Staco for low p_T muons. Of the 2×12000 true muons in the sample, only 1278 (about 5%) of them get reconstructed by Muid. Most of these are attributed to single-muon events, with only 16 reconstructed events containing two muons. The kinematic histograms for the reconstructed muons are shown in Figure 8.2. The reconstructed muon p_T is smeared to higher values than what it truly is. From the η plot, one can see that very forward muons are not reconstructed at all.

How well the reconstructed and true muons match can be quantified using ΔR, as defined in Equation 8.2. If the ΔR value between a true and reconstructed muon is small, it means that their

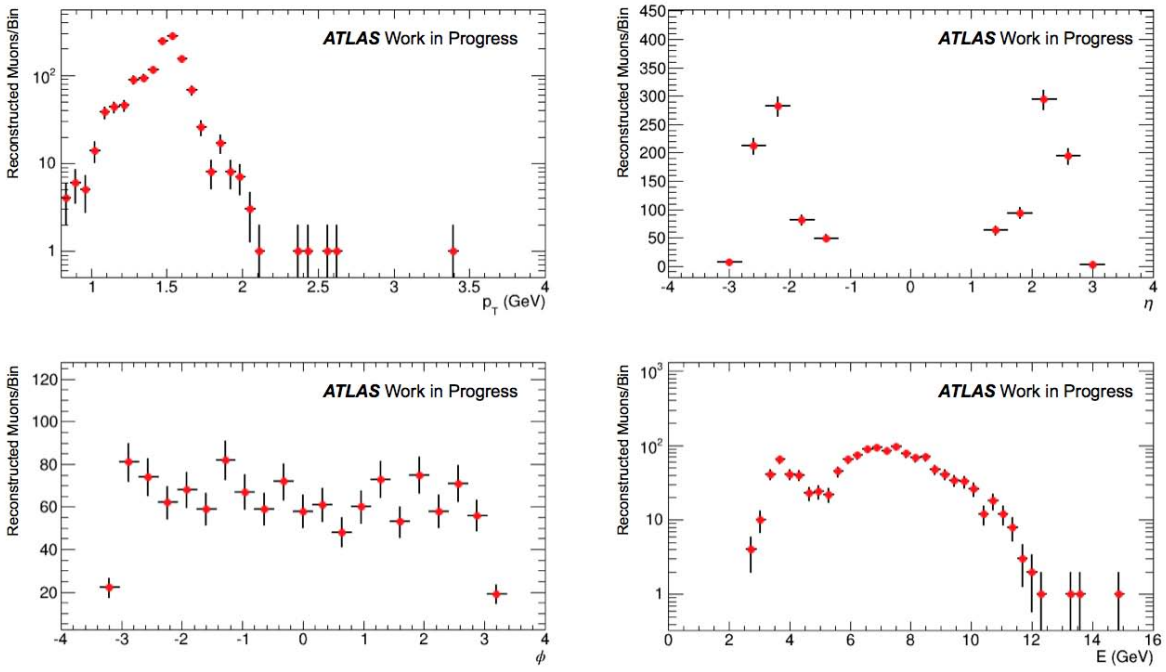

Figure 8.2: Kinematic histograms for the reconstructed muons.

η and ϕ values are very close and so the match is good. For each reconstructed muon in the sample, one can attempt to find a matching true muon within a cone of $\Delta R < 0.05$. The efficiency can be determined by finding the fraction of true muons with a reconstructed match over all true muons. This is done bin-by-bin, using the true muon p_T histogram and the reconstructed muon p_T histogram. The result of this procedure gives an approximate efficiency of 0.04, averaged over a p_T range up to 1 GeV. Since the p_T of these muons is so low, it is expected that the efficiency is very poor. This is supported by a similar efficiency plot taken from [75], as shown in Figure 8.3. Although the data used to make this figure is different, the point can be made that efficiencies at low p_T are extremely poor.

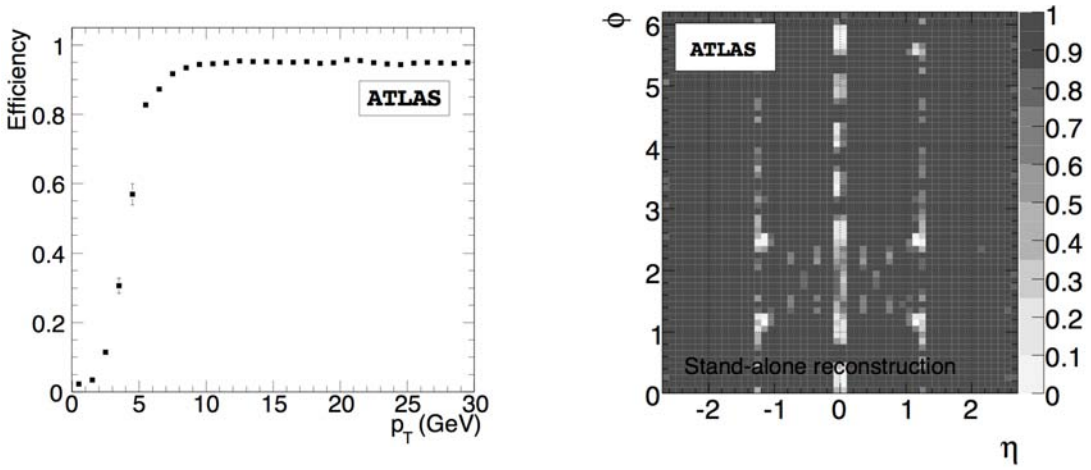

Figure 8.3: a. Efficiency versus p_T, taken from [75], describing muon reconstruction performance. b. Efficiency versus η and ϕ for a sample of $p_T = 50$ GeV muons [75].

8.3 Expected Number of Exclusive J/Ψ Events

In order to identify the events of interest in a sample, one can apply a set of selection criteria that each event must satisfy. These cuts are governed by the interaction of interest. Six requirements are placed on events in the STARlight sample analysed in this chapter to identify exclusive J/Ψ vector-mesons that decay to two muons. The first two and most obvious cuts are that the event should consist of two muons and nothing else and they should be of opposite charge. Since the η acceptance in ATLAS is in the range $|\eta| < 2.7$, this is the third cut, applied to each muon in the event. The J/Ψ vector-meson produced in an exclusive ultra-peripheral collision has a low p_T, so the difference in p_T of the two muons that come from it should also be small; the cut $\Delta p_T < 0.1$ GeV is imposed. Despite having a small difference in p_T, the two muons can still have large individual p_T. Due to momentum conservation, they should travel back-to-back. This cut is implemented by requiring that the azimuthal angle between the two muons is close to π, namely $|\Delta\phi - \pi| < 0.1$. Finally, the invariant mass of the muon pair should be close to that of the J/Ψ, so the cut 3.05 GeV $< M_{\mu^+\mu^-} <$ 3.12 GeV is used (the J/Ψ mass is 3.096 GeV [13]).

The MC sample used here contains 12 000 exclusive J/Ψ vector-mesons that have been decayed to two muons. Applying the six cuts should therefore not eliminate too many events. The cut flow and resulting number of events is given below:

1. Two muons in the event (11793 events).
2. Two muons have opposite charge (11793 events).
3. $|\eta| < 2.7$ for each muon (11793 events).
4. $\Delta p_T < 0.1$ GeV (11634 events).
5. $|\Delta\phi - \pi| < 0.1$ (11494 events).
6. $3.05 < M_{\mu^+\mu^-} < 3.12$ GeV (11440 events).

This means that only about 5% of the true events are eliminated by the selection criteria. Since most true events pass the cuts, it appears that this set of selection criteria is a fair one to use when searching for exclusive J/Ψ's.

The selection criteria can now be applied to real Pb-Pb collision data collected by ATLAS. Although this exercise has not been done for this thesis, the number of signal events expected to be observed can be determined. Given the cross-section already quoted, $\sigma = 0.7$ mb, and the total integrated luminosity from the 2011 Pb-Pb data-taking period, $\int dt\mathcal{L} = 160\ \mu b^{-1}$, the expected number of exclusive J/Ψ events that decay in the dimuon channel is

$$\begin{aligned} N &= \sigma \int dt\mathcal{L} \\ &= \Big(0.7 \times 10^{-3}\ \text{b}\Big)\Big(160 \times 10^{6}\ \text{b}^{-1}\Big) \\ &= 112\ 000 \text{ events.} \end{aligned} \tag{8.3}$$

The poor efficiency for low p_T muons has not been incorporated into this number. In the previous section, it was stated that the Muid algorithm only manages to reconstruct 16 dimuon events in the 12 000 event sample. This gives a rudimentary efficiency of approximately $\frac{16}{12000} \approx 0.1\%$. Applying this to N above reduces the expected number of candidate events to around 150 events. The selection criteria miss approximate 5% of these events, which reduces this number further. In summary, using the majority of the heavy ion data collected thus far at the LHC, ATLAS is only able to identify a small fraction of J/Ψ vector-mesons produced in exclusive interactions.

8.4 Other Experiments at the LHC

Besides ATLAS, the three other major experiments at the LHC are also interested in exclusive studies. ALICE, in particular, has measured the cross-section for exclusive J/Ψ production in ultra-peripheral Pb-Pb collisions at 2.76 TeV. In [88], a data sample corresponding to 55 μb^{-1} integrated luminosity was analysed for dimuon events in the rapidity range $-3.6 < y < -2.6$. After applying selection criteria, 78 candidate events were found. The cross-section obtained was $\frac{d\sigma}{dy} = 1.00 \pm 0.18(\text{stat})^{+0.24}_{-0.26}(\text{sys})$ mb, where the statistical and systematic uncertainties have been quoted as well. The dimuon invariant mass and p_T spectra taken from this analysis are shown in Figures 8.4 and 8.5, respectively.

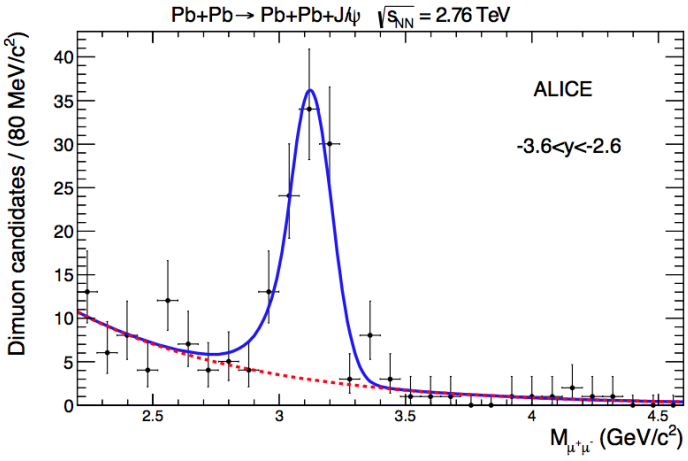

Figure 8.4: Dimuon invariant mass spectrum from [88].

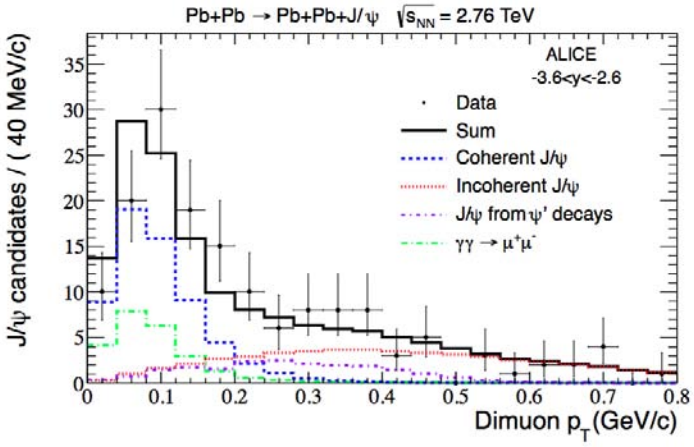

Figure 8.5: Dimuon p_T spectrum from [88] including fits using various MC.

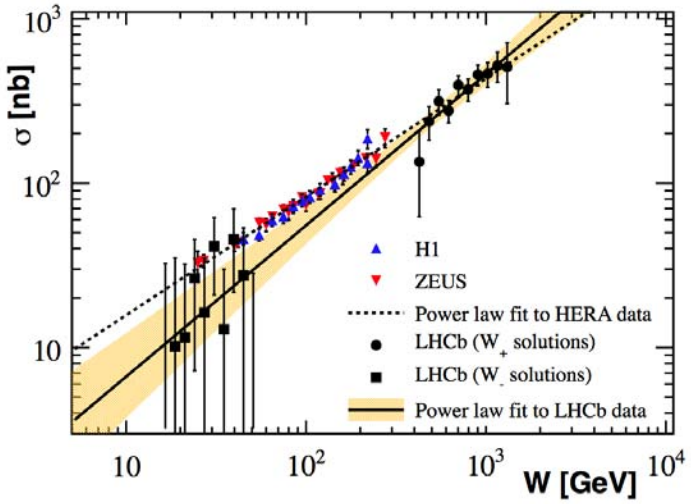

Figure 8.6: Power-law behaviour of the J/Ψ photo-production cross-section as a function of the centre-of-mass energy W [89].

Instead of heavy ion collisions, the LHCb collaboration has measured the cross-section for exclusive J/Ψ production in p-p collisions [89]. Analysing a sample with 36 pb^{-1} integrated luminosity, they have obtained a cross-section of $\sigma = 307 \pm 31(\text{stat}) \pm 36(\text{sys})$ pb, an order of 10^6 smaller than that expected from Pb-Pb collisions. An interesting peripheral result from this study is the confirmation of the power law behaviour of the cross-section as a function of centre-of-mass energy, as observed at HERA [90]. This is shown in Figure 8.6.

The last major detector at the LHC is CMS. Thus far, it has only published results of dimuon production from photon-photon interactions in p-p collisions (in terms of exclusive analyses). In [91], 40 pb^{-1} integrated luminosity-worth of data was analysed and 148 candidate events were identified. The major difference between this analysis and the kind discussed in this thesis is the muon p_T range. In [91], one of the cuts applied is that each muon p_T should be greater than 4 GeV. This immediately eliminates the poor efficiency issue experienced at low p_T.

End of Part II

Conclusion

In this thesis, exclusive J/Ψ vector-meson production in nuclear collisions has been discussed from two different viewpoints - a theoretical one and an experimental one. These two approaches connect via the cross-section; a cross-section determination has therefore been the goal of Parts `I` and `II`, albeit through distinctly different means. The common starting point for both theory and experiment is to understand the photonuclear processes that dominate ultra-peripheral heavy ion collisions, which is the context in which this work has been done.

From the theoretical perspective, one begins with the initial state of the colliding nuclei. At small x_{Bj}, the onset of saturation effects leads to constrained gluon occupation numbers in the nuclei. The CGC effective field theory attempts to describe this dense gluonic medium and in so doing, provide the initial condition for the collision. In ultra-peripheral collisions, the interaction is triggered by photons, which can fluctuate to colour objects like a quark dipole that have a chance of interacting with the target nucleus. The interaction between such a colour projectile and the gluonic target field is contained in an energy-averaged n-point correlator, where n is the number of particles in the projectile. These n-point correlators enter the cross-section directly as integrals over the impact parameter and constitute the entire strong interaction between projectile and target.

In order to understand the behaviour of correlators of this kind, the appropriate mathematical tool to use is the JIMWLK equation. The JIMWLK equation can be written as the Balitsky hierarchy. While this may be a useful analytical tool, some kind of approximation scheme is necessary to be able to make practical calculations and obtain phenomenological results. One example of such an approximation is the GT, which approximates the correlator by a parametrisation with new degrees

of freedom represented by 2-point functions $G_{\boldsymbol{uv}}$. This is the work that has been discussed in the literature and has been used as a springboard in this thesis.

The first non-trivial step beyond the GT is to consider higher-point functions as degrees of freedom that enter the approximation of the correlator. Specifically, the totally antisymmetric and symmetric 3-point functions $G^f_{\boldsymbol{uvw}}$ and $G^d_{\boldsymbol{uvw}}$ have been investigated. In calculating the 2-point and 3-point correlators required for the Balitsky equation, only certain coincidence limits of the new functions are needed. A full investigation of the true 3-point functions with three distinct coordinate indices is still needed. An attempt has been made for the starting point of such a study, which requires a 6×6 matrix of 6-point correlators. Deriving parametrisation equations for these monstrous objects leads to lengthy expressions whose discussion has been postponed to the Appendix. For the time being, a cross-section expression has been determined using the established parametrisations of the 2- and 4-point correlators as input.

In Chapter 6, the total and exclusive cross-sections were discussed. The origins of the 4-point correlators investigated in Chapters 3 and 4 were shown. The dipole correlator

$$\left\langle \frac{\mathrm{tr}(1 - U_{\boldsymbol{x}} U^\dagger_{\boldsymbol{y}})}{N_c} \right\rangle_Y$$

enters the total cross-section and the 4-point correlator

$$\left\langle \frac{\mathrm{tr}(U_{\boldsymbol{y}'} U^\dagger_{\boldsymbol{x}'})}{N_c} \frac{\mathrm{tr}(U_{\boldsymbol{x}} U^\dagger_{\boldsymbol{y}})}{N_c} \right\rangle_Y$$

enters the vector-meson production cross-section. The average of products with different coordinate indices comes about due to the presence of the final state projections in the middle of the average,

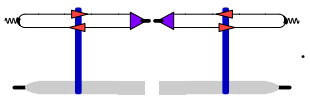

.

The fact that different correlators enter different types of cross-sections in such an obvious way leads to an interesting question: what is the result of probing differences of the kind

$$\left\langle \frac{\mathrm{tr}(U_{\boldsymbol{y}'} U^\dagger_{\boldsymbol{x}'})}{N_c} \frac{\mathrm{tr}(U_{\boldsymbol{x}} U^\dagger_{\boldsymbol{y}})}{N_c} \right\rangle_Y - \left\langle \frac{\mathrm{tr}(U_{\boldsymbol{y}'} U^\dagger_{\boldsymbol{x}'})}{N_c} \right\rangle_Y \left\langle \frac{\mathrm{tr}(U_{\boldsymbol{x}} U^\dagger_{\boldsymbol{y}})}{N_c} \right\rangle_Y ,$$

where the first term comes from one type of process cross-section and the second term from another? These kinds of questions have not been investigated in this thesis because they would require consideration of different cross-section calculations - but they leave scope for further work.

From the experimental perspective, the exclusive vector-meson cross-section calculation comes with several hurdles. At the LHC, pile-up in p-p collisions makes exclusive vector-meson production a difficult analysis. Turning to Pb-Pb collisions is still complicated due to the poor efficiency with which low p_T muons are reconstructed in ATLAS. Since these muons are critical for the reconstruction of the J/Ψ vector-mesons from which they originate, very few signal events are found in collision data. Part II of this work constitutes a feasibility study using MC simulations to predict how many exclusive J/Ψ's are expected in all the Pb-Pb data collected thus far at the LHC. After incorporating the low efficiencies, the result looks fairly bleak. The standard analysis methods used here will have to be abandoned at the low p_T scale should one wish to find exclusive J/Ψ's in collision data. One potential workaround is to use only inner detector tracks with very strict selection cuts to identify muons. The ZDC discussed in Chapter 7 could also prove useful in ensuring the exclusivity requirement is met, although it does have a limited high-rapidity range.

The outlook for high-energy particle physics on the whole, appears more appealing. What with particle physicists always campaigning for bigger, better machines, there is hope that studies like exclusive vector-meson production in nuclear collisions can be done at future colliders. One of the more promising future colliders is the LHeC (Large Hadron electron Collider) at CERN. The current design looks to build a new electron beam line (that will ultimately carry up to 140 GeV beams) at the LHC so that e-p and e-Pb collisions can be studied [92]. It is expected that the LHeC will probe new kinematic regions, thereby providing an opportunity to further test small-x_{Bj} physics.

Acknowledgements

I would like to thank my supervisor, Prof. Heribert Weigert, for countless hours of patient explanation over the years. Our discussions have been the source of most of my knowledge within this field (and of a different outlook on life and the universe). Thanks also go to my co-supervisor, Dr. Andrew Hamilton, for generous supervision and the opportunity for my "theorist brain" to learn experimental techniques. Finally, my sincere gratitude to the safety net of friends and family who have been behind me for the past two years. I owe you my sanity.

This degree has been funded by the National Research Foundation of South Africa, through a Masters Innovation Scholarship.

Bibliography

[1] H. Weigert, *Evolution at Small x_{Bj}: The Color Glass Condensate*, Prog. Part. Nucl. Phys. **55** (2005) 461-565 [hep-ph/0501087].

[2] C. Marquet and H. Weigert, *New Observables to Test the Color Glass Condensate Beyond the Large-N_c Limit*, Nucl. Phys. **A843** (2010) 68-97 [hep-ph/1003.0813].

[3] L. V. Gribov, E. M. Levin, and M. G. Ryskin, *Semihard Processes in QCD*, *Phys. Rept.* **100** (1983) 1–150.

[4] A. H. Mueller and J.-w. Qiu, *Gluon Recombination and Shadowing at Small Values of x*, *Nucl. Phys.* **B268** (1986) 427.

[5] A. H. Mueller, *Soft Gluons in the Infinite Momentum Wave Function and the BFKL Pomeron*, *Nucl. Phys.* **B415** (1994) 373–385.

[6] A. H. Mueller and B. Patel, *Single and Double BFKL Pomeron Exchange and a Dipole Picture of High-energy Hard Processes*, *Nucl. Phys.* **B425** (1994) 471–488, [hep-ph/9403256].

[7] A. H. Mueller, *Unitarity and the BFKL Pomeron*, *Nucl. Phys.* **B437** (1995) 107–126, [hep-ph/9408245].

[8] L. D. McLerran and R. Venugopalan, *Gluon Distribution Functions for Very Large Nuclei at Small Transverse Momentum*, *Phys. Rev.* **D49** (1994) 3352–3355, [hep-ph/9311205].

[9] L. D. McLerran and R. Venugopalan, *Computing Quark and Gluon Distribution Functions for Very Large Nuclei*, *Phys. Rev.* **D49** (1994) 2233–2241, [hep-ph/9309289].

[10] L. D. McLerran and R. Venugopalan, *Green's Functions in the Color Field of a Large Nucleus*, *Phys. Rev.* **D50** (1994) 2225–2233, [hep-ph/9402335].

[11] Y. V. Kovchegov, *Non-abelian Weizsaecker-Williams Field and a Two- dimensional Effective Color Charge Density for a Very Large Nucleus*, *Phys. Rev.* **D54** (1996) 5463–5469, [hep-ph/9605446].

[12] Y. V. Kovchegov, *Quantum Structure of the Non-abelian Weizsaecker-Williams Field for a Very Large Nucleus*, *Phys. Rev.* **D55** (1997) 5445–5455, [hep-ph/9701229].

[13] J. Beringer et al. (Particle Data Group), *2013 Review of Particle Physics*, Phys. Rev. **D86** (2012) 010001.

[14] J. Jalilian-Marian, A. Kovner, L. D. McLerran, and H. Weigert, *The Intrinsic Glue Distribution at Very Small x*, *Phys. Rev.* **D55** (1997) 5414–5428, [hep-ph/9606337].

[15] J. Jalilian-Marian, A. Kovner, A. Leonidov, and H. Weigert, *The BFKL Equation from the Wilson Renormalization Group*, *Nucl. Phys.* **B504** (1997) 415–431, [hep-ph/9701284].

[16] J. Jalilian-Marian, A. Kovner, A. Leonidov, and H. Weigert, *The Wilson Renormalization Group for Low x Physics: Towards the High Density Regime*, *Phys. Rev.* **D59** (1999) 014014, [hep-ph/9706377].

[17] J. Jalilian-Marian, A. Kovner, A. Leonidov, and H. Weigert, *Unitarization of Gluon Distribution in the Doubly Logarithmic Regime at High Density*, *Phys. Rev.* **D59** (1999) 034007, [hep-ph/9807462].

[18] A. Kovner, J. G. Milhano, and H. Weigert, *Relating Different Approaches to Nonlinear QCD Evolution at Finite Gluon Density*, *Phys. Rev.* **D62** (2000) 114005, [hep-ph/0004014].

[19] H. Weigert, *Unitarity at Small Bjorken x*, *Nucl. Phys.* **A703** (2002) 823–860, [hep-ph/0004044].

[20] E. Iancu, A. Leonidov, and L. D. McLerran, *Nonlinear Gluon Evolution in the Color Glass Condensate. I*, *Nucl. Phys.* **A692** (2001) 583–645, [hep-ph/0011241].

[21] E. Ferreiro, E. Iancu, A. Leonidov, and L. McLerran, *Nonlinear Gluon Evolution in the Color Glass Condensate. II*, *Nucl. Phys.* **A703** (2002) 489–538, [hep-ph/0109115].

[22] Y. V. Kovchegov, *Small-x F_2 Structure Function of a Nucleus Including Multiple Pomeron Exchanges*, *Phys. Rev.* **D60** (1999) 034008, [hep-ph/9901281].

[23] Y. V. Kovchegov, *Unitarization of the BFKL Pomeron on a Nucleus*, *Phys. Rev.* **D61** (2000) 074018, [hep-ph/9905214].

[24] I. Balitsky, *Operator Expansion for High-energy Scattering*, *Nucl. Phys.* **B463** (1996) 99–160, [hep-ph/9509348].

[25] I. Balitsky, *Operator Expansion for Diffractive High-energy Scattering*, hep-ph/9706411.

[26] I. Balitsky, *Factorization and High-energy Effective Action*, *Phys. Rev.* **D60** (1999) 014020, [hep-ph/9812311].

[27] E. Iancu and R. Venugopalan, *The Color Glass Condensate and High-energy Scattering in QCD*, hep-ph/0303204.

[28] H. Weigert, *Evolution at Small x_{bj}: The Color Glass Condensate*, *Prog. Part. Nucl. Phys.* **55** (2005) 461–565, [hep-ph/0501087].

[29] J. Jalilian-Marian and Y. V. Kovchegov, *Saturation Physics and Deuteron Gold Collisions at RHIC*, *Prog. Part. Nucl. Phys.* **56** (2006) 104–231, [hep-ph/0505052].

[30] F. Gelis, E. Iancu, J. Jalilian-Marian, and R. Venugopalan, *The Color Glass Condensate*, 1002.0333.

[31] The ATLAS Collaboration, *The CERN Large Hadron Collider: Accelerator and Experiments, The ATLAS Detector*, JINST **3** (2008) S08003.

[32] L. Evans, P. Bryant et al. *The CERN Large Hadron Collider: Accelerator and Experiments, The LHC Machine*, JINST **3** (2008) S08001.

[33] The ATLAS Collaboration, *Observation of a New Particle in the Search for the Standard Model Higgs Boson with the ATLAS Detector at the LHC*, Phys. Lett. **B716** (2012) 1-29 [hep-ex/1207.7214].

[34] The CMS Collaboration, *Observation of a New Boson at a Mass of 125 GeV with the CMS Experiment at the LHC*, Phys. Lett. **B716** (2012) 30 [hep-ex/1207.7235].

[35] F. Englert and R. Brout, *Broken Symmetry and the Mass of Gauge Vector Mesons*, Phys. Rev. Lett. **13** (1964) 321.

[36] Peter W. Higgs, *Broken Symmetries and the Masses of Gauge Bosons*, Phys. Rev. Lett. **13** (1964) 508.

[37] The ATLAS Collaboration, *Evidence for the Spin-0 Nature of the Higgs Boson Using ATLAS data*, Phys. Lett. **B726** (2013) 120 [hep-ex/1307.1432].

[38] D. Griffiths, *Introduction to Elementary Particles, 2nd ed.*, Wiley-VCH (2008).

[39] F. Halzen and A. D. Martin, *Quarks and Leptons: An Introductory Course in Modern Particle Physics*, John Wiley & Sons (1984).

[40] M. E. Peskin and D. V. Schroeder, *An Introduction to Quantum Field Theory*, Addison-Wesley (1995) 99-107, 230-237.

[41] S Bethke, *Experimental Tests of Asymptotic Freedom*, Prog. Part. Nucl. Phys. **58** (2007) 351-386 [hep-ex/0606035] Fig. 17.

[42] A. G. Ruggiero, *Scenario for the Relativistic Heavy Ion Collider (RHIC) for Brookhaven National Laboratory*, BNL-35127, RHIC-1 (1984).

[43] R. R. Wilson, *The Tevatron*, Phys. Today. **30N10** (1977) 23-30.

[44] *HERA* (1981), DESY-HERA-81-10.

[45] The CMS Collaboration, *The CERN Large Hadron Collider: Accelerator and Experiments, The CMS Detector*, JINST **3** (2008) S08004.

[46] The ALICE Collaboration, *The CERN Large Hadron Collider: Accelerator and Experiments, The ALICE Detector*, JINST **3** (2008) S08002.

[47] The LHCb Collaboration, *The CERN Large Hadron Collider: Accelerator and Experiments, The LHCb Detector*, JINST **3** (2008) S08005.

[48] The LHCf Collaboration, *The CERN Large Hadron Collider: Accelerator and Experiments, The LHCf Detector*, JINST **3** (2008) S08006.

[49] The TOTEM Collaboration, *The CERN Large Hadron Collider: Accelerator and Experiments, The TOTEM Detector*, JINST **3** (2008) S08007.

[50] The MoEDAL Collaboration, *MoEDAL TDR*, CERN-LHCC-2009-006.

[51] M. Brice, *The LHC Tunnel*, CERN Document Server © CERN.

[52] M. Brice, *Aerial View of CERN taken in 2008*, CERN Document Server © CERN (2008).

[53] E. A. Kuraev, L. N. Lipatov, and V. S. Fadin, *The Pomeranchuk Singularity in Non-Abelian Gauge Theories*, *Sov. Phys. JETP* **45** (1977) 199–204.

[54] Y. Y. Balitsky and L. N. Lipatov *Sov. J. Nucl. Phys.* **28** (1978) 822.

[55] J. Bartels, K. J. Golec-Biernat and H. Kowalski, *DGLAP Evolution in the Saturation Model*, Acta Phys. Polon. **B33** (2002) 2853-2858, [hep-ph/0207031].

[56] J. Bartels, K. J. Golec-Biernat and H. Kowalski, *A Modification of the Saturation Model: DGLAP Evolution*, Phys. Rev. **D66** (2002) 014001, [hep-ph/0203258].

[57] I. Balitsky, *Next-to-leading Order Evolution of Color Dipoles*, Nucl. Phys. **B463** (1996) p99-160, [hep-ph/9509348].

[58] E. Gardi, J. Kuokkanen, K. Rummukainen and H. Weigert, *Running Coupling and Power Corrections in Nonlinear Evolution at the High-energy Limit*, Nucl. Phys. **A784** (2007) 282-340 [hep-ph/0609087].

[59] I. Balitsky and G. A. Chirilli, *Next-to-leading Order Evolution of Color Dipoles*, Phys. Rev. **D77** (2008) 014019 [0710.4330].

[60] I. Balitsky, *Operator Expansion for High-energy Scattering*, *Nucl. Phys.* **B463** (1996) 99–160, [hep-ph/9509348].

[61] I. Balitsky, *Operator Expansion for Diffractive High-energy Scattering*, hep-ph/9706411.

[62] I. Balitsky, *Factorization and High-energy Effective Action*, *Phys. Rev.* **D60** (1999) 014020, [hep-ph/9812311].

[63] Y. V. Kovchegov, *Small-x F_2 Structure Function of a Nucleus Including Multiple Pomeron Exchanges*, *Phys. Rev.* **D60** (1999) 034008, [hep-ph/9901281].

[64] Y. V. Kovchegov, *Unitarization of the BFKL Pomeron on a Nucleus*, *Phys. Rev.* **D61** (2000) 074018, [hep-ph/9905214].

[65] Y. V. Kovchegov, J. Kuokkanen, K. Rummukainen, and H. Weigert, *Subleading-N_c Corrections in Non-linear Small-x Evolution*, Nucl. Phys. **A823** (2009) 47-82 [0812.3238].

[66] K. Golec-Biernat and M. Wusthoff, *Saturation in Diffractive Deep Inelastic Scattering*, Phys. Rev. **D60** (1999) 114023 [hep-ph/9903358].

[67] L. McLerran and R. Venugopalan, *Computing Quark and Gluon Distribution Functions for Very Large Nuclei*, Phys. Rev. **D49** (1994) 2233-2241 [hep-ph/9309289].

[68] P. Cvitanovic, *Group Theory: Birdtracks, Lie's, and Exceptional Groups*, Princeton University Press (2008) p98.

[69] Y. Hatta, E. Iancu, K. Itakura and L. McLerran, *Odderon in the Color Glass Condensate*, Nucl. Phys. **A760** (2005) 172-207 [hep-ph/0501171].

[70] S. Keppeler and M. Sjödahl, *Orthogonal Multiplet Bases in SU(N_c) Colour Space*, JHEP 0912 (2012) 124 [hep-ph/1207.0609].

[71] C. Marquet and B. Wu, *Exclusive vs. Diffractive Vector Meson Production in DIS at Small x or Off Nuclei* [hep-ph/0908.4180].

[72] H. Kowalski and D. Teaney, *An Impact Parameter Dipole Saturation Model*, Phys. Rev. **D68** (2003) 114005 [hep-ph/0304189].

[73] C. Marquet, R. Peschanski and G. Soyez, *Exclusive Vector Meson Production at HERA from QCD With Saturation*, Phys. Rev. **D76** (2007) 034011 [hep-ph/0702171].

[74] F. Dominguez, C. Marquet, A. Stasto and B.-W. Xiao, *Universality of Multi-particle Production in QCD at High Energies*, Phys. Rev. **D87** (2013) 3, 0340007 [hep-ph/1210.1141].

[75] The ATLAS Collaboration, *Expected Performance of the ATLAS Experiment - Detector, Trigger and Physics*, (2008) [hep-ex/0901.0512].

[76] *LHC Accelerator Complex*, CERN Document Server, © CERN.

[77] R. Schmidt et al., *Protection of the CERN Large Hadron Collider*, New J. Phys. **8** (2006) 290.

[78] *Dipole Magnet*, CERN Document Server, © CERN.

[79] The ATLAS Collaboration, *A $Z \to \mu\mu$ candidate event*, © CERN (2013).

[80] T. Sjöstrand, S. Mrenna and P. Skands, *A Brief Introduction to PYTHIA 8.1*, Comput. Phys. Commun. **178** (2008) 852-867 [hep-ph/0710.3820].

[81] M. Bahr et al., *Herwig++ Physics and Manual*, Eur. Phys. J. **C58** (2008) 639-707 [hep-ph/0803.0883].

[82] T. Gleisberg et al., *Event Generation with SHERPA 1.1*, JHEP 0902 (2009) 007 [hep-ph/0811.4622].

[83] M. G. Pia for the Geant4 Collaboration, *The Geant4 Object Oriented Simulation Toolkit*, EPS-HEP99 Conference, Tampere (1999).

[84] S. Klein and E. Scannapieco, *The Gold Flashlight: Coherent Photons (and Pomerons) at RHIC* (1997) [hep-ph/9706358].

[85] J. Butterworth, *STARlight: A C++ Object-Oriented Monte Carlo Event Generator for Ultra-Peripheral Collisions*, Master of Science Dissertation at the University of Creighton (2009).

[86] A. G. Galperin and V. V. Uzhinskij, *The Calculation of Nucleus-nucleus Interaction Cross-sections at High Energy in the Glauber Approach*, JINR **E2** (1994) 505 [nucl-th/0902.0453].

[87] The ALICE Collaboration, *Charmonium and e+e- Pair Photoproduction at Mid-rapidity in Ultra-peripheral Pb-Pb Collisions at* $\sqrt{s_{NN}} = 2.76$ *TeV*, Eur. Phys. J. **C73** (2013) 2617 [nucl-ex/1305.1467].

[88] The ALICE Collaboration, *Coherent* J/Ψ *Photoproduction in Ultra-peripheral Pb-Pb Collisions at* $\sqrt{s_{NN}} = 2.76$ *TeV*, Phys. Lett. **B718** (2013) 1273-1283 [nucl-ex/1209.3715].

[89] The LHCb Collaboration, *Exclusive* J/Ψ *and* $\upsilon(2S)$ *Production in pp Collisions at* $\sqrt{s} = 7$ *TeV*, J. Phys. G: Nucl. Part. Phys. **40** (2013) 045001 [hep-ex/1301.7084].

[90] The H1 Collaboration, *Diffractive Photoproduction of* J/Ψ *Mesons with Large Momentum Transfer at HERA*, Phys. Lett. **B568** (2003) 205-218 [hep-ex/0306013].

[91] The CMS Collaboration, *Exclusive Photon-photon Production of Muon Pairs in Proton-proton Collisions at* $\sqrt{s} = 7$ *TeV*, JHEP 01 (2012) 052 [hep-ex/1111.5536].

[92] J. L. Abelleira Fernandez, C. Adolphsen, et al., *A Large Hadron Electron Collider at CERN: Report on the Physics and Design Concepts for Machine and Detector* [physics.acc-ph/1206.2913].